“*If it's important you'll find a way. If it's not, you'll find an excuse.*”

— Ryan Blair

ATMOSPHERIC DELAY MODELLING FOR GROUND-BASED GNSS REFLECTOMETRY

by

Thalia Nikolaidou

Dipl. Rural and Surveying Eng., AUTh, 2014

A Dissertation Submitted in Partial Fulfillment
of the Requirements for the Degree of

Doctor of Philosophy

in the Department of Geodesy and Geomatics Engineering

Supervisors: Marcelo Santos, Ph.D., Geodesy and Geomatics Engineering
Felipe Geremia-Nievinski, Ph.D., Federal University of Rio Grande do Sul, Institute of Geosciences, Department of Geodesy

Examining Board: Marcelo Santos, Ph.D., Geodesy and Geomatics Engineering
Felipe Geremia-Nievinski, Ph.D., Geodesy
Richard B. Langley, Ph.D., Geodesy and Geomatics Engineering
Bret Peterson, Electrical and Computer Engineering
William Ward, Ph.D., Physics

External Examiner: Maximilian Semmling, Ph.D., Institute for Solar-Terrestrial Physics, German Aerospace Center, Neustrelitz, Germany

This dissertation is accepted by the
Dean of Graduate Studies

THE UNIVERSITY OF NEW BRUNSWICK

July, 2020

ABSTRACT

Several studies have demonstrated the utility of global navigation satellite system reflectometry (GNSS-R) for ground-based coastal sea-level altimetry. Recent studies evidenced the presence of atmospheric delays in GNSS-R sea-level retrievals and by-products such as tidal amplitudes. On the one hand, several ad-hoc atmospheric correction formulas have been proposed in the literature. On the other hand, ray-tracing studies applied for GNSS-R show little information about the methods and algorithms involved. This dissertation is based on three articles which establish the theoretical framework of the atmospheric delay experienced in ground-based GNSS-R altimetry. In the first article, we defined the atmospheric interferometric delay in terms of the direct and reflected atmospheric delays as well as the vacuum distance and radio length. Then, we clarified the roles of linear and angular refraction, derived the respective delays and combined them in the total delay. We also introduced for the first time two subcomponents of the atmospheric geometric delay, the geometric-shift and the geometric-excess, unique for reflected signals. The atmospheric altimetry correction necessary for unbiased sea-level retrievals was defined as half the rate-of-change of the atmospheric delay with respect to the sine of satellite elevation angle. We developed a ray-tracing procedure to solve rigorously the three-point boundary value problem involving transmitting satellite, reflecting surface, and receiving antenna. We hence evaluated the atmospheric bias in sea-level retrievals for a range of typical scenarios, showing its dependence on elevation angle and reflector height. In the second article, we demonstrated that rigorous ray-tracing of the bent ray can be simplified by a judicious choice of rectilinear wave propagation model. This facilitates the adaptation by existing

GNSS ray-tracing procedures, besides numerical and speed advantages. Further it was emphasized that mapping functions developed for GNSS positioning cannot be reused for GNSS-R purposes without adaptations. In the third article, we developed closed-form expressions of the atmospheric delay and altimetry correction for end-users without access or expertise in ray-tracing. These expressions rely only on direct elevation bending and mean refractivity at the site. Finally, we determined cut-off elevation angle and reflector height, for neglecting atmospheric delays. These limiting conditions are useful in observation planning and error budgeting of the GNSS-R altimetry retrievals.

DEDICATION

To my family in Greece, and my family in Canada that I didn’t know I have.

ACKNOWLEDGEMENTS

"If you want to go fast, go alone. If you want to go far, go together", according to the proverb. In my case, many people supported and accelerated my travel on the Ph.D. trajectory. I would like to take this moment to thank them.

First, I would like to express my deepest gratitude to my immediate supervisor Dr. Marcelo C. Santos. Under your supervision I learnt invaluable lessons that made me evolve as student, but most importantly as a person. You set high expectations for me and I tried to meet them, raising my academic level, always with your excellent guidance and encouragement. Your genuine passion about Geodesy, that reflected on your teaching as well as during our meetings, kept me motivated throughout these years and inspired me to always push further and to learn more. My gratitude is transcending for your unwavering support throughout these years. I will never forget your caring disposition towards the problems I encountered and your always making time to meet even in the midst of your demanding schedule as the Chair of the Department. Your knowledge, discernment and consideration for others are displayed in every aspect of your professorship. I will do everything I can to honor what I have learnt from you in my life and never to let you down.

Then, I cannot begin to express my gratitude to my co-supervisor Dr. Felipe Geremia-Nievinski, to whom I owe the vision, growth and success (according to the committee) of this dissertation. This work would not have been possible without your instrumental guidance and dedicated support. You are gifted at explaining complicated things in a clear manner to help stubborn students like me grasp the concepts and theories behind the numbers and equations. Your endless patience during my endless questions and your commitment as a professor have marked my character as a developing scholar. I am deeply indebted to you for always challenging me to seek quality and excellence in my research; your constructive criticism broadened my intellect and helped me transform from a graduate student to an independent researcher (!).You showed me how research is done, and how a researcher should think, and you walked with me through every detail of this dissertation. For all of this and for much more, I am grateful and ever indebted to you. Nothing can come close to the inspirational presence of a supervisor like Dr. Geremia-Nievinski or unwavering support and guidance of Dr. Santos.

I would also like to thank the members of my dissertation committee - Dr. Richard. B. Langley, Dr. William. Ward, Dr. Brent Petersen and Dr. Maximilian Semmling- for their time and effort reviewing my dissertation as well as their insightful contributions. I very much appreciate Dr. Kevin Englehart for Chairing the committee and Ms. Jacqueline Seely for organizing it, as well as our Department secretary, Ms. Alicia Farnham. I am also grateful to the colleagues, friends and family who tuned in my virtual defense and dissipated the clouds of anxiety. Last but not least, I am thankful to the editors and reviewers of the journals in which this work has been published for their invaluable suggestions.

I would also like to extend my deep gratitude to my professors, both in the Geodesy and Geomatics Engineering department at UNB and in the School of Rural and Surveying Engineering at Aristotle University of Thessaloniki, in Greece, for equipping me with the knowledge and skills needed in the academic life. Especially, I would like to thank Dr. Langley for holding the bi-weekly GNSS meetings, which allowed me to learn from my colleagues and expand my knowledge beyond my research objective as well as meet and communicate with GNSS experts I looked up to since my undergraduate years. I am extremely grateful to Dr. Church who so generously accommodated my needs by granting me a suitable office space. In this office, which ended up being my second home, I found the ideal environment for productive work.

Next, I wish to thank the professors who shared their expertise, insightful feedback and time in collaborative GNSS projects. Dr. Tomasz Hadas (UPWr), Dr. Johannes Böhm (TU Wien), Dr. Harald Schuh (GFZ, TU Berlin), Dr. Sajad Tabibi (University of Luxembourg), Dr. Salim Masoumi (Geoscience Australia), and Dr. Simon Williams (National Oceanography Centre).

Colleagues at UNB as well as at other universities have continuously helped me throughout these years, not only with their ideas and insights, but also with their support and sympathy as friends. Dr. Kyriakos Balidakis, Dr. Eleftheria Pissadaki, MSc. Anthony O. Mayaki, (soon Dr.) Emerson P. Cavalheri, and Dr. Daniel Landskron, thank you! Many thanks also to the students of: the GNSS group at UNB, the Geodesy lab at Federal University of Rio Grande do Sul (UFRGS, Brazil), and the Geodesy and Geoinformatics lab at Wroclaw University of Environmental and Life Sciences in Poland (UPWr), for making work days easier.

On a personal level, first and foremost I wish to thank Fr. John Palmer for being my spiritual Father in all the depth and breadth of such a vocation. I feel extremely blessed for the holy people who surround(ed) me, to whose prayers I owe everything: Elder Archimandrite Ephraim (of Philotheou), Elder Archimandrite Paisios (of St. Anthony's), Abbess Thekla and the Sisters (of Most Holy Theotokos the Consoler), Fr. Matthew Penney & Presvitera Catherine Penney, Fr. Theodore Efthimiadis, Presvitera

Constantina Palmer, Fr. Ioannis Droggitis, Fr. Petros (Church of the Ascension, Greece) as well as Sister Filotheh.

In addition to these people, I am deeply indebted to Dr. Maria Papaioannou for her unconditional love and motherly nurture all the years I have been in Canada. I cannot leave out all my dear friends who having been making my life happier, each in their unique way. I wish to express special thanks to: loving Mrs. Antonia Stratigou, Paul Penney, Diego Fernandes, Iman Sharafaldin, Yessica Enríquez, Dr. Farhad Baratchi, Dr. Ilona Shiller, Matthew Kitchen, M. Ed. Eleni Karavanidou, Dr. Anette Guse, Dr. Constantine Passaris, Carolyna Cavalheri, Dr. Ismael Foroughi, Haris Edirnelis, Dr. Pavel Novac, Marta Padilla, Maria Patrou, Dr. Sofia Mylona and Marina M. Aziz.

This work was made possible through the generous support of Dr.Santos, the School of Graduate Studies of UNB, the Natural Sciences and Engineering Research Council of Canada and Mitacs. International presentations of this work have been facilitated by the GGE department, the International Association of Geodesy and the Canadian Geophysical Union among other organizations. I also thank from the bottom of my heart Dr. Neeru Gupta.

The Canadian Meteorological Centre (Sandrine Edouard - thank you!), National Centers for Environmental Prediction and European Centre for Medium-Range Weather Forecasts provided data for projects I have been involved.

Last but certainly not least, I gratefully acknowledge the assistance of staff at the UNB Writing Centre (Dr. Richard M. Spacek) for their patience reading my manuscripts, as well as staff at ACENET (Dr. Serguei Vassiliev, Dr. Ross Dickson and Dr. Joey Bernard) and GGE (Terry Arsenault and David Fraser) for their technical support and our

past and current GGE secretaries for addressing my every concern. Much thanks also to the URec and SMA Pool staff for brightening my evenings with their smile.

Table of Contents

List of Tables

List of Figures

List of Symbols, Nomenclature and Abbreviations

BVP	boundary-value problem
CIRA	COSPAR international reference atmosphere
CORS	continuously operating reference stations
ECMWF	European Centre for Medium-Range Weather Forecasts
GMF	global mapping function
GNSS	global navigation satellite systems
GNSS-R	global navigation satellite systems reflectometry
GNSS-IR	global navigation satellite systems interferometric reflectometry
GNSS-MR	global navigation satellite systems multipath reflectometry
GPS	global positioning system
GPT	Global Pressure and Temperature
IERS	international Earth rotation and reference systems service
IVP	initial-value problem
NWM	numerical weather model
OSTM	ocean surface topography mission
RA	rectilinear-apparent ray-tracing approach
RG	rectilinear-geometric ray-tracing approach
RI	rigorous ray-tracing approach
RM	rectilinear-mixed ray-tracing approach
SNR	signal-to-noise ratio
TEC	total electron content

TUW	Technical University of Vienna
UNB	University of New Brunswick
VMF	Vienna mapping functions
$d; d_d, d_r, d_i$	atmospheric delay; direct, reflected, interferometric
$D; D_d, D_r, D_i$	vacuum distance; direct, reflected, interferometric
$e; e'$	satellite elevation angle; geometric, apparent
H	reflector height
$L; L_d, L_r, L_i$	radio length; direct, reflected, interferometric
n	index of refraction
$r; r_{sat}, r_{ant}, r_{sfc}$	position vector; satellite; antenna; surface reflection point
$R; R_d, R_r, R_i$	curve range; direct, reflected, interferometric
δe	elevation bending
λ	GNSS satellite carrier wavelength
τ_i	interferometric propagation delay
ϕ_i	interferometric phase

1. Introduction

Global sea-level rise is increasing in recent decades (Church et al., 2013) posing inundation and erosion danger at coastal and island communities. Higher sea-levels can also produce more frequent nuisance flooding due to storm surges threatening coastal community, land, and infrastructure activities. An approximate one centimeter rise in sea-level on a gently sloping beach can push the water one meter farther inland (Siebentritt, 2016). With a large percentage of the world's population living near the coast, even small changes in the sea-level can have substantial societal and economic impacts. However, lack of comprehensive historical data sets as well as discontinuities preclude confident predictions of the sea-level rise (Alley, Clark, Huybrechts, & Joughin, 2005). Thus, precise monitoring of the dynamic as well as the long-term sea-level variations would improve estimates of both the regional and the global sea-level rise.

Global Navigation Satellite Systems Reflectometry (GNSS-R) is an emerging remote sensing method that can measure sea-level, among other geophysical variables. It exploits GNSS radio waves reflected off the Earth's surface, including the oceans. Ground-based GNSS-R can provide geocentric coastal sea-level measurements bypassing any spirit levelling and vertical land motion errors that the tide gauge datum may have. GNSS radio-wave broadcast is ubiquitous, open and all-weather. GNSS-R setups can be easily deployed to gauge sea level. Moreover, existing GNSS continuously operating reference stations, installed for geodetic and/or geophysical applications, can be used for reflectometry purposes as sites of opportunity with no additional cost (Geremia-Nievinski & Hobiger, 2020; Geremia-Nievinski, Makrakis, & Tabibi, 2020). Recent research has also demonstrated the feasibility of using low-cost equipment (Strandberg, 2020) making GNSS-R particularly appealing for future on-demand deployment.

Thus, it becomes clear that GNSS-R features many advantages and can, not only provide regional information but also contribute to estimates of the global mean sea-level rise. To leverage these advantages and match the accuracy of the traditional measuring techniques, i.e., tide gauges and satellite altimetry, it is important that systematic errors are modelled. Furthermore, in order for GNSS-R to contribute to long-term studies, stable and unbiased time series are required. In accordance with recommendations from the Decadal Survey for Earth Observation from Space (National Academies of Sciences, Engineering, 2018), the uncertainty in sea-level change rates at global, regional, and local scales is sought to be better than 0.1 mm/yr for global mean sea-level equivalent and better than 0.5 mm/yr sea-level equivalent at resolution of 10 km.

Despite the very high demand for accuracy, there is still a number of corrections in GNSS-R that are not consistently applied, and assumptions commonly made in the analysis can lead to systematic effects, hence failing to meet the above requirements. One assumption often made concerns atmospheric refraction. The neutral atmosphere refractive index causes a change in speed and direction of the GNSS radio waves compared to their vacuum propagation. Both types of refraction affect GNSS observations in terms of the so-called atmospheric delay or tropospheric delay. GNSS-R deals with the reflected minus direct atmospheric delay, also known as the interferometric atmospheric delay, which cancels out the bulk of refraction. However, the cancelation is not exact, leading to biases in the sea-level retrievals that depend on the satellite elevation angle and the station altitude. Recent studies evidenced the presence of atmospheric refraction in GNSS-R sea-level retrievals and by-products such as tidal amplitudes (Williams & Nievinski, 2017).

To account for atmospheric refraction in GNSS-R, several ad-hoc atmospheric correction formulas have been proposed in the literature (Fabra et al., 2012; N. Roussel et al., 2014; Santamaría-Gómez & Watson, 2017; Santamaría-Gómez, Watson, Gravelle, King, & Wöppelmann, 2015; Treuhaft, Lowe, Zuffada, & Chao, 2001). On the other hand, ray-tracing studies applied to GNSS-R (Anderson, 2000; Semmling et al., 2012) show little information about the methods and algorithms involved. Modelling atmospheric delays for ground-based GNSS reflectometry constitutes the main thread of this work; more specifically it builds on the proposition that interferometric atmospheric delay features unique characteristics compared to the direct or line-of-sight propagation. This affects the observation planning in GNSS-R and can bias altimetry retrievals. Ergo, employing ray-tracing, we model its principal components and their effect on the altimetry retrievals and develop closed-form expressions to correct for them.

The motivation for this work thus emanates from the ongoing climate change with sea-level rise as a leading consequence. Although we focus on sea level retrievals, the results have direct application also to snow depth retrievals because it is also an altimetric process. Thus, this study feeds the need to harness GNSS-R for altimetry applications. The reasoning for our choice is supported by the possibility of using existing GNSS sites for gauging/reflectometry applications and further exploit their time series to study long-term sea level. Yet, mitigation of the atmospheric delay is imperative not only for unbiased geocentric sea-level retrievals and stable time series, but also for accurate GNSS-R by-products such as tidal coefficients.

1.1. Contributions of this dissertation

This work establishes the theoretical framework of the atmospheric refraction experienced in ground-based GNSS-R. It is corroborated by the development of a ray-tracing procedure that solves rigorously the three-point boundary value problem in GNSS-R. It includes a thorough analysis of the interferometric atmospheric delay and corresponding atmospheric altimetry correction using the satellite elevation angle and reflector height as the independent variables. It also assesses the concepts/models currently found in the literature and indicates their level of appropriateness. Ultimately, it offers the tools to mitigate atmospheric refraction for unbiased GNSS-R ground-based sea-level retrievals.

In particular, our contribution is divided in three parts with reference to the articles constituting this dissertation. In the first part, we present the intrinsic radio propagation quantities of vacuum distance, curve range and radio length, necessary for understanding atmospheric refraction. We give the definition of the interferometric atmospheric delay in terms of the direct and reflected atmospheric delays. Further, we clarify the roles of linear and angular refraction in contributing to the total delay as a function of satellite elevation angle. We also unify the interferometric delay components, along-path and geometric, into the total delay. We also introduce for the first time two subcomponents of the atmospheric geometric delay, the geometric-shift and the geometric-excess, unique for reflected signals. While the latter fine-tunes the delay, the former is an indispensable part of the total delay at low elevation angles. Furthermore, we provide an atmospheric altimetry correction necessary for unbiased sea-level retrievals. Using simulations, we investigate the dependence of the interferometric atmospheric delay and its components on the key variables of satellite elevation angle and reflector height. The magnitude and variability of the atmospheric altimetry correction reveals the impact of atmospheric refraction on the retrieved heights. We thus quantify the atmospheric bias in GNSS-R sea-level retrievals.

In the second part, we show how interferometric results can be obtained using rectilinear ray-tracing. The presented approach is faster and more efficient because it does not require solving a differential equation in reflections, involving only the broadcasting satellite and the receiving antenna. We also demonstrate that the atmospheric layers both above and below the receiver contribute to the total interferometric delay, contrary to the popular belief that atmospheric refraction effects originating above the receiver cancel out when forming the interferometric quantities. This highlights that mapping functions developed for GNSS positioning cannot be reused for GNSS-R purposes without adaptations.

In the third and final part, we develop closed-form expressions of the atmospheric delay and atmospheric altimetry correction for end-users without access or expertise in ray-tracing. Those expressions have the advantage of relying only on two auxiliary meteorological variables to predict the delay, refractivity and elevation angle bending. The two variables can be obtained via a single direct-only ray-tracing or from empirical models in the absence of ray-tracing software. Finally, we show limiting conditions for neglecting atmospheric refraction for cut-off elevation angle and reflector height. These results are valuable in observation planning and error budgeting of the GNSS-R retrievals.

In total, our work casts a new light on the atmospheric refraction experienced by GNSS reflections, through the development of a rigorous ray-tracing procedure for reflections. It offers the fundamental knowledge and the tools to correct for the total atmospheric delay and recover unbiased altimetry retrievals. While it is applicable to the broader GNSS-R altimetry applications, the proposed interferometric atmospheric modelling contributes especially towards geocentric sea-level monitoring made by ground-based GNSS-R.

The rest of this dissertation is as follows. Chapter 2 gives a brief background on the sea-level measurements, underlines the need for accurate and precise GNSS-R retrievals; a short review linking the main parameter of interest – atmospheric altimetry correction – to the main observable in GNSS-R – SNR – follows immediately after, with the objective to introduce the reader to the next chapters. The three original articles summarized above are presented in subsequent chapters (3, 4, and 5). Chapter 6 summarizes the main findings of this work and presents suggestions for future work and challenges. Few footnotes in the Chapters 3-5 include additions to this thesis not included in the published articles.

2. Background

2.1. Sea-level measurements

In-situ sea-level measurements have been traditionally performed using tide gauges. Although such records from modern stations are highly accurate, meticulous monitoring is required to model and subtract the time-dependent vertical land motion from the measurements, for which GNSS positioning is the recommended approach. Since it is common for the tide gauge and the GNSS station to be separated by a distance that can reach up to a few kilometers, spirit levelling is necessary to connect the two, which adds additional errors.

Moreover, although long-term tide-gauge records make possible the extraction of local sea-level trends, it is difficult to deduce global trends due to interannual and decadal periodicities in the local records (Douglas, 2001). Albeit the global distribution of the coastal and island tide gauge network has increased since the last century, existing gaps introduce uncertainties in the global sea-level estimate. Unless filled in by other techniques, e.g.,, satellite altimetry or GNSS-R, these gaps introduce uncertainties in the global sea-level. Furthermore, while tide gauges are unique in capturing high frequency water level variations, water level extremes may not be captured representatively enough by a tide gauge because of its inability to measure the water level beyond its immediate circumference. Inhomogeneities in the data caused from an undocumented equipment change and data gaps due to power outage can also affect the quality of the data recorded and the long-term trends derived. Lastly, the near proximity of the tide gauge equipment with the water means increased wear and tear.

Remote sensing sea level monitoring in the open oceans is primarily performed via satellite altimetry (e.g., TOPEX/Poseidon, Jason-1, and Ocean Surface Topography Mission (OSTM)/Jason-2 missions). It can be aided by satellite imagery when serving specific applications (e.g., flood monitoring, storm surges, etc.). Global sea-level measurements since late 1992 have been contributing to our understanding of climate change and phenomena, such as storm surges and large-scale circulations (Chen et al., 2017; Li, Hinnov, Huang, & Ogg, 2018). Although altimetry offers nearly global sea-level measurements, its coarse spatio-temporal resolution is problematic when it comes to mesoscale observations (Jin, Cardellach, & Xie, 2014b). Moreover, it is not effective for coastal applications, due to the loss of accuracy in such areas (Cazenave, Palanisamy, & Ablain, 2018). While tide gauges and altimeters operate on a completely different basis, the former are used to calibrate the latter (Mitchum, 2000). Hence, these two techniques are not completely independent; to minimize the error propagation, independent measurements, e.g. ship survey, and/or GNSS-R, are necessary for unbiased retrievals.

2.2. GNSS Reflectometry

GNSS is well established for positioning, navigation and timing. It also has its share in geodesy, by contributing to the definition of reference frame parameters in addition to very long baseline interferometry, satellite laser ranging and other satellite and space geodetic techniques. In the last decades GNSS gained ground in atmospheric science providing information about the neutral atmosphere (Bevis et al., 1994, 1992; Ho et al., 2019) and the ionosphere (Calais, Minster, & Bernard, 1995; Klobuchar, 1991; Rocken et al., 1997). While GNSS-meteorology uses ground-based stations, GNSS Radio Occultation (Feng & Herman, 1999; Fjeldbo et al., 1965; Yakovlev, Matyugov, &

Vilkov, 1995) utilizes space-based receivers to extract weather data at different levels of the atmosphere for applications in numerical weather prediction, climate studies and atmospheric dynamics.

In recent decades, GNSS Reflectometry (GNSS-R) has emerged as a technique to remotely sense the Earth's surface environments. Using the radio waves reflected off the Earth's surface as sources of opportunity, GNSS-R has applications in remote sensing of the ocean (e.g., altimetry, tides, currents, winds), hydrology (e.g., soil moisture), vegetation (e.g., forest biomass) and the cryosphere (e.g. dry and wet snow monitoring).

One particular GNSS-R configuration is called GNSS Interferometric Reflectometry (GNSS-IR) (Larson, 2016), also known as GNSS Multipath Reflectometry (GNSS-MR) (Zavarotny et al., 2014). In GNSS-IR or GNSS-MR, reflections are superimposed with the line-of-sight (LOS) or direct propagation from the satellite. As a consequence, crests (constructive interference) and troughs (deconstructive interference) are created in the power of the received – including direct and reflected – signal. These oscillations are particularly evident in the signal-to-noise ratio (SNR) measurements a receiver is recording. Decoding the features of these oscillation reveals information about the reflecting surface. Specifically, measuring the phase and the amplitude of the oscillation can be used to derive information about the soil moisture and the vegetation characteristics respectively while their frequency is related to the height of the reflecting surface, allowing sea-level and snow depth determination.

Over the following years, many pioneering studies (Cardellach et al., 2011; Larson, 2016; Zavorotny, Gleason, Cardellach, & Camps, 2014), explored the possibilities of using GNSS reflections for water/sea/ice level (Larson, Ray, Nievinski, & Freymueller, 2013; Lofgren, 2014; Roussel et al., 2015), soil moisture (Tabibi, Nievinski, Van Dam, & Monico, 2015), snow depth (Estel Cardellach, Fabra, Rius, Pettinato, & D'Addio, 2012), permafrost melt (Liu & Larson, 2018), ice detection (Strandberg, Hobiger, & Haas, 2017), firn density (Larson, Wahr, & Munneke, 2015), vegetation water content (Wan, Larson, Small, Chew, & Braun, 2015) and agriculture (Small, Larson, & Braun, 2010). Long-term analysis of GNSS reflected signals has also been presented by Larson, Ray, & Williams (2017) and Siegfried, Medley, Larson, Fricker, & Tulaczyk (2017) among other studies. Other seminal works include simulating the refection's characteristics based on the antenna response and the surface scattering (Nievinski & Larson, 2014a, 2014b), using GNSS-R as a validation technique for soil moisture (Al-Yaari et al., 2017) and constraining surface mass balance (Larson et al., 2015).

The multitude of GNSS-R ground-based applications are supported by its easy deployment and simpler equipment compared to airborne and spaceborne GNSS-R and other sensing techniques. Many of the GNSS stations utilized by the above studies are part of continuously operating reference stations (CORS) networks deployed for geodetic purposes and are thus simply used as sites of opportunity. The utility of such sites, besides their global distribution, extends also to the long time series records of several of them, for studies of periodic and long-term phenomena impacting Earth's surface. In addition, ground-based GNSS-R offers a convenient spatial resolution, i.e., between in-situ and satellite observations, facilitating its adaptation by specific application and need. Furthermore, one can target a specific geographic area of interest by adjusting the height of the antenna and the satellite cut-off elevation angle. The near simultaneous measurement of multiple reflection points around the antenna will result in more representative average values of sea-level, soil moisture, etc. Remarkably, GNSS-R has the unique advantage of providing measurements defined directly in the International Terrestrial Reference Frame. It follows that GNSS-R can provide geocentric coastal sea-level measurements. Critical to GNSS-R altimetry is the interferometric propagation delay $\tau_i = \tau_r - \tau_d$, the difference in propagation between reflection and direct propagation, expressed in meters. Its largest component is the free-space vacuum distance, $\tau_i \approx D_i + \cdots$. Assuming a locally horizontally reflecting surface, the latter is geometrically derived as:

$$D_i = 2H \sin(e) \qquad (1)$$

with H denoting vertical distance between the receiver and the reflecting surface (Larson & Nievinski, 2012) and e the satellite elevation angle. The vacuum distance D_i is largest at zenith ($\lim_{e=90^\circ} D_i = 2H$) – where it equals the round-trip distance from the antenna to the surface and back – and is zero when the satellite rises or sets ($\lim_{e \to 0^\circ} D_i = 0$).

Altimetry is synonymous with solving for H in the propagation delay equation above. Basically, it can be performed in two ways. On the one hand, there is the ratio method, $\hat{H} = 0.5\, \tau_i / \sin e$, which requires absolute interferometric delays τ_i (akin to ambiguity-fixed phase). On the other hand, there is the rate method, $\hat{H} = 0.5\, \partial \tau_i / \partial \sin e$, which requires only the variation of τ_i with satellite elevation angle (akin to Doppler). The interferometric delay rate, assuming a constant reflector height, follows from eq. (1) as: $\dot{D}_i = 2H\dot{e}\cos(e)$. The interferometric Doppler can then be described as: $f_i = -\dot{D}_i / \lambda = -\, 2H\dot{e}\cos(e)/\lambda$, with λ denoting the carrier wavelength. A thorough review on the interferometric Doppler can be found in (Nievinski & Larson, 2014a; M.

Semmling, 2012). SNR-based GNSS-R or GNSS-IR/MR relies on the delay rate method, as it involves a frequency estimation.

However, all the terms neglected in the initial approximation $\tau_i \approx D_i + \cdots$ may cause altimetry biases, such as the random surface roughness, antenna phase gain and phase pattern, the medium composition (via Frensel reflection coefficients), surface tilting or undulations, etc. (Nievinski & Larson, 2014a). Perhaps the main source of altimetry bias in GNSS-R is the atmospheric refraction. It will produce an extra term d_i in the total propagation delay $\tau_i \approx D_i + d_i$ ... It will result in an atmospheric altimetry bias (or its negative, the atmospheric altimetry correction) defined based on the retrieval method employed (ratio or rate).

In GNSS-R altimetry, atmospheric refraction can be accounted for at different levels. The easiest one is at the coordinate level, subtracting an altimetry correction from the biased reflector heights retrieval: $\hat{\hat{H}} = \hat{H} - \Delta H$. In fact, most comparisons between GNSS-R and tide gauges are done in a relative sense, removing the average difference, thus implicitly removing the constant part of atmospheric bias. An alternative approach is to correct for atmospheric refraction during the processing of the observations. For such an approach, the theoretical atmospheric delay is subtracted from the experimental interferometric delay, prior to or during the application of the retrieval algorithm: $0.5\,\partial(\tau_i - d_i)/\partial \sin e$. The level distinction is analogous to that in the application of atmospheric pressure loading correction in GNSS positioning (Tregoning & van Dam, 2005): fast-changing instantaneous corrections are applied at the observation level, while slowly changing average corrections can be applied at the coordinate level, depending on the session duration.

2.3. Atmospheric Refraction in Space Geodesy

In this section we offer a brief introduction in the atmospheric refraction in space geodesy; we recall the basics of atmospheric modelling for direct/line-of-sight propagation, which we will use to base our initial assumptions for the propagation of the reflected signals.

Atmospheric refraction causes, characteristics and modelling techniques for GNSS positioning have been extensively studied, both recently (Balidakis, 2019; Landskron, 2017) and classically (Niell, 1996; Saastamoinen, 1972). In atmospheric modelling for radio waves, it is typical to characterize the atmosphere as a mixture of dry gases and water vapor, considering its behavior very close to that of an ideal gas (Böhm, Salstein, Alizadeh, & Wijaya, 2013). Dry air is a gas mixture, the most important constituents of which are nitrogen and oxygen, constituting 99% of the total volume; while greenhouse gas, including water vapor, form the remaining 1%. In contrast to dry gases, water vapor has a strong temporal and spatial variation and has a major role not just on meso- and micro-scale weather events but also in global weather and climate.

Regarding the propagation of electromagnetic waves, in the radiowave band, the atmosphere is divided into two layers: an ionized (ionosphere) and a non-ionized or non-dispersive medium, the neutral atmosphere, commonly referred to as the troposphere. By definition, neutral atmosphere includes the troposphere, which extents up to 9-16 km above the Earth’s surface (depending on the latitude), and it is combined with the adjusted layers of stratosphere and mesosphere and even part of the thermosphere, to accumulatively exceed 80 km above the Earth's surface. However, for GNSS purposes, contributions of the neutral atmosphere above 75 km can be ignored[1] (Mendes, 1999).

Both layers cause a propagation delay with respect to its vacuum propagation. Ionospheric delay can effectively be eliminated by using dual-frequency receivers and the appropriate linear combination when processing GNSS observations (ionosphere free).

Neutral atmosphere's effect on radio waves depends mainly on temperature, pressure and relative humidity. The neutral atmospheric delay, as seen below, is frequency independent and thus its modelling is required to remove its effect. According to Fermat's principle of least time, the path followed by a GNSS ray joining the station antenna and satellite, is the one that can be traversed in least time. The time interval Δt, taken from transmitter T, to antenna A, can be described as:

$$\Delta t = \frac{1}{c} \int_{A}^{T} n \, ds \tag{2}$$

where n is the index of refraction and c is the speed of light in vacuum ($299{,}792{,}458$ m s^{-1}). It is more common though to express the time delay in terms of optical path length or radio path length L (in meters) as:

$$L = c \, \Delta t \tag{3}$$

Usually, for practical reasons, the refractivity N (unitless) is used instead of the refractive index[2],

$$N = (n - 1) \tag{4}$$

---

[1] In this work we adopted 100 km as the upper limit for the neutral-atmosphere.

[2] Often N is defined with a 10^6 factor, but here we do not follow that.

The total refractivity of moist air for neutral gases and radio waves can be described as a function of the partial pressure of dry gases and water vapor, P_d and P_w (in hPa) respectively and the temperature T (in K) :

$$N = k_1 \frac{P_d}{T} + k_2 \frac{P_w}{T} + k_3 \frac{P_w}{T^2} \tag{5}$$

The coefficients k_1, k_2 and k_3 are determined experimentally in laboratory (Rüeger, 2002; Thayer, 1974). The first term corresponds to the "dry" part of refractivity and the remaining two terms to the "wet" part, due to water vapor. Yet, upon rewriting refractivity as a function of the total mass density ρ, refractivity can be separated in to a "hydrostatic" and a "non-hydrostatic" part:

$$N_h = k_1 R_d \rho \tag{6}$$

$$N_{nh} = k_2' \frac{P_w}{T} + k_3 \frac{P_w}{T^2} \tag{7}$$

with R_d the dry air constant (usually $R_\mathrm{d} = 287.05376$ J/(kg K)), and

$$k_2' = k_2 - k_1 \frac{R_w}{R_d} \tag{8}$$

with $\mathrm{R_w}$ the wet air constant (usually $\mathrm{R_w} = 461.5$ J/(kg K)).

Integrating vertically the refractivity profile, in terms of ellipsoidal height h, the (total) zenith delay is derived:

$$d^z = \int_h^\infty N \ dh \tag{9}$$

Similarly, integrating the refractivity parts the respective zenith delays can be derived minding the correct grouping i.e., $d^z = d_h^z + d_{nh}^z$.

Similar expressions can be derived for the non-zenithal or slant directions, except that the result will be only the so-called along-path delay:

$$d^a = \int_A^T N \, ds \tag{10}$$

To express the total slant delay, the geometric delay d^g, which is a consequence of the bending of the ray due to angular refraction, needs to be added to the sum of the two components, e.g. $d = d^a + d^g$, defined as:

$$d^g = \int_A^T 1 \, ds - D \tag{11}$$

where D is the straight-line distance.

2.4. Mapping Functions

The neutral atmospheric delay of a radio wave is least when propagated at the zenith direction and increases with increasing satellite elevation angle. The projection of the zenith direction d^z to the slant delay at an arbitrary elevation angle is performed by means of a mapping function. In general, it is a function of elevation angle and usually assumes azimuthal symmetry of the neutral atmosphere, as well as its hydrostatic equilibrium. Although several mapping functions have been suggested in the literature (Hopfield, 1969; Marini & Murray, 1973; Niell, 1996; Saastamoinen, 1972), the prevailing ones are the VMF1 (Boehm, Werl, & Schuh, 2006) developed by the Technical University of Vienna (TUW). Their accuracy and precision have been extensively tested and compared against other mapping functions (Nikolaidou, Balidakis, Nievinski, Santos, & Schuh, 2018; Urquhart, Nievinski, & Santos, 2012, 2013) and have also been used as models for other mapping functions such as the UNB-VMF1 by the

University of New Brunswick (Urquhart, Santos, Nievinski, & Böhm, 2014), and the GFZ-VMF and Potsdam mapping functions by the German Research Centre for Geosciences (Balidakis et al., 2018; Zus, Dick, Heise, & Wickert, 2015). VMF1 are suggested by the International Earth Rotation and Reference Systems Service (IERS) Conventions (Petit & Luzum, 2010) for all geophysical applications. However, improved mapping functions have also been generated recently (Drożdżewski, Sośnica, Zus, & Balidakis, 2019; Landskron & Böhm, 2017) featuring higher spatiotemporal resolution and better agreement with the numerical weather models, among other enhancements. Mapping function of a particular functional form (e.g., *a, b, c* in a continued fraction) are obtained by fitting to ray-tracing results.

2.5. Atmospheric Ray-tracing

According to the American Meteorological Society's Glossary of Meteorology (AMS, 2020) and adjusted to our scope, ray-tracing is a mathematical approximation scheme for determining the propagation of electromagnetic waves by following the path of rays obeying the laws of reflection and refraction. Ray-tracing can be used to retrieve the delay at any satellite elevation angle (Nievinski and Santos, 2009). It serves as the basis for the development of a mapping function, by fitting coefficients of a particular functional form (e.g., *a, b, c* in a continued fraction).

The meteorological data on which refraction is evaluated are provided by the atmospheric source, which can be radiosondes, a climatology or a numerical weather model. Radiosondes sample the atmosphere vertically and although they are very accurate, they have a rather coarse horizontal resolution. A climatology on the other hand can offer a substantial spatial coverage but represents mean conditions and thus discrepancies are expected during atypical weather conditions. Numerical weather models assimilate in situ observations and exploit atmospheric physics to model atmospheric circulation. Their output is a set of 3D grids sampling meteorological variables, e.g., pressure, temperature, humidity, etc.. They represent the state-of-the-art atmospheric source and come on a variety of spatial and temporal scales and are provided on a routine basis by many centers, e.g., the Canadian Meteorological Center, the European Centre for Medium Range Weather Forecasts.

The numerical results presented here are based on a reflections (3-point) raytracing procedure, as described below. It was built upon the UNB ray-tracing code developed initially for direct propagation by Nievinski (2009). It was further enhanced here to include reflected radio waves, the details of which are included in Chapter 3. All the direct ray-tracing modelling options are presented in Nievinski & Santos (2010). Validation of the raytracing procedure is provided by Nafisi et al. (2012), who compared results of five independent ray-tracing implementations from different research groups worldwide. The UNB ray-tracing code has been widely utilized for GNSS positioning (Urquhart et al., 2012; Urquhart, Santos, Nievinski, & Böhm, 2014; Nikolaidou, Balidakis, et al., 2018; Nikolaidou, Nievinski, Balidakis, Schuh, & Santos, 2018), GNSS-meteorology (Mayaki, Nikolaidou, Santos, & Okolie, 2018; Mcadam, 2013) as well as in GNSS-R (Williams and Nievinski, 2017).

2.6. Direct versus Interferometric atmospheric delays

Thus far, an introductory review has been presented on atmospheric delay modelling and determination, assuming direct radio wave propagation. Reflected radio waves will suffer very similar atmospheric effects down to the antenna height before they reflect off the Earth's surface. Thus, it is reasonable to consider the direct propagation modelling techniques as a first approach to our problem. This consideration will take the form of a juxtaposition of the direct and reflected delay's characteristics. The following chapters provide a rigorous solution on these issues. This section aims to briefly introduce the direct propagation effects to the interferometric and thus enhance the understanding of the latter. It also attempts to delineate the limits of applying direct models for the interferometric delay and expose its unequaled characteristics.

The boundaries of the time interval for the reflected raypath Δt_r, will involve the reflection point P, splitting the ray to the incoming $\Delta t_{r_{in}}$ and outgoing $\Delta t_{r_{out}}$ raypath "legs":

$$\Delta t_r = \Delta t_{r_{in}} + \Delta t_{r_{out}} = \frac{1}{c}\left(\int_S^T n\, ds + \int_A^S n\, ds\right) \tag{12}$$

Assuming that direct and reflected signals suffer similar atmospheric refraction effects during Δt, one could further partition $\Delta t_{r_{in}}$ using the antenna height above the reflecting surface:

$$\Delta t_{r_{in}} = \frac{1}{c}(\int_A^T n\, ds + \int_S^A n\, ds) \tag{13}$$

Combining with to eq.(2), the interferometric time interval Δt_i, can be described as:

$$\Delta t_i = \Delta t_r - \Delta t = \frac{1}{c}(\int_S^A n\, ds + \int_A^S n\, ds) \tag{14}$$

To solve for Δt_i, the location of the reflection point and the index of refraction along the raypath need to be determined. The exact location of the reflection point can be calculated only in vacuum conditions because it depends, as it is proven later, on the angular refraction. The raypath, and hence the index of refraction along it, depends, in turn also on the location of the reflection point. Thus, the need for a 3-point boundary value iterative procedure (i.e., ray-tracing), in contrast to the 2-point ray-tracing employed in direct signal propagation, becomes obvious.

A naïve endeavor to model the interferometric delay would consist of applying a direct propagation model twice, each at the azimuth of the incoming and outgoing raypath “legs”, at the vacuum location on the surface S, and for the atmospheric layer of thickness H. However, such an approach disregards a) the impact of the atmospheric layer above the antenna and b) assumes the reflection point will remain unchanged under atmospheric conditions. This thesis addresses the impact of both of these assumptions in detail, in Chapter 3.

References

Al-Yaari, A., Wigneron, J.-P., Kerr, Y., Rodriguez-Fernandez, N., O'Neill, P. E., Jackson, T. J., … Yueh, S. (2017). Evaluating soil moisture retrievals from ESA's SMOS and NASA's SMAP brightness temperature datasets. *Remote Sensing of Environment*, *193*, 257–273. doi.org/10.1016/J.RSE.2017.03.010

Alley, R. B., Clark, P. U., Huybrechts, P., & Joughin, I. (2005). Ice-Sheet and Sea-Level Changes. *Science, 310*(5747), 456–460.

American Meteorological Society, cited 2020: "ray-tracing ". Glossary of Meteorology. [Available online at http://glossary.ametsoc.org/wiki/ray-tracing]. (2020). Retrieved July 13, 2020, from http://glossary.ametsoc.org/wiki/Main_Page

Anderson, K. D. (2000). Determination of water level and tides using interferometric observations of GPS signals. *Journal of Atmospheric and Oceanic Technology*, *17*(8), 1118–1127. doi.org/10.1175/1520-0426(2000)017<1118:DOWLAT>2.0.CO;2

Balidakis, K. (2019). *On the development and impact of propagation delay and geophysical loading on space geodetic technique data analysis (Ph.D. dissertation)*. Technische Universität Berlin. doi.org/10.14279/depositonce-9125

Balidakis, K., Nilsson, T., Zus, F., Glaser, S., Heinkelmann, R., Deng, Z., & Schuh, H. (2018). Estimating Integrated Water Vapor Trends From VLBI, GPS, and Numerical Weather Models: Sensitivity to Tropospheric Parameterization. *Journal of Geophysical Research: Atmospheres*, *123*(12), 6356–6372. doi.org/10.1029/2017JD028049

Bevis, M., Businger, S., Chiswell, S., Herring, T. A., Anthes, R. A., Rocken, C., … Ware, R. H. (1994). GPS Meteorology: Mapping Zenith Wet Delays onto Precipitable Water. *Journal of Applied Meteorology*, *33*(3), 379–386. doi.org/10.1175/1520-0450(1994)033<0379:GMMZWD>2.0.CO;2

Bevis, M., Businger, S., Herring, T. A., Rocken, C., Anthes, R. A., & Ware, R. H. (1992). GPS meteorology: Remote sensing of atmospheric water vapor using the global positioning system. *Journal of Geophysical Research*, *97*(D14), 15787. doi.org/10.1029/92JD01517

Boehm, J., Werl, B., & Schuh, H. (2006). Troposphere mapping functions for GPS and very long baseline interferometry from European Centre for Medium-Range Weather Forecasts operational analysis data. *Journal of Geophysical Research: Solid Earth*, *111*(B02406). doi.org/10.1029/2005JB003629

Böhm, J., Salstein, D., Alizadeh, M. M., & Wijaya, D. D. (2013). Geodetic and Atmospheric Background (pp. 1–33). Springer, Berlin, Heidelberg. doi.org/10.1007/978-3-642-36932-2_1

Calais, E., Minster, J. B., & Bernard, J. (1995). GPS detection of ionospheric perturbations following the January 17, 1994, Northridge Earthquake. *Geophysical Research Letters*, *22*(9), 1045–1048. doi.org/10.1029/95GL00168

Cardellach, E., Fabra, F., Nogués-Correig, O., Oliveras, S., Ribó, S., & Rius, A. (2011). GNSS-R ground-based and airborne campaigns for ocean, land, ice, and snow techniques: Application to the GOLD-RTR data sets. *Radio Science*, *46*(5), 1–16. doi.org/10.1029/2011RS004683

Cardellach, Estel, Fabra, F., Rius, A., Pettinato, S., & D'Addio, S. (2012). Characterization of dry-snow sub-structure using GNSS reflected signals. *Remote Sensing of Environment*, *124*, 122–134. doi.org/10.1016/J.RSE.2012.05.012

Cazenave, A., Palanisamy, H., & Ablain, M. (2018). Contemporary sea level changes from satellite altimetry: What have we learned? What are the new challenges? *Advances in Space Research*, *62*(7), 1639–1653. doi.org/10.1016/j.asr.2018.07.017

Chen, X., Zhang, X., Church, J. A., Watson, C. S., King, M. A., Monselesan, D., … Harig, C. (2017). The increasing rate of global mean sea-level rise during 1993-2014. *Nature Climate Change*, *7*(7), 492–495. doi.org/10.1038/nclimate3325

Church, A. J., Clark, U. P., Cazenave, A., Gregory, M. J., Jevrejeva, S., Levermann, A., … Unnikrishnan, S. A. (2013). Sea level change. In V. B. and P. M. M. Stocker, T.F., D. Qin, G.-K. Plattner, M. Tignor, S.K. Allen, J. Boschung, A. Nauels, Y. Xia (Ed.), *Climate Change 2013 the Physical Science Basis: Working Group I Contribution to the Fifth Assessment Report of the Intergovernmental Panel on Climate Change* (Vol. 9781107057, pp. 1137–1216). Cambridge, United Kingdom and New York: Cambridge University Press. doi.org/10.1017/CBO9781107415324.026

Douglas, B. C. (2001). Sea level change in the era of the recording tide gauge. In *International Geophysics* (Vol. 75, pp. 37–64). Academic Press. doi.org/10.1016/S0074-6142(01)80006-1

Drożdżewski, M., Sośnica, K., Zus, F., & Balidakis, K. (2019). Troposphere delay modeling with horizontal gradients for satellite laser ranging. *Journal of Geodesy*, *93*(10), 1853–1866. doi.org/10.1007/s00190-019-01287-1

Fabra, F., Cardellach, E., Rius, A., Ribó, S., Oliveras, S., Nogués-Correig, O., … D'Addio, S. (2012). Phase altimetry with dual polarization GNSS-R over sea ice. *IEEE Transactions on Geoscience and Remote Sensing*, *50*(6), 2112–2121. doi.org/10.1109/TGRS.2011.2172797

Feng, D. D., & Herman, B. M. (1999). Remotely Sensing the Earth's Atmosphere Using the Global Positioning System (GPS)—The GPS/MET Data Analysis. *Journal of Atmospheric and Oceanic Technology*, *16*(8), 989–1002. doi.org/10.1175/1520-0426(1999)016<0989:RSTESA>2.0.CO;2

Fjeldbo, G., Eshleman, V. R., Garriott, O. K., Smith, F. L., Garriot, O. K., & Smith, F. L. (1965). The two-frequency bistatic radar-occultation method for the study of planetary ionospheres. *Journal of Geophysical Research*, *70*(15), 3701–3710. doi.org/10.1029/JZ070i015p03701

Ho, S.-P., Anthes, R. A., Ao, C. O., Healy, S., Horanyi, A., Hunt, D., … Zeng, Z. (2019). The COSMIC/FORMOSAT-3 Radio Occultation Mission after 12 years: Accomplishments, Remaining Challenges, and Potential Impacts of COSMIC-2. *Bulletin of the American Meteorological Society*, *preprint*(2019). doi.org/10.1175/bams-d-18-0290.1

Hopfield, H. S. (1969). Two-Quartic Tropospheric Refractivity Profile for Correcting Satellite Data. *Journal of Geophysical Research*, *74*(18), 4487–4499. doi.org/10.1029/JC074i018p04487

Jin, S., Cardellach, E., & Xie, F. (2014). *Ocean Remote Sensing Using GNSS-R. In: GNSS Remote Sensing. Remote Sensing and Digital Image Processing* (Vol. 19). Springer, Dordrecht. doi.org/10.1007/978-94-007-7482-7_9

Klobuchar, A. J. (1991). Ionospheric Effects On GPS. *GPS World*, *2*(4), 48–51. doi.org/10.2514/5.9781600866388.0485.0515

Landskron, D. (2017). *Modeling tropospheric delays for space geodetic techniques (Ph.D. dissertation)*. Technischen Universitat Wien. Retrieved from https://resolver.obvsg.at/urn:nbn:at:at-ubtuw:1-100249

Landskron, D., & Böhm, J. (2017). VMF3/GPT3: refined discrete and empirical troposphere mapping functions. *Journal of Geodesy*, *92*(4), 349–360. doi.org/10.1007/s00190-017-1066-2

Larson, K. M. (2016). GPS interferometric reflectometry: applications to surface soil moisture, snow depth, and vegetation water content in the western United States. *Wiley Interdisciplinary Reviews: Water*, *3*(6), 775–787. doi.org/10.1002/wat2.1167

Larson, K. M., & Nievinski, F. G. (2012). GPS snow sensing: results from the EarthScope Plate Boundary Observatory. *GPS Solutions*, *17*(1), 41–52. doi.org/10.1007/s10291-012-0259-7

Larson, K. M., Ray, R. D., Nievinski, F. G., & Freymueller, J. T. (2013). The Accidental Tide Gauge: A GPS Reflection Case Study From Kachemak Bay, Alaska, *10*(5), 1200–1204. doi.org/10.1109/LGRS.2012.2236075

Larson, K. M., Ray, R. D., & Williams, S. D. P. (2017). A 10-Year Comparison of Water Levels Measured with a Geodetic GPS Receiver versus a Conventional Tide Gauge. *Journal of Atmospheric and Oceanic Technology*, *34*(2), 295–307. doi.org/10.1175/JTECH-D-16-0101.1

Larson, K. M., Wahr, J., & Munneke, P. K. (2015). Constraints on snow accumulation and firn density in

Greenland using GPS receivers. *Journal of Glaciology*, *61*(225), 101–114. doi.org/10.3189/2015JoG14J130

Li, M., Hinnov, L. A., Huang, C., & Ogg, J. G. (2018). Sedimentary noise and sea levels linked to land-ocean water exchange and obliquity forcing. *Nature Communications*, *9*(1). doi.org/10.1038/s41467-018-03454-y

Liu, L., & Larson, K. M. (2018). Decadal changes of surface elevation over permafrost area estimated using reflected GPS signals. *The Cryosphere*, *12*(2), 477–489. doi.org/10.5194/tc-12-477-2018

Lofgren, S. J. (2014). *Local Sea Level Observations Using Reflected GNSS Signals*. Chalmers University of Technology. Retrieved from http://publications.lib.chalmers.se/records/fulltext/191472/191472.pdf

Marini, J. W., & Murray, C. W., J. (1973). *(NASA-TM-T-70555) Correction of laser range tracking data for atmospheric refraction at elevations above 10 degrees*. *National Aeronautics and Space Administration NASA* (Vol. 60). National Aeronautics and Space Administration NASA.

Mayaki, A. O., Nikolaidou, T., Santos, M., & Okolie, C. J. (2018). Comparing the Nigerian GNSS Reference Network's Zenith Total Delays from Precise Point Positioning to a Numerical Weather Model. *International Association of Geodesy Symposia International Symposium on Advancing Geodesy in a Changing World*, *149*. doi.org/10.1007/1345_2018_43

McAdam, M. (2013). Implementation and Validation of a UNB Vienna Mapping Functions Service. M.Sc.E. thesis, Department of Geodesy and Geomatics Engineering Technical Report No. 284, University of New Brunswick, Fredericton, New Brunswick, Canada, 305 pp., (284).

Mitchum, G. T. (2000). An improved calibration of satellite altimetric heights using tide gauge sea levels with adjustment for land motion. *Marine Geodesy*, *23*(3), 145–166. doi.org/10.1080/01490410050128591

Nafisi, V., Urquhart, L., Santos, M. C., Nievinski, F. G., Bohm, J., Wijaya, D. D., … Gegout, P. (2012). Comparison of Ray-Tracing Packages for Troposphere Delays. *IEEE Transactions on Geoscience and Remote Sensing*, *50*(2), 469–481. doi.org/10.1109/TGRS.2011.2160952

National Academies of Sciences, Engineering, and M. 2018. (2018). *Thriving on Our Changing Planet*. *Thriving on Our Changing Planet: A Decadal Strategy for Earth Observation from Space*. Washington, D.C.: National Academies Press. doi.org/10.17226/24938

Niell, A. E. (1996). Global mapping functions for the atmosphere delay at radio wavelengths. *Journal of Geophysical Research: Solid Earth*, *101*(B2), 3227–3246. doi.org/10.1029/95JB03048

Nievinski, F. G. (2009). *Ray-tracing Options to Mitigate the Neutral Atmosphere Delay in GPS. (M.Sc.E. thesis).* Technical Report No. 262. University of New Brunswick.

Nievinski, F. G., & Larson, K. M. (2014a). Forward modeling of GPS multipath for near-surface reflectometry and positioning applications. *GPS Solutions*, *18*(2), 309–322. doi.org/10.1007/s10291-013-0331-y

Nievinski, F. G., & Larson, K. M. (2014b). Inverse Modeling of GPS Multipath for Snow Depth Estimation—Part I: Formulation and Simulations. *IEEE Transactions on Geoscience and Remote Sensing*, *52*(10), 6555–6563. doi.org/10.1109/TGRS.2013.2297681

Nievinski, F. G., & Santos, M. C. (2010). Ray-tracing options to mitigate the neutral atmosphere delay in GPS. *Geomatica*, *64*(2), 191–207.

Nikolaidou, T., Balidakis, K., Nievinski, F., Santos, M., & Schuh, H. (2018). Impact of different NWM-derived mapping functions on VLBI and GPS analysis Introduction and background. *Earth, Planets and Space*, *70*, 95. doi.org/10.1186/s40623-018-0865-x

Nikolaidou, T., Nievinski, F., Balidakis, K., Schuh, H., & Santos, M. (2018). PPP Without Troposphere Estimation: Impact Assessment of Regional Versus Global Numerical Weather Models and Delay Parametrization (pp. 1–12). Springer, Berlin, Heidelberg. doi.org/10.1007/1345_2018_44

Petit, G., & Luzum, B. (2010). IERS Conventions (2010). In G. P. and B. Luzum (Ed.), *International Earth*

Rotation and Reference Systems Service (IERS) Service International de la Rotation Terrestre et desSys emes de Référence IERS Conventions (2010). IERS Technical Note No. 36. Frankfurt am Main. Retrieved from https://www.iers.org/SharedDocs/Publikationen/EN/IERS/Publications/tn/TechnNote36/tn36.pdf;jsessionid=835D089F780AD79FEC5C1A69FD434DB5.live2?__blob=publicationFile&v=1

Rocken, C., Anthes, R., Exner, M., Hunt, D., Sokolovskiy, S., Ware, R., … Zou, X. (1997). Analysis and validation of GPS/MET data in the neutral atmosphere. *Journal of Geophysical Research: Atmospheres*, *102*(D25), 29849–29866. doi.org/10.1029/97JD02400

Roussel, N., Frappart, F., Ramillien, G., Darrozes, J., Desjardins, C., Gegout, P., … Biancale, R. (2014). Simulations of direct and reflected wave trajectories for ground-based GNSS-R experiments. *Geoscientific Model Development*, *7*(5), 2261–2279. doi.org/10.5194/gmd-7-2261-2014

Roussel, Nicolas, Ramillien, G., Frappart, F., Darrozes, J., Gay, A., Biancale, R., … Allain, D. (2015). Sea level monitoring and sea state estimate using a single geodetic receiver. *Remote Sensing of Environment*, *171*, 261–277. doi.org/10.1016/j.rse.2015.10.011

Rüeger, J. M. (2002). JS28 Integration of Techniques and Corrections to Achieve Accurate Engineering Refractive Index Formulae for Radio Waves Refractive Index Formulae for Radio Waves. *Proc. FIG XXII International Congress, Washington, D. C.*, 1–13. Retrieved from www.gmat.unsw.edu.au

Saastamoinen, J. (1972). Atmospheric Correction for the Troposphere and Stratosphere in Radio Ranging Satellites. In *Geophysical Monograph Series* (pp. 247–251). American Geophysical Union (AGU). doi.org/10.1029/GM015p0247

Santamaría-Gómez, A., & Watson, C. (2017). Remote leveling of tide gauges using GNSS reflectometry: case study at Spring Bay, Australia. *GPS Solutions*, *21*(2), 451–459. doi.org/10.1007/s10291-016-0537-x

Santamaría-Gómez, A., Watson, C., Gravelle, M., King, M., & Wöppelmann, G. (2015). Levelling co-located GNSS and tide gauge stations using GNSS reflectometry. *Journal of Geodesy*, *89*(3), 241–258. doi.org/10.1007/s00190-014-0784-y

Semmling, A. M., Schmidt, T., Wickert, J., Schn, S., Fabra, F., Cardellach, E., … Rius, A. (2012). On the retrieval of the specular reflection in GNSS carrier observations for ocean altimetry. *Radio Science*, *47*(6). doi.org/10.1029/2012RS005007

Semmling, M. (2012). *Altimetric Monitoring of Disko Bay using Interferometric GNSS Observations on L1 and L2 (Ph.D. thesis)*. Scientific Technical Report STR12/04. Deutsches GeoForschungsZentrum GFZ. doi.org/10.2312/GFZ.b103-12049

Siebentritt, M. (2016). *Understanding sea-level rise and climate change, and associated impacts on the coastal zone. CoastAdapt Information Manual 2*.

Siegfried, M. R., Medley, B., Larson, K. M., Fricker, H. A., & Tulaczyk, S. (2017). Snow accumulation variability on a West Antarctic ice stream observed with GPS reflectometry, 2007-2017. *Geophysical Research Letters*, *44*(15), 7808–7816. doi.org/10.1002/2017GL074039

Small, E. E., Larson, K. M., & Braun, J. J. (2010). Sensing vegetation growth with reflected GPS signals. *Geophysical Research Letters*, *37*(12). doi.org/10.1029/2010GL042951

Strandberg, J. (2020). *New methods and applications for interferometric GNSS reflectometry (Ph.D. thesis)*. Chalmers University of Technology.

Strandberg, J., Hobiger, T., & Haas, R. R. (2017). Coastal Sea Ice Detection Using Ground-Based GNSS-R. *IEEE Geoscience and Remote Sensing Letters*, *14*(9), 1552–1556. doi.org/10.1109/LGRS.2017.2722041

Tabibi, S., Nievinski, F. G., Van Dam, T., & Monico, J. F. G. (2015). Assessment of modernized GPS L5 SNR for ground-based multipath reflectometry applications. *Advances in Space Research*, *55*, 1104–1116. doi.org/10.1016/j.asr.2014.11.019

Thayer, G. D. (1974). An improved equation for the radio refractive index of air. *Radio Scienc*, *9*(10), 803–

807.

Tregoning, P., & van Dam, T. (2005). Atmospheric pressure loading corrections applied to GPS data at the observation level. *Geophysical Research Letters*, *32*(L22310,). doi.org/10.1029/2005GL024104

Treuhaft, R. N., Lowe, S. T., Zuffada, C., & Chao, Y. (2001). 2-cm GPS altimetry over Crater Lake. *Geophysical Research Letters*, *28*(23), 4343–4346. doi.org/10.1029/2001GL013815

Urquhart, L., Nievinski, F. G., & Santos, M. C. (2012). Ray-traced slant factors for mitigating the tropospheric delay at the observation level. *Journal of Geodesy*, *86*(2), 149–160. doi.org/10.1007/s00190-011-0503-x

Urquhart, L., Nievinski, F. G., & Santos, M. C. (2013). Assessment of troposphere mapping functions using three-dimensional ray-tracing. *GPS Solutions*, *18*(3), 345–354. doi.org/10.1007/s10291-013-0334-8

Urquhart, L., Santos, M. C., Nievinski, F. G., & Böhm, J. (2014). Generation and assessment of VMF1-type grids using North-American numerical weather models. In *International Association of Geodesy Symposia* (Vol. 139, pp. 3–9). doi.org/10.1007/978-3-642-37222-3_1

Wan, W., Larson, K. M., Small, E. E., Chew, C. C., & Braun, J. J. (2015). Using geodetic GPS receivers to measure vegetation water content. *GPS Solutions*, *19*(2), 237–248. doi.org/10.1007/s10291-014-0383-7

Williams, S. D. P., & Nievinski, F. G. (2017). Tropospheric delays in ground-based GNSS multipath reflectometry-Experimental evidence from coastal sites. *Journal of Geophysical Research: Solid Earth*, *122*(3), 2310–2327. doi.org/10.1002/2016JB013612

Yakovlev, O. I., Matyugov, S. S., & Vilkov, I. A. (1995). Attenuation and scintillation of radio waves in the Earth’s atmosphere from radio occultation experiments on satellite-to-satellite links. *Radio Science*, *30*(3), 591–602. doi.org/10.1029/94RS01920

Zavorotny, V. U., Gleason, S., Cardellach, E., & Camps, A. (2014). Tutorial on remote sensing using GNSS bistatic radar of opportunity. *IEEE Geoscience and Remote Sensing Magazine*, *2*(4), 8–45. doi.org/10.1109/MGRS.2014.2374220

Zus, F., Dick, G., Heise, S., & Wickert, J. (2015). A forward operator and its adjoint for GPS slant total delays. *Radio Science*, *50*(5), 393–405. doi.org/10.1002/2014RS005584

3. Raytracing atmospheric delays in ground-based GNSS reflectometry

Abstract[3]: Several studies have recognized that Global Navigation Satellite System Reflectometry (GNSS-R) are subject to atmospheric propagation delays. Unfortunately, there is little information in the peer-reviewed literature about the methods and algorithms involved in correcting for this effect. We have developed an atmospheric ray-tracing procedure to solve rigorously the three-point boundary value problem of ground-based GNSS-R observations. We defined the reflection-minus-direct or interferometric delay in terms of vacuum distance and radio length. We clarified the roles of linear and angular refraction in splitting the total delay in two components, along-path and geometric. We have introduced for the first time two subcomponents of the atmospheric delay, the geometry shift and geometric excess. We have defined corresponding atmospheric altimetry corrections necessary for unbiased altimetry retrievals. Using simulations, we examined the interferometric atmospheric delay for a range of typical scenarios, where it attained centimeter-level values at low satellite elevation angles ~ 5° for a 10-m high station. We found a linear and exponential dependence on reflector height and satellite elevation angle, respectively. A similar trend was found for the atmospheric altimetry correction, albeit with an amplified meter-level magnitude. The two delay components were similar near the horizon while the angular one vanished at zenith. For the altimetry correction components, both remained non-zero at zenith. We thus quantified the atmospheric bias in GNSS-R sea level retrievals.

---

[3] This chapter is based on the manuscript accepted for publication in the Journal of Geodesy: Nikolaidou, T., Santos, C. M., Williams, D. P. S., & Geremia-Nievinski, F., (2020). Raytracing atmospheric delays in ground-based GNSS reflectometry. Journal of Geodesy. https://doi.org/10.1007/s00190-020-01390-8.

3.1. Introduction

In positioning, navigation, and timing (PNT) using the Global Positioning System (GPS) and other Global Navigation Satellite Systems (GNSS), one often assumes that radio waves propagate along a straight line and at the speed of light in vacuum. Systematic deviations arise as GPS/GNSS waves get refracted in the atmosphere and possibly reflected on the earth’s surface. In GNSS PNT applications, these deviations are considered errors that need to be corrected, to achieve improved accuracy (Boehm and Schuh 2013). On the other hand, in GNSS remote sensing, the same refraction and reflection phenomena become sources of information for monitoring the environment. GNSS radio occultation (GNSS-RO) and other refractometric methods allow inferring air pressure, temperature and humidity as well as plasma electron density, based on propagation in the neutral and ionized layers of the atmosphere, respectively. GNSS reflectometry (GNSS-R) permits estimation of sea level, snow depth, soil moisture, and other geophysical parameters based on radio wave reflections off natural surfaces such as water and land (Zavorotny et al. 2014; Larson 2016).

The simultaneous occurrence of refraction and reflection in GNSS waves has been noted before (Boniface et al. 2011). Often one effect is of main interest while the other is considered a nuisance. For example, in GNSS-RO studies, reflections may contaminate atmospheric retrievals. Conversely, in GNSS-R altimetry retrievals of, e.g., sea level, atmospheric refraction may cause a bias compared to conventional tide gauges. Here we focus on ground-based or near-surface GNSS-R altimetry, from static or fixed stations (Larson et al. 2013;Larson et al. 2017).

Atmospheric refraction (sometimes called tropospheric refraction) includes the effect of speed retardation (linear refraction) and direction bending (angular refraction). The two effects depend on the index of refraction, on its mean value and spatial gradient, respectively. Both types may result in a signed atmospheric propagation delay as compared to the idealization of propagation in vacuum. The receiving GNSS antenna is typically not very directional nor is it aimed at any particular satellite, so angular refraction is only experienced indirectly via the resulting delay in pseudo-ranges and carrier-phase measurements.

In GNSS-R, one is specially interested in the reflection-minus-direct or interferometric propagation delay τ_i (Nievinski and Larson 2014a). The interferometric phase $\phi_i = 2\pi\lambda^{-1}\tau_i$ (at a given carrier wavelength λ) dictates the constructive and destructive interference pattern observed in the coherent superposition of the two radio waves (multipath reception) (Nievinski and Larson 2014b).

Several studies have recognized the importance of atmospheric errors in GNSS- R (Anderson 2000; Treuhaft et al. 2001; Fabra et al. 2012; Semmling et al. 2012; Roussel et al. 2014; Santamaría-Gómez et al. 2015; Santamaría-Gómez and Watson 2017). Most such studies claim to have corrected for atmospheric effects but show little information about the methods and algorithms involved. More recently, we have presented experimental evidence of systematic errors in GNSS-R altimetry retrievals (Williams and Nievinski 2017), where we examined deviations from tidal analysis at 22 GNSS stations as function of satellite elevation angle, time of year, and reflector height (the vertical distance between antenna and surface). Although at the time we tested both bent and rectilinear raytracing models, we accounted for angular refraction only approximately. A preliminary comparison to existing correction models was also made; unfortunately, those models were somewhat ad hoc, introduced based on heuristic justifications.

Here we offer a more rigorous derivation from first principles and a comprehensive evaluation of the atmospheric delay in GNSS-R, including the unification of its linear and angular components. The modelling of the interferometric atmospheric delay is presented in Section 2. The atmospheric altimetry correction derivation takes place also in the same section. Section 3 deals with the raytracing and its rigorous solution. Following, in Section 4 results are presented for the total delay as well as its components. Section 6 concludes the study.

3.2. Atmospheric Delay Modeling

3.2.1. Propagation Quantities

For line-of-sight propagation, the *direct vacuum distance*,

$$D_d = \|\boldsymbol{r}_{\text{ant}} - \boldsymbol{r}_{\text{sat}}\|, \tag{1}$$

is simply the vector length between position vectors of transmitting satellite, $\boldsymbol{r}_{\text{sat}}$, and receiving antenna, $\boldsymbol{r}_{\text{ant}}$. The *reflection vacuum distance*,

$$D_r = \|\boldsymbol{r}_{\text{ant}} - \boldsymbol{r}_{\text{sfc}}\| + \|\boldsymbol{r}_{\text{sfc}} - \boldsymbol{r}_{\text{sat}}\|, \tag{2}$$

is the sum of distances along incoming and outgoing directions, each similarly defined as the vector lengths invoving the surface reflection point, $\boldsymbol{r}_{\text{sfc}}$, in-between satellite and antenna (Figure 3.1). Finally, the *interferometric vacuum distance* is defined as the reflection-minus-direct difference,

$$D_i = D_r - D_d. \tag{3}$$

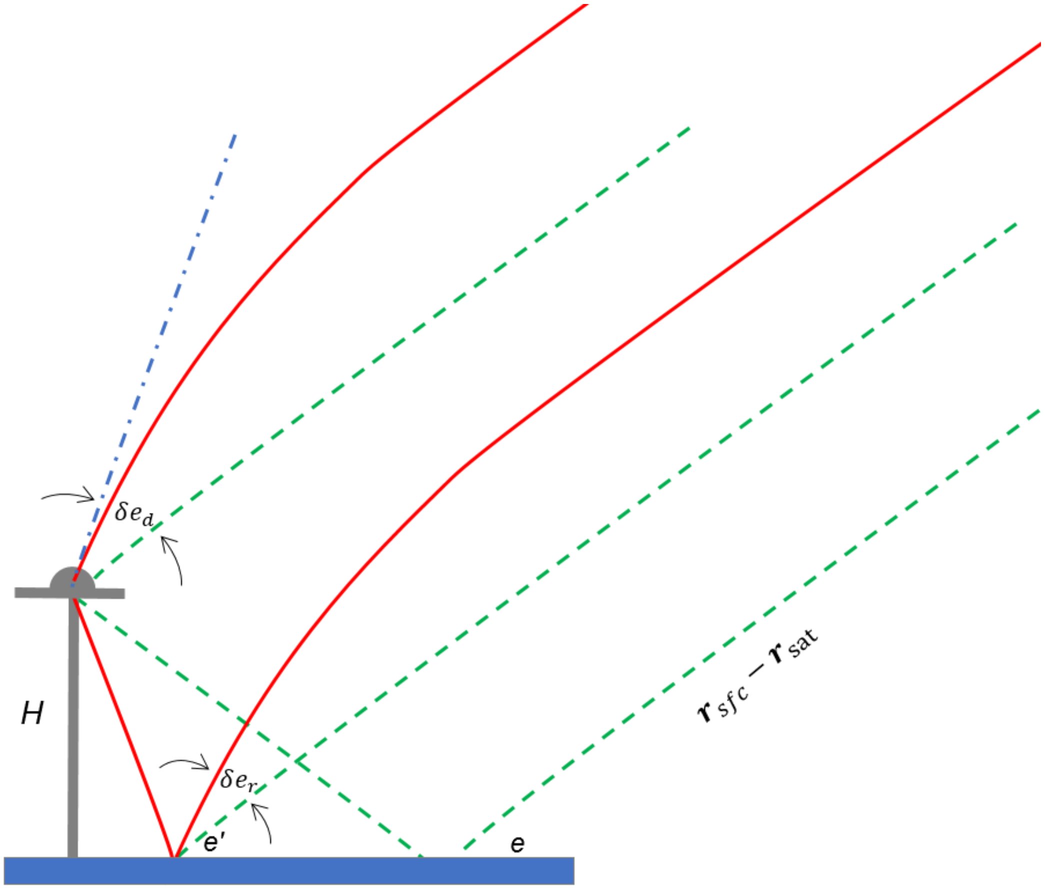

Figure 3.1: Geometric representation of the vacuum distance and geometric path length for direct, reflected and interferometric atmospheric delay in the vacuum and shifted-vacuum frames. The geometric incidence and apparent elevation angle are given by e and e' respectively; the distance between the antenna phase center (APC) and the reflecting surface – the reflector height – is denoted H.

Now replacing vacuum for an atmosphere, the *direct radio length*, L_d, is the integral of index of refraction n,

$$L_d = \int_{r_{\text{ant}}}^{r_{\text{sat}}} n \, dl, \tag{4}$$

where the integrand n is variable, evaluated along the bent ray path between satellite and antenna, of infinitesimal arc length dl. The ray trajectory is unknown and determined solving a differential equation, as described below. The resulting angular refraction implies a greater elevation angle e' than the vacuum satellite elevation angle e, where the (positive) elevation bending is:

$$\delta e = e' - e. \tag{5}$$

Similarly, the *reflection radio length*,

$$L_r = \int_{r'_{\mathrm{sfc}}}^{r_{\mathrm{sat}}} n\,dl + \int_{r_{\mathrm{ant}}}^{r'_{\mathrm{sfc}}} n\,dl, \tag{6}$$

is the sum of two integrals, along each incoming and outgoing paths. Its evaluation requires some care, because the reflection point on the surface must satisfy Snell's law, which shall be based on the apparent satellite elevation e'. Thus, angular refraction yields a displaced reflection point $\boldsymbol{r}'_{\mathrm{sfc}}$ which is closer to the antenna compared to the vacuum point $\boldsymbol{r}_{\mathrm{sfc}}$. The *interferometric radio length* is then simply:

$$L_i = L_r - L_d. \tag{7}$$

3.2.2. Total Atmospheric Delay

The *atmospheric delay* (also known as *tropospheric delay*),

$$d = L - D, \tag{8}$$

is defined as the difference between the radio length L and the vacuum distance D. It can be applied for direct or reflected rays, thus defining d_d and d_r, respectively. The *interferometric atmospheric delay*,

$$d_i = d_r - d_d \tag{9}$$

is the difference between reflection and direct atmospheric delays. Equivalently, it is also the difference between interferometric radio length and interferometric vacuum distance,

$$d_i = L_i - D_i. \tag{10}$$

It represents the discrepancy between what is observed in nature (L_i) and what would have happened in an idealized vacuum (D_i).

3.2.3. Atmospheric Delay Components

The total atmospheric delay is normally decomposed as

$$d = (L - R) + (R - D) = d^a + d^g, \tag{11}$$

with the introduction of the *curve range*

$$R = \int_{\boldsymbol{r}_1}^{\boldsymbol{r}_2} 1 \, dl \tag{12}$$

which is the total arc length of the bent ray path[4]. The first component of the total atmospheric delay is the *along-path atmospheric delay*:

$$d^a = L - R = \int_{\boldsymbol{r}_1}^{\boldsymbol{r}_2} N \, dl, \tag{13}$$

where $N = n - 1$ is the *refractivity* varying in the raypath, sometimes defined modulo 10^{-6} in the literature (Boehm and Schuh 2013).

The second component is the *geometric atmospheric delay*

$$d^g = R - D. \tag{14}$$

After Fermat's principle, in the presence of the atmosphere, propagation along the bent ray-path is faster than in a straight line, despite being geometrically longer ($R > D$). This decomposition (eq. 11) applies to any of the direct, reflected, or interferometric atmospheric delays, e.g., $d_i = d_i^a + d_i^g$.

---

[4] Where $\boldsymbol{r}_1$ and $\boldsymbol{r}_2$ arbitrary vector positions denoting the first and the final position of the raypath (e.g., $\boldsymbol{r}_1 = \boldsymbol{r}_{\text{ant}}$, $\boldsymbol{r}_2 = \boldsymbol{r}_{\text{sat}}$).

3.2.4. Atmospheric Altimetry Correction

In practice, field measurements involve the total interferometric delay, τ_i, and corresponding phase, ϕ_i, which are driven essentially by the interferometric radio length $L_i = D_i + d_i$. Here we neglect smaller contributions from the antenna radiation pattern and the surface reflection coefficients (Nievinski and Larson 2014a).

Naïve GNSS-R altimetry retrievals $\hat{H}$ that assume vacuum propagation will be biased compared to the true reflector height H. There is a need for an *atmospheric altimetry correction* $\Delta H = H - \hat{H}$ to recover the unbiased reflector height. Its definition depends on the altimetry retrieval method employed, as follows.

Normally one assumes a horizontal surface model, for which the interferometric vacuum distance is simply $D_i = 2H \sin e$. Reflector height may be retrieved from field measurements either via the absolute-ratio formula:

$$\hat{H} = \frac{1}{2}\frac{\tau_i}{\sin e} \approx \frac{1}{2}\frac{L_i}{\sin e} = H + \frac{1}{2}\frac{d_i}{\sin e} \tag{15}$$

or via the rate-of-change formula:

$$\hat{H} = \frac{1}{2}\frac{\partial \tau_i}{\partial \sin e} \approx \frac{1}{2}\frac{\partial L_i}{\partial \sin e} = H + \frac{1}{2}\frac{\partial d_i}{\partial \sin e} \tag{16}$$

The former (15) requires phase measurements to be unwrapped and ambiguity-fixed. The latter (17) is based on the interferometric delay-rate $\dot{\tau}_i = \partial \tau_i / \partial t$ (or interferometric Doppler scaled by carrier wavelength (Nievinski and Larson 2014a)):

$$\Delta H = -\frac{1}{2}\frac{\partial d_i / \partial e}{\cos e} = -\frac{1}{2}\frac{\dot{d}_i}{\dot{e} \cos e} \tag{17}$$

where a moving satellite is assumed, $\dot{e} = \partial e / \partial t \neq 0$. The derivative may be evaluated numerically given a series of delay values versus elevation angle. The two altimetry retrieval methods above correspond, respectively, to the "anchoring" and "stopping" approaches of GNSS-R carrier-phase altimetry in general (Zavorotny et al. 2014, p.32).

Like the total atmospheric delay, the total atmospheric altimetry correction can be split in its along-path and geometrical components: $\Delta H = \Delta H^a + \Delta H^g$. For the same positive interferometric atmospheric delay d_i, the absolute-ratio retrieval method (15) will overestimate the vacuum height H while the rate-of-change retrieval (16) will underestimate H. We will focus on the latter because it affects GNSS-R techniques that employ signal-to-noise (SNR) as observable, known as GNSS interference pattern technique or GNSS interferometric reflectometry. It also affects other observables, such as carrier-phase, collected under multipath reception conditions, in the broader class of GNSS multipath reflectometry techniques. A variety of retrieval algorithms exist (Geremia-Nievinski & Hobiger, 2020), the simplest of which is based on the spectral analysis of detrended SNR observations to find the best-fitting sinusoid, whose frequency is proportional to the reflector height, under the assumption of a planar reflector.

3.3. Interferometric Raytracing

3.3.1. Direct Raytracing

The interferometric raytracing software has been developed based on Nievinski and Santos (2010), originally developed for direct or line-of-sight raytracing only. The bent ray path is determined solving the Eikonal equation (Born and Wolf 1999):

$$\frac{\partial(n\,\hat{\boldsymbol{t}})}{\partial l} = \boldsymbol{\nabla} n \tag{18}$$

where $\hat{\boldsymbol{t}} = \partial \boldsymbol{r}/\partial l$ is the ray tangent direction, $\boldsymbol{r}$ is the evolving ray vector position, l is the incremental arc length, and $\boldsymbol{\nabla} n = \boldsymbol{\nabla} N$ is the spatial gradient of index of refraction or refractivity.

Postulating spherical atmospheric symmetry imposes the direction of the gradient of refractivity to point towards the center of the sphere:

$$\frac{\boldsymbol{\nabla} n}{\|\boldsymbol{\nabla} n\|} = -\frac{\boldsymbol{r}'}{\|\boldsymbol{r}'\|} \tag{19}$$

where $\boldsymbol{r}' = \boldsymbol{r} - \boldsymbol{r}_o$ is a vector position with respect to the center of the osculating sphere. This causes the ray path to become a plane curve and would allow a simplified raytracing formulation (2D), but we retain the 3D expressions because of their versatility in allowing lifting the assumption of spherical symmetry in the future.

The index of refraction n slows down the radio wave (via the atmospheric speed of propagation $v = c/n$, where c is the vacuum speed of light), while its spatial gradient $\boldsymbol{\nabla} n$ changes the direction of propagation (Nievinski and Santos 2010). We call these two radio propagation delay effects linear refraction and angular refraction, respectively, as both are formulated in terms of the index of refraction. Similar effects arise from the calculation of power attenuation due to atmospheric extinction, as in the calculation of air mass and path loss in the astronomy and electrical engineering literature.

Equation (18) specifies only the change in the ray position; to obtain the whole ray trajectory, one needs to specify initial or boundary conditions, as well. It involves specifying the moving ray tangent direction $\hat{\boldsymbol{t}}$ at a given arc length l^*. The minimum and maximum arc length l^* are, respectively zero (at the antenna) and near infinite (towards the transmitting GNSS satellite); the latter is approximated by the slant distance up to the satellite orbital radius (Nievinski, 2009, p.168).

We start ignoring the reflection and raytracing only the direct ray first. The user inputs a given satellite relative direction $\Delta\hat{\boldsymbol{r}}_{\text{sat}}$ (or elevation angle and azimuth, in local spherical coordinates). Normally this is the vacuum or geometric direction, as calculated from the antenna position $\boldsymbol{r}_{\text{ant}}$ and satellite position $\boldsymbol{r}_{\text{sat}}$ (interpolating ephemeris at a given epoch):

$$\Delta\hat{\boldsymbol{r}}_{\text{sat}} = \frac{\boldsymbol{r}_{\text{sat}} - \boldsymbol{r}_{\text{ant}}}{\|\boldsymbol{r}_{\text{sat}} - \boldsymbol{r}_{\text{ant}}\|} \tag{20}$$

The direct ray trajectory is then solved as a two-point boundary-value problem (BVP):

$$\text{BVP}_{\text{d}}\colon \begin{cases} \boldsymbol{r}_{\text{d}}^{0} = \boldsymbol{r}|_{l=0} = \boldsymbol{r}_{\text{ant}} \\ \hat{\boldsymbol{t}}_{\text{d}}^{\infty} = \hat{\boldsymbol{t}}|_{l\to\infty} = \boldsymbol{\Delta}\hat{\boldsymbol{r}}_{\text{sat}} \end{cases} \tag{21}$$

The direct BVP is solved via the iterative shooting method, which involves solving internally a simpler initial-value problem (IVP):

$$\text{IVP}_{\text{d}}\colon \begin{cases} \boldsymbol{r}_{\text{d}}^{0} = \boldsymbol{r}|_{l=0} = \boldsymbol{r}_{\text{ant}} \\ \hat{\boldsymbol{t}}_{\text{d}}^{0} = \hat{\boldsymbol{t}}|_{l=0} = \boldsymbol{\Delta}\hat{\boldsymbol{r}}'_{\text{sat}} \end{cases} \tag{22}$$

The ray tangent direction at the antenna $\hat{\boldsymbol{t}}_{\text{d}}^{0}$, also called the apparent or refracted satellite direction $\Delta\hat{\boldsymbol{r}}'_{\text{sat}}$, is specified as input in the IVP but is unknown in the BVP. So it gets initialized with the geometric direction as a first guess, $\hat{\boldsymbol{t}}_{\text{d}}^{0}[\text{IVP}; i = 0] \leftarrow \Delta\hat{\boldsymbol{r}}_{\text{sat}}$, and then it is updated iteratively for $i = 1, 2, \ldots$ based on the resulting geometric or vacuum direction mismatch $\hat{\boldsymbol{t}}_{\text{d}}^{\infty}$ across IVP output and BVP input:

$$\begin{gathered} \delta\hat{\boldsymbol{t}}_{\text{d}}^{\infty} = \hat{\boldsymbol{t}}_{\text{d}}^{\infty}[\text{IVP}, i] - \hat{\boldsymbol{t}}_{\text{d}}^{\infty}[\text{BVP}, i] \\ \hat{\boldsymbol{t}}_{\text{d}}^{0}[\text{IVP}; i + 1] \leftarrow \hat{\boldsymbol{t}}_{\text{d}}^{0}[\text{IVP}, i] - \delta\hat{\boldsymbol{t}}_{\text{d}}^{\infty} \end{gathered} \tag{23}$$

As stopping criterion, we check the absolute change in integrated delay against an input tolerance, normally 0.5 mm.

In its turn, the IVP is solved via a perturbed quadrature approach (Nievinski and Santos, 2010; Nafisi et al. 2012). This is an alternative to the application of ordinary differential equation solvers, such as Runge–Kutta methods, which is faster when the effect of curvature is mild. The raypath is initialized as a straight-line segment between receiver and satellite. Refractivity is evaluated by interpolation in the atmospheric model at steps determined either via adaptive quadrature (Espelid 2007) or at pre-defined non-uniform steps (smaller at low altitudes and larger aloft, as the ray reaches the limits of the atmosphere where refractivity is minimal). Finally, the previous raypath approximation gets updated with curvature corrections based on the component of the gradient of refractivity perpendicular to the tangent direction $\hat{\boldsymbol{t}}_j$ at each point of the raypath. For more details, please see Nievinski (2009, p.155-193).

The direct ray trajectory is thus determined; as a by-product, we also have the direct bending angle $\delta e_d = e'_d - e_d$ between refracted and vacuum satellite directions, as well as a series of refractivity values N_j discretized at increasing arc length values l_j. The direct along-path atmospheric delay is evaluated via numerical quadrature, such as a simple trapezoidal rule:

$$d_d^a = \int N\, dl \approx \sum N_j \cdot (l_{j+1} - l_{j-1})/2 \qquad (24)$$

On the other hand, the direct geometric atmospheric delay follows in principle from the difference between the arc length at the satellite and the vacuum distance,

$$d_d^g = R_d - D_d = l_{\mathrm{d/sat}} - \|\boldsymbol{r}_{\mathrm{sat}} - \boldsymbol{r}_{\mathrm{ant}}\| \qquad (25)$$

In practice, though, the raypath is not guaranteed to contain $\boldsymbol{r}_{\mathrm{sat}}$ exactly, as the convergence criterion allows for deviations within a given tolerance. The best approximation possible is provided by the ray–satellite pericenter or point of closest approach, $\boldsymbol{r}_{\mathrm{pc}}$, defined as the orthogonal projection of the satellite position to the raypath (Nievinski, 2009, p.168-169). Although it may affect the calculation of the vacuum distance, it is more consistent with the raytraced curve range. Recalling that the raypath is a semi-infinite half-line in outer space (above the top of the atmosphere), the pericenter can be found as:

$$\boldsymbol{r}_{\mathrm{pc}} = \boldsymbol{r}_{\mathrm{pp}} + \hat{\boldsymbol{t}}_{\mathrm{pc}}\left(\boldsymbol{r}_{\mathrm{sat}} - \boldsymbol{r}_{\mathrm{pp}}\right) \cdot \hat{\boldsymbol{t}}_{\mathrm{pp}} \tag{26}$$

It involves the atmospheric piercing point $\boldsymbol{r}_{\mathrm{pp}}$, where the ray exits the atmosphere (at an altitude of about 100 km), as well as the ray tangent direction at that point $\hat{\boldsymbol{t}}_{\mathrm{pp}}$. Finally, the direct geometric atmospheric delay can be evaluated as:

$$d_d^g \cong l_{\mathrm{pc}} - \left\|\boldsymbol{r}_{\mathrm{pc}} - \boldsymbol{r}_{\mathrm{ant}}\right\|. \tag{27}$$

The original BVP condition of parallelism $\hat{\boldsymbol{t}}|_{l\to\infty} = \boldsymbol{\Delta}\hat{\boldsymbol{r}}_{\mathrm{sat}}$ is strictly valid for a transmitter at a practically infinite distance. It can be evaluated at the piercing point or at the pericenter, $\hat{\boldsymbol{t}}|_{l_{\mathrm{pp}}} = \hat{\boldsymbol{t}}|_{l_{\mathrm{pc}}} = \boldsymbol{\Delta}\hat{\boldsymbol{r}}_{\mathrm{sat}}$; the equivalence follows from the uniformity in the ray tangent direction outside the atmosphere, where there is no bending. In this case, the geometric atmospheric delay can be further simplified to involve the piercing point (Nievinski, 2009, p.182-185).

The finite distance to transmitter can be accounted for more rigorously by a slight reformulation of the BVP,

$$\mathrm{BVP_d}: \begin{cases} \boldsymbol{r}_{\mathrm{d}}^0 = \boldsymbol{r}_{\mathrm{ant}} \\ \boldsymbol{\Delta}\hat{\boldsymbol{r}}_{\mathrm{pc}} = \boldsymbol{\Delta}\hat{\boldsymbol{r}}_{\mathrm{sat}} \end{cases} \tag{28}$$

It specifies equality between the viewing direction to the pericenter and the viewing direction to the satellite, in terms of the relative directions with respect to the receiving antenna (Nievinski, 2009, p.171-172):

$$\Delta\hat{\boldsymbol{r}}_{\mathrm{pc}} = \left(\boldsymbol{r}_{\mathrm{pc}} - \boldsymbol{r}_{\mathrm{ant}}\right) / \left\|\boldsymbol{r}_{\mathrm{pc}} - \boldsymbol{r}_{\mathrm{ant}}\right\| \tag{29}$$

For GNSS orbits, the assumption of near infinite distance leads to negligible errors in direct raytracing (Zus et al. 2015; Yan and Wang 1999; Ifadis 2000). But it raises the question of whether this effect is also negligible for reflection raytracing, which is more sensitive to the bending angle δe.

3.3.2. Reflection Raytracing

The reflection raytracing is performed separately for each of the incident and scattered legs, also known as incoming and outgoing segments, split at the reflection point, in-between satellite and receiving antenna. The reflection point is calculated based on the height of the antenna above the surface as well as the satellite elevation angle. Azimuth is not involved, as the surface is postulated planar and horizontal (leveled), based on a plane tangent to the ellipsoid. Furthermore, the atmospheric model is azimuthally symmetric (as detailed below). In this case, the reflection direction is the mirror image of the satellite direction, $e_r = -e_d$. Figure 3.1 summarizes the reflection geometry under atmospheric and vacuum conditions.

The type of satellite elevation angle input in the reflection point calculation is always the apparent or refracted one e', thus resulting in a refracted reflection point $\boldsymbol{r}'_{\mathrm{sfc}}$, different than the vacuum reflection point $\boldsymbol{r}_{\mathrm{sfc}}$. The solution for the reflection IVP is specified separately for each incoming and outgoing parts:

$$\mathrm{IVP}_{\mathrm{r/inc}} : \begin{cases} \boldsymbol{r}^{0}_{\mathrm{r/inc}} = \boldsymbol{r}'_{\mathrm{sfc}} \\ \hat{\boldsymbol{t}}^{\infty}_{\mathrm{r/inc}} = \Delta\hat{\boldsymbol{r}}'_{\mathrm{sat}} \end{cases} \tag{30}$$

$$\mathrm{IVP}_{\mathrm{r/out}} : \begin{cases} \boldsymbol{r}^{0}_{\mathrm{r/out}} = \boldsymbol{r}'_{\mathrm{sfc}} \\ \hat{\boldsymbol{t}}^{\infty}_{\mathrm{r/out}} = -\Delta\hat{\boldsymbol{r}}'_{\mathrm{sfc}} \end{cases} \tag{31}$$

where the relative direction to the surface with respect to the antenna is:

$$\boldsymbol{\Delta}\hat{\boldsymbol{r}}'_{\text{sfc}} = \frac{\boldsymbol{r}'_{\text{sfc}} - \boldsymbol{r}_{\text{ant}}}{\left\|\boldsymbol{r}'_{\text{sfc}} - \boldsymbol{r}_{\text{ant}}\right\|} \tag{32}$$

The slant distance from the antenna to the refracted reflection point is simply[5]

$$\Delta r'_{\text{sfc}} = \|\boldsymbol{r}'_{\text{sfc}} - \boldsymbol{r}_{\text{ant}}\| = H/\sin e'. \tag{33}$$

Now, for the reflection raytracing to be compatible with the direct raytracing – meaning the receiver to be able to track both rays simultaneously – we must solve a reflection BVP imposing the following constraints:

(1) Snell's law – incident and scattered apparent elevation angles are equal;

(2) scattered ray reaches the receiving antenna – negligible distance to the antenna on the ray final point;

(3) incident ray reaches the satellite – reflection vacuum elevation equals direct vacuum elevation.

The last requirement implies that reflection elevation bending $\delta e_r = e'_r - e_r$ is not necessarily the same as the direct elevation bending δe_d, if the vacuum satellite elevation e is to be unique and the same. We start with initial guesses at $i = 0$ for the reflection apparent elevation angle $e'_r \leftarrow e'_d$ and for the corresponding reflection point $\boldsymbol{r}'_{\text{sfc}}$. These approximations are then updated until convergence, effectively displacing the reflection point horizontally until condition (2) above is satisfied.

Finally, the reflection along-path atmospheric delay $d_r^a = L_r - R_r$ is obtained by straightforward summation of the incoming and outgoing contributions, each obtained similarly as for the direct path formulation:

---

[5] A straight-line propagation is assumed or equivalently negligible ray bending, for atmospheric layer of thickness up to few tens of meters

$$d_r^a = d_{\mathrm{r/inc}}^a + d_{\mathrm{r/out}}^a \tag{34}$$

On the other hand, the reflection geometric atmospheric delay:

$$d_r^g = R_r - D_r \tag{35}$$

requires some care, as it involves the vacuum distance D_r. When repurposing a conventional, direct-only raytracing software for reflection raytracing, the software may be unaware that it has been input a refracted reflection point instead of the vacuum reflection point. So, the raytracing output will be actually only part of the geometric delay:

$$d_r^{g'} = R_r - D_r' \tag{36}$$

which we call *reflection geometric-excess atmospheric delay*, where the shifted vacuum distance is define as:

$$D_r' = \|\boldsymbol{r}_{\mathrm{ant}} - \boldsymbol{r}'_{\mathrm{sfc}}\| + \|\boldsymbol{r}'_{\mathrm{sfc}} - \boldsymbol{r}_{\mathrm{sat}}\|. \tag{37}$$

The missing part

$$d_r^{g''} = D_r' - D_r \tag{38}$$

is here called *reflection geometric-shift atmospheric delay* and must be restored so as to obtain the total reflection geometric atmospheric delay from its two subcomponents as:

$$d_r^g = d_r^{g'} + d_r^{g''} \tag{39}$$

To make things slightly more complicated, in numerical practice the reflection raypath defines new pericenters, one along each incident and scattered legs, so we end up having approximations such as:

$$d_{\mathrm{r/inc}}^{g'} \approx l_{\mathrm{pc-r/inc}} - \left\|\boldsymbol{r}_{\mathrm{pc-r/inc}} - \boldsymbol{r}'_{\mathrm{sfc}}\right\|$$

$$d_{\mathrm{r/out}}^{g'} \approx l_{\mathrm{pc-r/out}} - \left\|\boldsymbol{r}_{\mathrm{pc-r/out}} - \boldsymbol{r}'_{\mathrm{sfc}}\right\|$$

$$d_{\mathrm{r/out}}^{g''} \approx \|\boldsymbol{r}_{\mathrm{ant}} - \boldsymbol{r}'_{\mathrm{sfc}}\| - \|\boldsymbol{r}_{\mathrm{ant}} - \boldsymbol{r}_{\mathrm{sfc}}\|$$

$$d_{\mathrm{r/inc}}^{g''} \approx \|\boldsymbol{r}'_{\mathrm{sfc}} - \boldsymbol{r}_{\mathrm{pc-d}}\| - \|\boldsymbol{r}_{\mathrm{sfc}} - \boldsymbol{r}_{\mathrm{pc-d}}\|$$

For consistency with the direct raypath, we use the latter's pericenter $\boldsymbol{r}_{\mathrm{pc-d}}$ when calculating the reflection geometric-shift atmospheric delay on the incident leg.

3.4. Results and Discussion

Here we present simulations of the main results.

3.4.1. Atmospheric Model

As atmospheric model source, we employed the COSPAR International Reference Atmosphere 1986 (CIRA-86) climatology (Chandra et al. 1990; Fleming et al. 1990). It provides temperature (0-120 km) and pressure (20-120 km) at 5-km intervals; surface pressure is obtained via hydrostatic integration. Temperature and pressure at any other sampling point is obtained via linear and log-linear interpolation, respectively.

Humidity is unavailable in this climatology thus left for future work. Dry gases are known to be responsible for the majority of the atmospheric delay in radio propagation and to remain relatively stable over time and space. In contrast, humidity has a smaller contribution and is highly variable. Therefore, we expect the present study to represent well the bulk of the atmospheric effect in ground-based GNSS-R.

In principle CIRA-86 depends on altitude, latitude and month, with no dependence on longitude and year. We also leave geographical and temporal variations for future work. We only extracted a single vertical profile at a fixed location and epoch: zero latitude and beginning of year (Figure 3.2).

We postulate an atmospheric structure with azimuthal symmetry around the antenna. It is based on an osculating spherical Earth, normal to the Earth's ellipsoid and with Gaussian radius of curvature (Nievinski and Santos 2010). Refractivity is computed from $N_d = 10^{-6}\, k_1\, P_d/T$, where k_1 is an empirical coefficient equal to $77.6890\ 10^{-2}\ \mathrm{K} \cdot \mathrm{Pa}^{-1}$ (Rüeger 2002); P_d (in pascals) is the partial pressure due to dry gases including CO_2 and T (in kelvin) is the temperature.

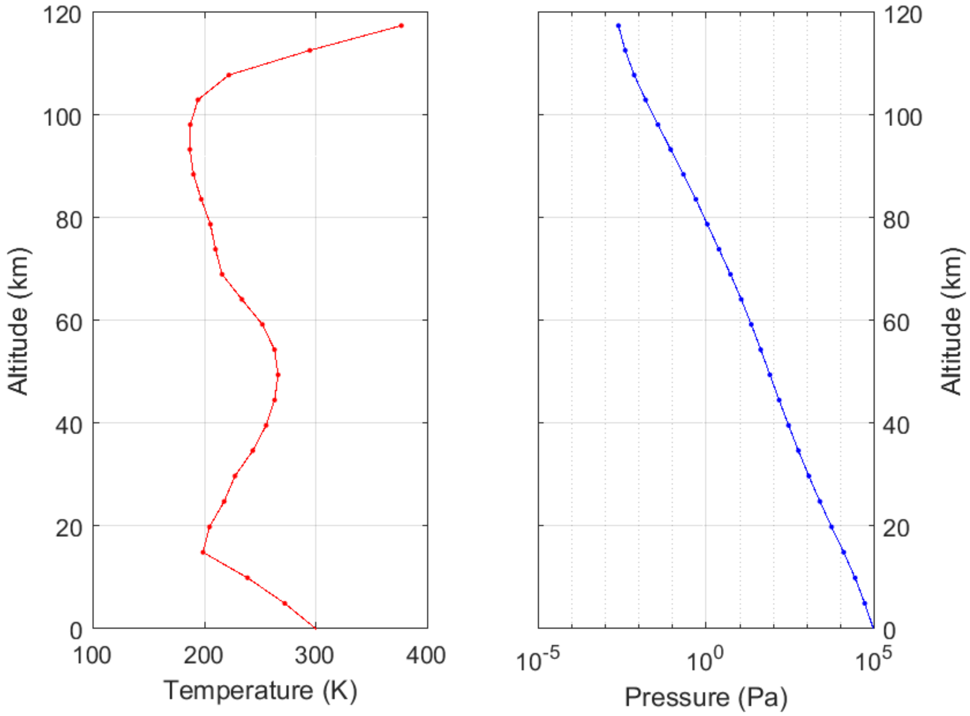

Figure 3.2: Temperature and pressure profiles extracted from CIRA-86

3.4.2. Propagation Quantities

For a fixed reflector height (10 m), we start by illustrating in Figure 3.3 the definition of interferometric atmospheric delay $d_i = L_i - D_i$ given in (10), showing the terms of the difference between two interferometric propagation quantities. The interferometric radio length $L_i = L_r - L_d$ and the interferometric vacuum distance $D_i = D_r - D_d$ each follows from the subtraction of the corresponding reflection and direct propagation quantities (not shown). Notice that $L_i > D_i$, i.e., the propagation takes longer in the atmosphere compared to a vacuum, so that the interferometric atmospheric delay is positive. The interferometric vacuum distance equals twice the reflector height at zenith, $D_i|_{e=90^\circ} = 2H$, and decreases to zero towards the horizon, where the two paths become parallel. The radio length L_i also decreases with elevation angle but less rapidly, causing an increased separation with respect to the vacuum distance D_i at low elevation angles.

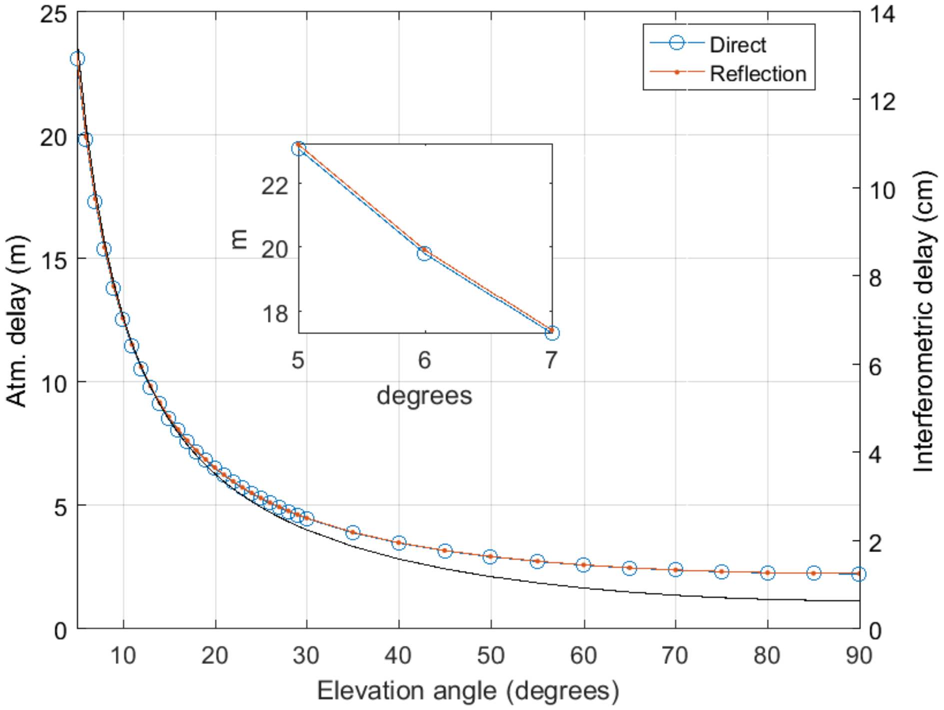

Figure 3.3: Interferometric delay as the difference between interferometric radio length and interferometric vacuum distance (for a fixed 10-m reflector height); inset shows a zoom in the lowest elevation angles.[6]

---

[6] The colored and marked lines correspond to the right axis while the black solid line to the left.

Figure 3.4 illustrates the alternative definition of interferometric atmospheric delay, $d_i = d_r - d_d$, given in (9), following from difference between reflection and direct atmospheric delays. The reflection atmospheric delay $d_r = L_r - D_r$ and the direct atmospheric delay $d_d = L_d - D_d$ each results from the excess travel time that the corresponding ray undergoes in order to reach the antenna, i.e., both d_r and d_d represent the difference across atmospheric and vacuum propagation conditions. At zenith, they are about 2.3 m and reach ten times more at 5-degree elevation. The reflection ray travels longer and partially in denser air portions in the lower atmospheric layers compared to the direct ray. Thus $d_r > d_d$, and the effect of refraction (both linear and angular) is greater on the reflected path rather than on the direct one, which is another reason why the interferometric atmospheric delay is positive.

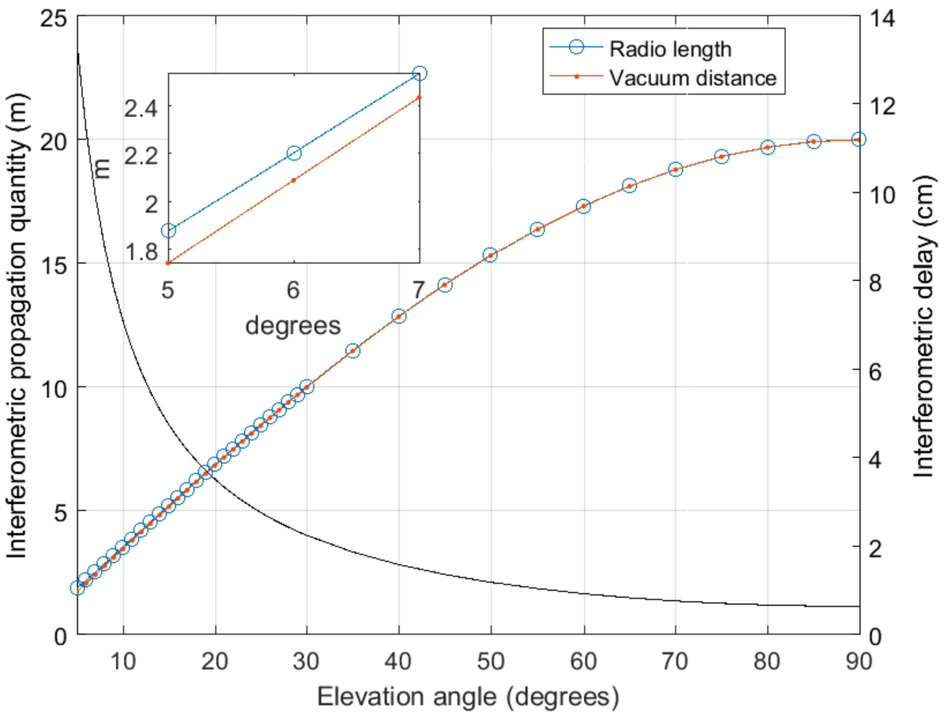

Figure 3.4: Interferometric atmospheric delay as the difference between reflected atmospheric delay and direct atmospheric delay (for a fixed 10-m reflector height); inset shows a zoom in the lowest elevation angles.[7]

Figure 3.5 shows the direct elevation bending $\delta e_d = e'_d - e_d$, which is always positive, i.e., the satellite appears higher in the sky under the atmosphere, compared to what would be observed in vacuum. The reflected ray bending δe_r (not shown) is slightly greater than the direct one. Their difference, $\delta e_i = \delta e_r - \delta e_d = e'_r - e'_d$, is the interferometric bending and is shown on the right-hand side vertical axis of Figure 3.5. It is a thousand times smaller and in fact it seems a downscaled version of δe_d (above 30-degree elevation it might be corrupted by numerical noise). It should be noted that δe_i scales with reflector height H (not shown), while δe_d is mostly independent of it.

---

[7] The colored and marked lines correspond to the right axis while the black solid line to the left.

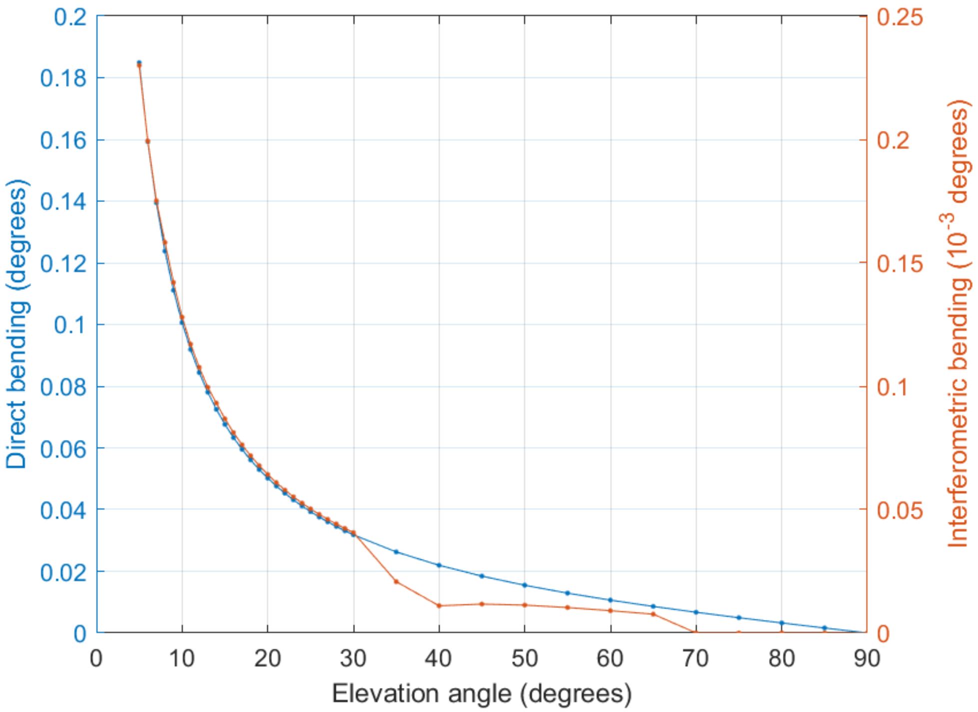

Figure 3.5: Direct (left axis) and interferometric (right axis) bending in degrees and 10-3 degrees respectively (for a fixed 10- m reflector height).

We have also assessed the impact of the assumption of infinite distance to transmitting satellite (no figure included). For a 10-m high reflector the lowest satellite elevation (5 degrees) has a micrometer level discrepancy in interferometric total delay, only about 4 μm. It is much greater in the direct total interferometric delay, reaching about 0.8 mm, but it is slightly greater in the reflection path, thus nearly canceling out when forming the difference. Even at 1-km height, the effect on interferometric delay remains sub-mm.

3.4.3. Total Atmospheric Delay and Altimetry Correction

Figure 3.6 demonstrates that the total interferometric atmospheric delay, d_i, increases with decreasing elevation angle. This follows primarily from a similar behavior in elevation bending with elevation angle. Yet towards zenith, d_i converges to a non-zero asymptote ($d_i|_{e=90^\circ} \neq 0$) despite having negligible bending ($\delta e \approx 0$); this finding indicates the presence of linear refraction effects in addition to angular refraction, as explored below. For a given reflector height, the total interferometric delay decreases seemingly exponentially with elevation angle (Figure 3.6, top).

Conversely, for a fixed elevation angle, the total interferometric atmospheric delay is nearly linearly proportional to the reflector height (Figure 3.6, bottom). At 50-m reflector height, the value of d_i is about 30 cm at 10-degree elevation and ten times less near zenith.

The atmospheric altimetry correction (following the rate-of-change definition (16)) is shown in Figure 3.7 and represents a variably-scaled version of the atmospheric delay. It increases linearly with reflector height and decreases exponentially with elevation angle. Compared to the delay, the altimetry correction has a much larger magnitude. For a 50-m reflector height, the correction reaches about one meter at 10-degree elevation and less than 5 cm at zenith.

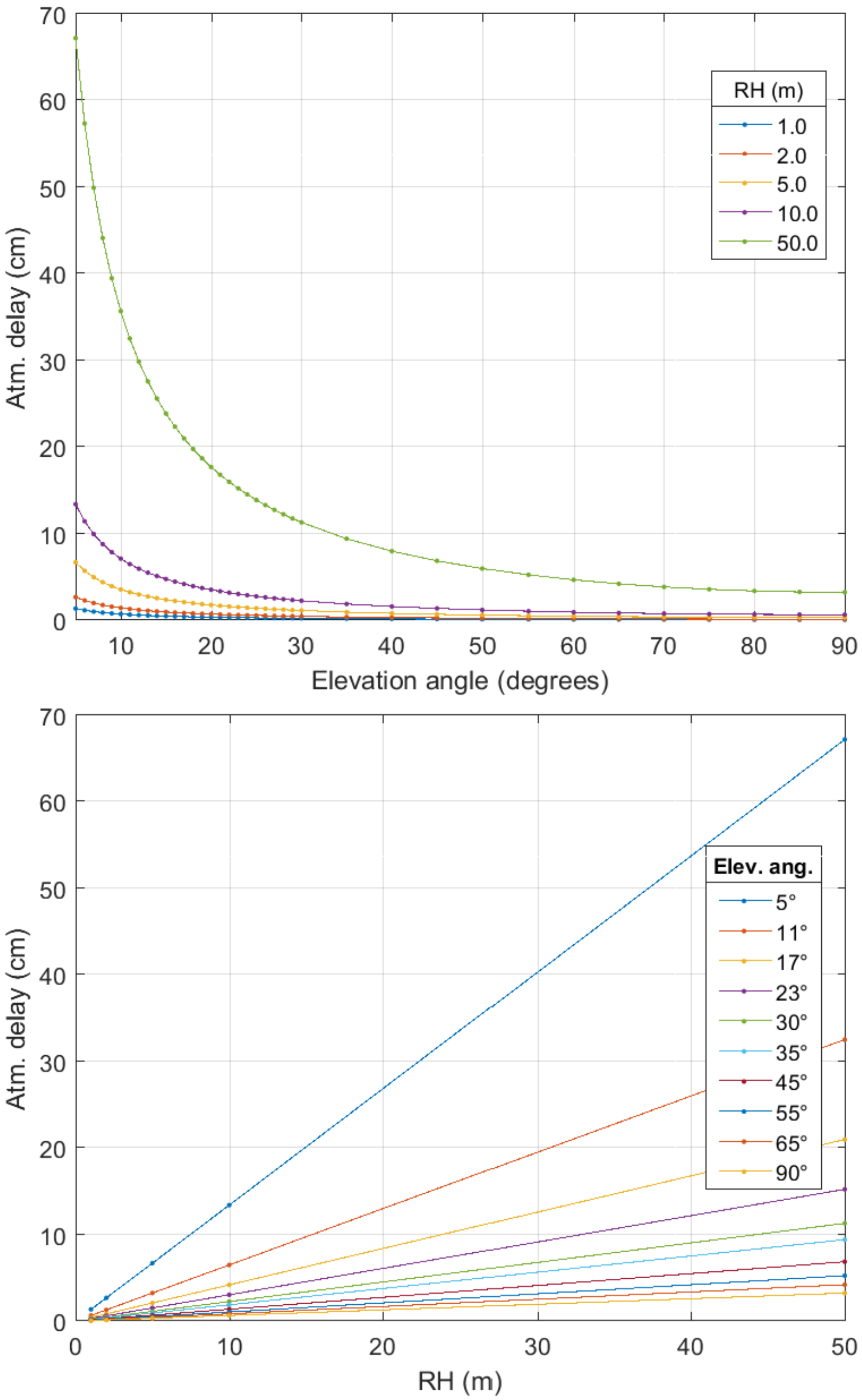

Figure 3.6: Total interferometric atmospheric delay as a function of satellite elevation angle and for varying reflector height (top) and as a function of reflection height for varying satellite elevation (bottom) .

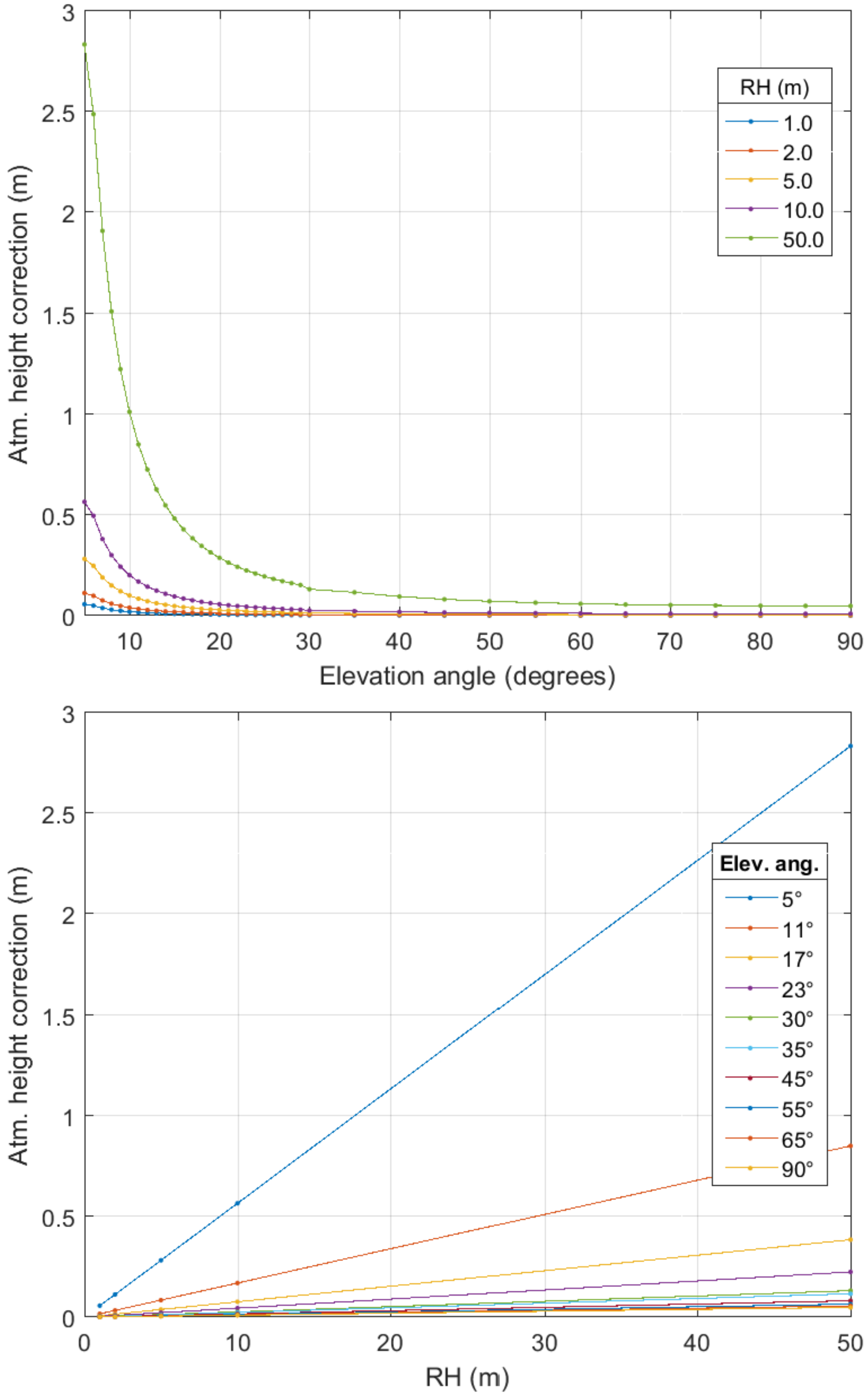

Figure 3.7: Total interferometric atmospheric altimetry correction as a function of satellite elevation angle for varying reflector height (top) and as a function of reflection height for varying satellite elevation (bottom) .

3.4.4. Components of the Atmospheric Delay and Altimetry Correction

In Figure 3.8 we examine the components of the total interferometric delay $d_i = L_i - D_i$; for clarity, we focus on a single reflector height value ($H = 10$ m). The interferometric geometric atmospheric delay $d_i^g = R_i - D_i$ is zero at zenith, where elevation bending is null, and it grows to 3.5 cm at 10° above the horizon. It can be interpreted as the difference between D_i (Figure 3.1) and a replica shifted towards the higher apparent elevation angles; e.g., we would have $d_i^g \approx D_i|_{e=5.2^\circ} - D_i|_{e=5^\circ}$ at 5-degree elevation, where elevation bending equals ~ 0.2 degrees. Completing the total delay d_i, we have the along-path interferometric delay component $d_i^a = L_i - R_i$ (13). It is non-zero at zenith, although it does not exceed one centimeter for $H = 10$ m; it can be interpreted as $d_i^a|_{e=90^\circ} \approx 2HN$, where the refractivity is of the order of $N \approx 300 \cdot 10^{-6}$ on average. At slant incidence, this delay component grows seemingly exponentially, reaching 3.5 cm at 10° elevation, like the geometric delay component.

Figure 3.8 (bottom) shows the relative contribution of each of the two components to the total delay budget. At zenith, the along-path atmospheric delay dominates (100%), as the geometric atmospheric delay is zero. Near the horizon, for the height employed in the simulation, surprisingly the two components split the total delay practically in half: 51% and 49% for along-path atmospheric delay and geometric atmospheric delay, respectively.

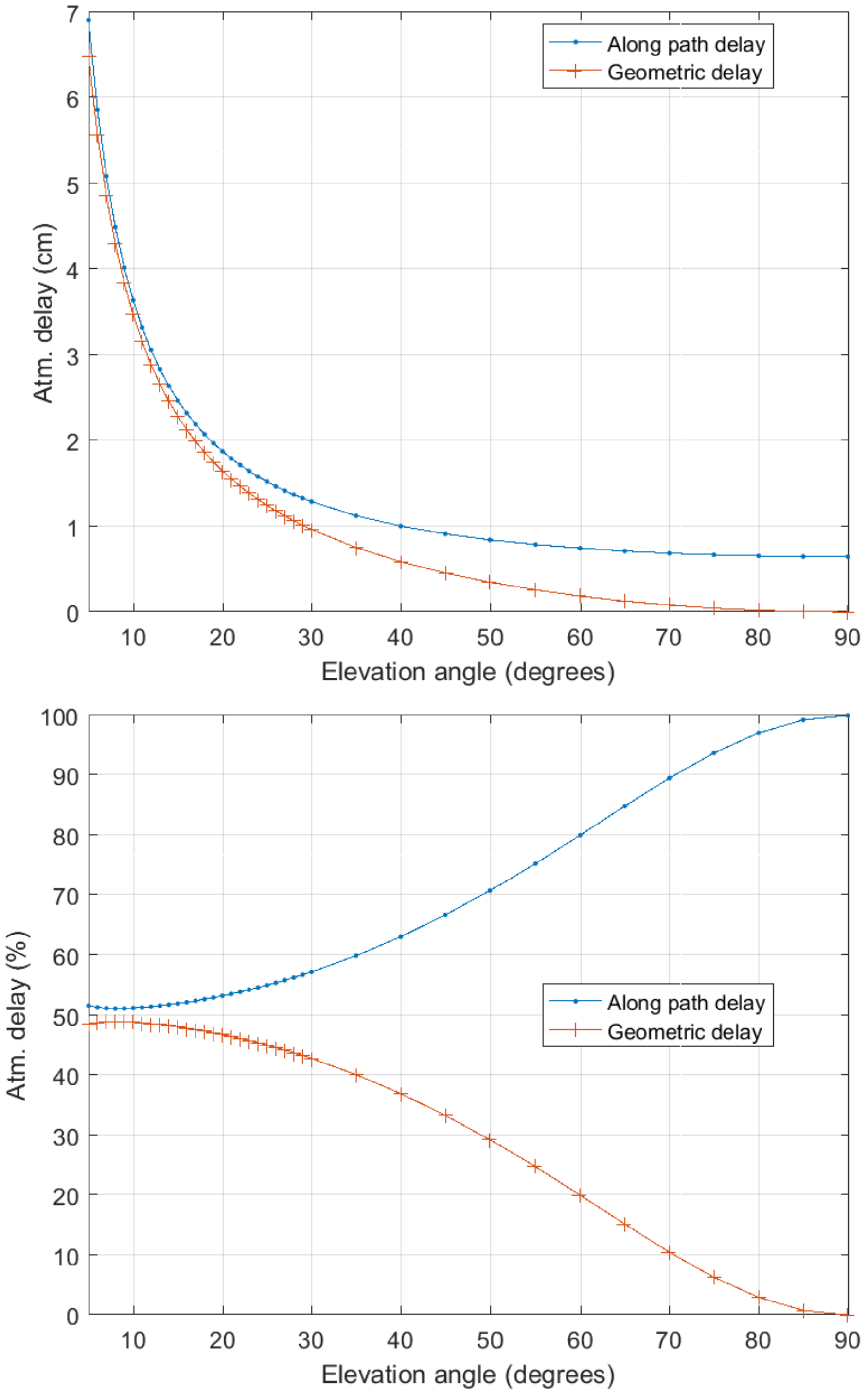

Figure 3.8: Interferometric atmospheric delay components as a function of satellite elevation angle, for a fixed 10-m reflector height (top) ; relative contribution of each component to the total (bottom) .

Now turning to the atmospheric altimetry correction, its components (Figure 3.9) in general follow the delay pattern. The main exception is near zenith, where the geometric atmospheric delay d_i^g goes to zero, yet the corresponding altimetry correction ΔH^g remains non-zero, because it depends on the rate of change of d_i^g w.r.t. sin(e) in eq.(16). There is more similarity between the two components near the horizon, where they again split the total nearly in half: at 10° elevation, there is a crossing in the proportionality, where two components contribute equally.

So, for this particular reflector height ($H = 10$ m), the along-path delay component (Figure 3.8) is consistently larger than the geometric one, for all elevations. This is in contrast to the altimetry correction (Figure 3.9), whose along-path atmospheric component ΔH^a alternates in the leading place with the geometrical atmospheric altimetry correction ΔH^g. At higher elevation angles the two altimetry correction components split the total in 65% and 35%. In terms of absolute values, ΔH^a ranges from 29 cm to nearly 10 cm and eventually 3 mm at 5°, 10° and 90° elevation angle respectively; ΔH^g, on the other hand, attains a maximum of 26 cm at 5° and a minimum of 1.5 mm at 90°.

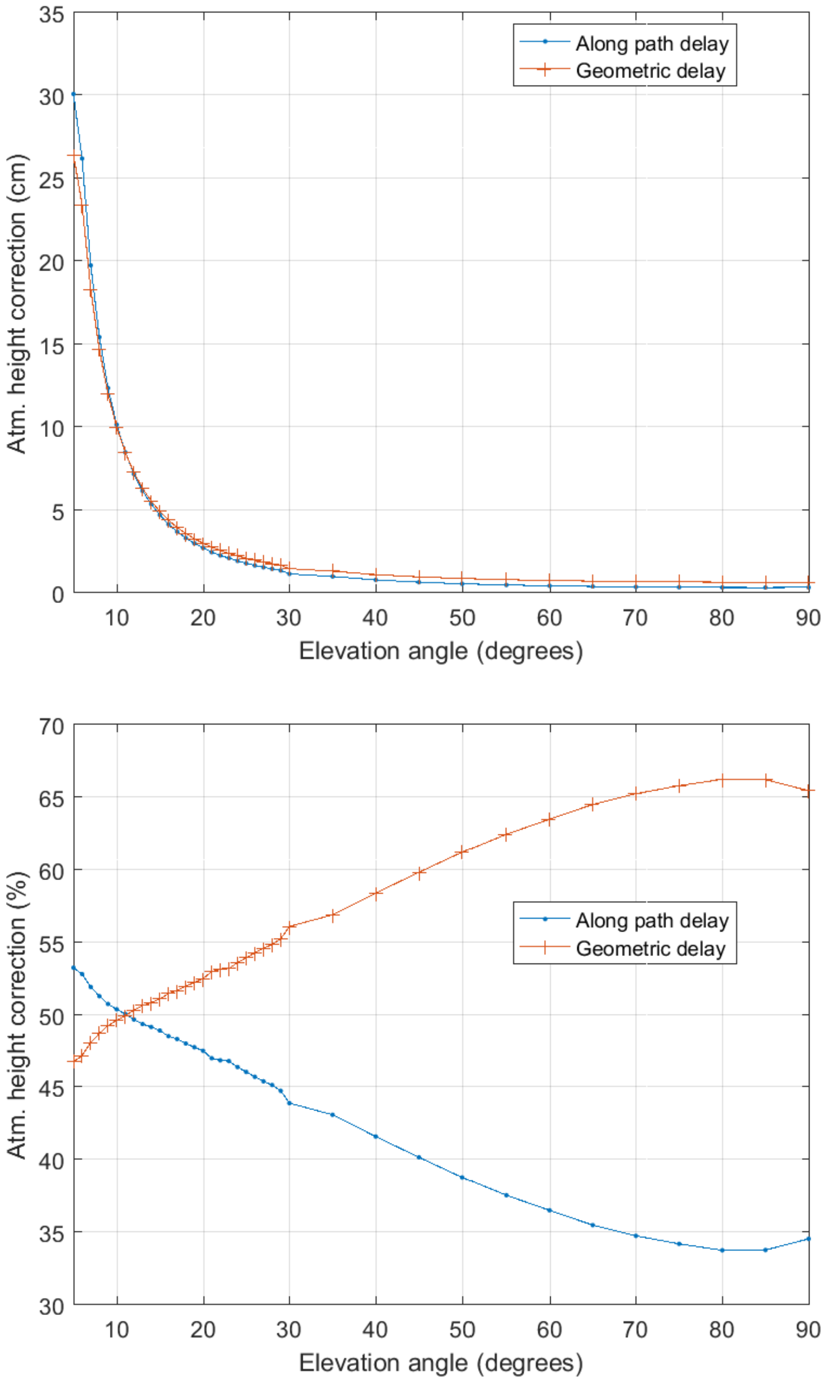

Figure 3.9: Interferometric atmospheric altimetry correction components as a function of satellite elevation angle, for a fixed 10-m reflector height (top) ; relative contribution of each component to the total (bottom) .

As for the subcomponents of the geometric atmospheric delay, shown in Figure 3.10, the geometric-excess component is found to have a negligible effect on the total geometric delay (< 1% of the total geometric delay). At 5-degree elevation the geometric-shift delay component is almost 6.5 cm which translates to an altimetry correction of almost 26 cm (Figure 3.9). The respective geometric-excess altimetry correction is less than 0.5 cm.

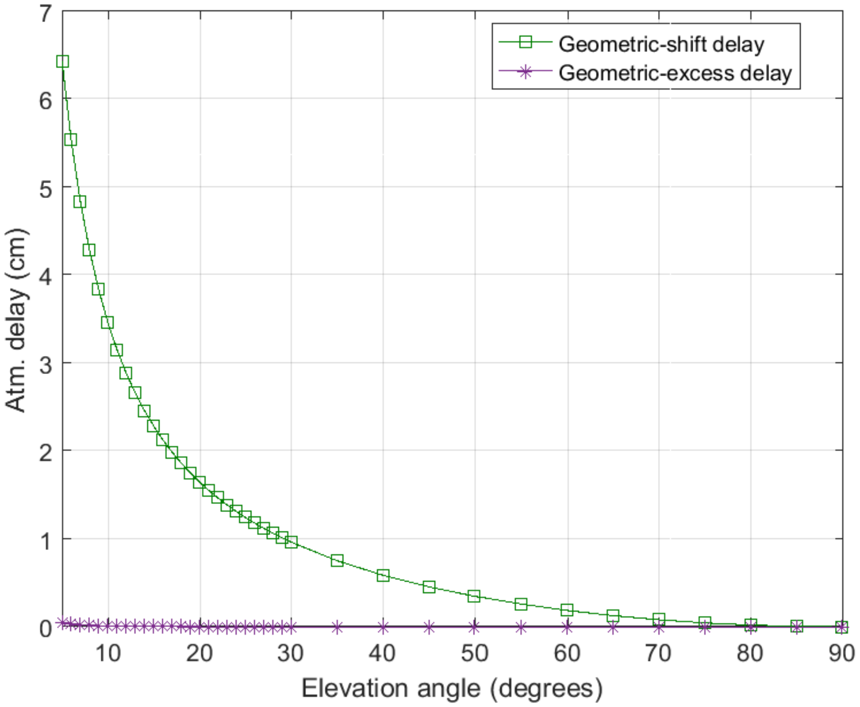

Figure 3.10: Subcomponents of interferometric atmospheric geometric delay components as a function of satellite elevation angle, for a fixed 10-m reflector height.

3.5. Conclusions

Several studies have recognized the importance of atmospheric effects in GNSS-R as it causes systematic biases in altimetry retrievals. In this contribution, we offered a comprehensive study of the atmospheric error in ground-based GNSS-R, including the unification of its linear and angular components.

We defined the total interferometric atmospheric delay based on the vacuum distance and the radio length for each direct and reflected rays. This total was later decomposed in its along-path and geometric components with the introduction of the so-called curve range. We have introduced for the first time two subcomponents of the atmospheric delay, the geometry shift and geometric excess. The definition of an atmospheric altimetry correction concluded the theoretical framework.

We described how atmospheric raytracing, normally employed for line-of-sight directions, can be modified to obtain rigorous results for reflections, including some issues related to the interplay between linear and angular refraction. A procedure was implemented to solve the reflection three-point boundary value problem, involving the broadcasting satellite, reflecting surface, and receiving antenna.

Then, we presented simulation results and performed a thorough analysis of the atmospheric effects in GNSS-R. We showed that interferometric atmospheric delay decreases exponentially with satellite elevation angle and increases linearly with reflector height. The corresponding atmospheric altimetry correction exhibited similar trends, albeit with amplified magnitude: meter level instead of centimeters for a 10-m reflector height.

Subsequently, we examined simulations of the components that make up the interferometric atmospheric delay and altimetry correction. For a 10-m reflector height, the along-path delay is always greater than the geometric atmospheric delay. At low elevation angles the two components split the total in half, while at high elevation angles the geometric one converges to zero at zenith. As for the atmospheric altimetry correction, its geometric component converges to a non-zero value at zenith, as a consequence of its rate-of-change with respect to elevation angle.

We recommend as future work applying the formulation above for modeling the geographical and temporal variations of interferometric atmospheric delay. Due consideration for humidity, preferably using a high-resolution numerical weather model instead of a climatology as done here, is also suggested.

References

Anderson KD (2000) Determination of Water Level and Tides Using Interferometric Observations of GPS Signals. J Atmos Ocean Technol 17:1118–1127. doi: 10.1175/1520-0426(2000)017<1118:DOWLAT>2.0.CO;2

Boehm J, Schuh H, Alizadeh MM, et al (2013) Atmospheric Effects in Space Geodesy. Springer Atmospheric Sciences, Springer Heidelberg New York Dordrecht London

Boniface K, Aparicio JM, Cardellach E (2011) Meteorological information in GPS-RO reflected signals. Atmos Meas Tech 4:1397–1407. doi: 10.5194/amt-4-1397-2011

Born M, Wolf E (1999) Principles of optics Electromagnetic theory of propagation, interference and diffraction of light, 7th expand. Cambridge University Press

Chandra S, Fleming EL, Schoeberl MR, Barnett JJ (1990) Monthly mean global climatology of temperature, wind, geopotential height and pressure for 0-120 km. Adv Sp Res 10:3–12. doi: 10.1016/0273-1177(90)90230-W

Espelid TO (2007) Algorithm 868. ACM Trans Math Softw 33:21-es. doi: 10.1145/1268769.1268775

Fabra F, Cardellach E, Rius A, et al (2012) Phase altimetry with dual polarization GNSS-R over sea ice. IEEE Trans Geosci Remote Sens 50:2112–2121. doi: 10.1109/TGRS.2011.2172797

Fleming EL, Chandra S, Barnett JJ, Corney M (1990) Zonal mean temperature, pressure, zonal wind and geopotential height as functions of latitude. Adv Sp Res 10:11–59. doi: 10.1016/0273-1177(90)90386-E

Geremia-Nievinski F, Hobiger T, Haas R, et al (2020) SNR-based GNSS reflectometry for coastal sea-level altimetry – Results from the first IAG inter-comparison campaign. J Geod 94:70. doi: 10.1007/s00190-020-01387-3

Ifadis IM (2000) A new approach to mapping the atmospheric effect for GPS observations. Earth, Planets Sp 52:703–708. doi: 10.1186/BF03352268

Larson KM (2016) GPS interferometric reflectometry: applications to surface soil moisture, snow depth, and vegetation water content in the western United States. Wiley Interdiscip Rev Water 3:775–787. doi: 10.1002/wat2.1167

Larson KM, Ray RD, Nievinski FG, Freymueller JT (2013) The Accidental Tide Gauge: A GPS Reflection Case Study From Kachemak Bay, Alaska. 10:1200–1204. doi: 10.1109/LGRS.2012.2236075

Larson KM, Ray RD, Williams SDP, et al (2017) A 10-Year Comparison of Water Levels Measured with a Geodetic GPS Receiver versus a Conventional Tide Gauge. J Atmos Ocean Technol 34:295–307. doi: 10.1175/JTECH-D-16-0101.1

Nafisi V, Urquhart L, Santos MC, et al (2012) Comparison of Ray-Tracing Packages for Troposphere Delays. IEEE Trans Geosci Remote Sens 50:469–481. doi: 10.1109/TGRS.2011.2160952

Nievinski FG, Larson KM (2014a) Forward modeling of GPS multipath for near-surface reflectometry and positioning applications. GPS Solut 18:309–322. doi: 10.1007/s10291-013-0331-y

Nievinski FG, Larson KM (2014b) An open source GPS multipath simulator in Matlab/Octave. GPS Solut 18:473–481. doi: 10.1007/s10291-014-0370-z

Nievinski FG, Santos MC (2010) Ray-tracing options to mitigate the neutral atmosphere delay in GPS. Geomatica 64:191–207

Roussel N, Frappart F, Ramillien G, et al (2014) Simulations of direct and reflected wave trajectories for ground-based GNSS-R experiments. Geosci Model Dev 7:2261–2279. doi: 10.5194/gmd-7-2261-2014

Rüeger JM (2002) JS28 Integration of Techniques and Corrections to Achieve Accurate Engineering Refractive Index Formulae for Radio Waves Refractive Index Formulae for Radio Waves. Proc FIG

XXII Int Congr Washington, D C 1–13

Santamaría-Gómez A, Watson C (2017) Remote leveling of tide gauges using GNSS reflectometry: case study at Spring Bay, Australia. GPS Solut 21:451–459. doi: 10.1007/s10291-016-0537-x

Santamaría-Gómez A, Watson C, Gravelle M, et al (2015) Levelling co-located GNSS and tide gauge stations using GNSS reflectometry. J Geod 89:241–258. doi: 10.1007/s00190-014-0784-y

Semmling AM, Schmidt T, Wickert J, et al (2012) On the retrieval of the specular reflection in GNSS carrier observations for ocean altimetry. Radio Sci 47:. doi: 10.1029/2012RS005007

Treuhaft RN, Lowe ST, Zuffada C, Chao Y (2001) 2-cm GPS altimetry over Crater Lake. Geophys Res Lett 28:4343–4346. doi: 10.1029/2001GL013815

Williams SDP, Nievinski FG (2017) Tropospheric delays in ground-based GNSS multipath reflectometry-Experimental evidence from coastal sites. J Geophys Res Solid Earth 122:2310–2327. doi: 10.1002/2016JB013612

Yan H, Wang G (1999) New consideration of atmospheric refraction in laser ranging data. Mon Not R Astron Soc 307:605–610. doi: 10.1046/j.1365-8711.1999.02618.x

Zavorotny VU, Gleason S, Cardellach E, Camps A (2014) Tutorial on remote sensing using GNSS bistatic radar of opportunity. IEEE Geosci Remote Sens Mag 2:8–45. doi: 10.1109/MGRS.2014.2374220

4. A simplification of rigorous atmospheric raytracing based on judicious rectilinear paths for near-surface GNSS reflectometry

Abstract[8]: Atmospheric delays are known to cause biases in Global Navigation Satellite System Reflectometry (GNSS-R) altimetry applications, such as for sea-level monitoring. The main quantity of interest is the reflection-minus-direct or interferometric atmospheric delay. Recently we have presented a rigorous raytracing procedure to account for linear and angular refraction in conjunction with reflection as observed from near-surface platforms. Here we demonstrate the feasibility of simplifying the ray trajectory by imposing a rectilinear wave propagation model. Two variants were assessed, based on the apparent or refracted satellite direction on the one hand and the geometric or vacuum conditions on the other hand. The former was shown to agree with rigorous results in terms of interferometric radio length while the latter agreed in terms of the interferometric vacuum distance. Upon a judicious combination of the best aspects of the two rectilinear cases, we have defined a mixed variant with excellent agreement with rigorous raytracing in terms of interferometric atmospheric delay. We further showed that mapping functions developed for GNSS positioning cannot be reused for GNSS-R purposes without adaptations. Otherwise, the total atmospheric delay may be underestimated by up to 50% at low elevation angles. The present work facilitates the adaptation of existing atmospheric raytracing software for GNSS-R purposes.

---

[8] This chapter is based on the manuscript published in the journal Earth, Planets and Space: Nikolaidou, T., Santos, M. C., Williams, S. D. P., & Geremia-Nievinski, F., (2020). A simplification of rigorous atmospheric raytracing based on judicious rectilinear paths for near-surface GNSS reflectometry. Earth, Planets and Space, 14. doi.org/10.1186/s40623-020-01206-1)

4.1. Introduction

Global Navigation Satellite System Reflectometry (GNSS-R) (E. Cardellach et al., 2011; Jin, Cardellach, & Xie, 2014a; Zavorotny et al., 2014) has been widely demonstrated for long-term ground-based coastal sea level altimetry (Larson et al. 2013; Larson et al. 2017). Atmospheric refraction is known to cause a propagation delay which produces a bias in GNSS-R altimetry, depending on the satellite elevation angle and the reflector height. Almost all assessments of GNSS-R against co-located tide gauges ignore a constant offset between the two sensors, except for example Santamaría-Gómez et al. (2015); this in part due to the lack of levelling (surveying) across the two locations but also due to the atmospheric bias. Unfortunately, this limitation undermines one of the promoted advantages of GNSS-R altimetry, of providing geocentric sea level measurement. Besides a constant offset (average error), systematic atmospheric refraction errors found in sea level retrievals versus satellite elevation angle (Williams & Nievinski, 2017) also affect the precision of retrievals when forming a site-wide average sea level across all visible satellites.

Under multipath reception conditions, direct and reflected radio waves are separated by the interferometric propagation delay $\tau_i = \tau_r - \tau_d$ (Nievinski & Larson, 2014a). Under the hypothesis of a large flat and horizontal reflector surface in vacuum, and ignoring other effects, the interferometric propagation delay can be expressed as $\tau_i = 2H \sin e$ where e is the satellite elevation angle and H is the reflector height, i.e., the vertical distance between the receiver and the reflecting surface. It is the interferometric atmospheric delay which needs to be removed in GNSS-R for determining unbiased reflector height.

Atmospheric refraction manifests in both speed retardation and direction bending along the propagating ray (Nilsson et al., 2013). Its linear and angular components are combined, resulting in the atmospheric propagation delay, which affects GNSS observables such as signal-to-noise ratio (SNR), pseudo-range and carrier phase. In altimetry, the atmospheric delay may be understood as it were causing a mirage effect, in which the reflecting surface appears to be higher than where it actually is.

Several studies have recognized the importance of atmospheric refraction errors in GNSS-R altimetric retrievals (Anderson 2000; Treuhaft et al. 2001; Fabra et al. 2012; Semmling et al. 2012; Roussel et al. 2014; Santamaría-Gómez and Watson 2017; Williams and Nievinski 2017). To address the issue, some authors have suggested the adoption of mapping functions used in GNSS positioning, developed for line-of-sight or direct propagation from satellites (Nafisi et al., 2012) with minimal adaptation for GNSS-R applications. For example, Cardellach et al. (2011) states that "…*the delays induced by the tropospheric layer above the receiving platform cancel out, and only those due to the bottom layer, between the surface and the receiver, affect the altimetric range*…" In line with this concept of a vertically partitioned atmosphere, Zavorotny et al. (2014) states that "*Only the effect coming from the troposphere below the receiver needs to be corrected.*" A similar assumption is held in Treuhaft et al. (2001), who defined the zenith delay difference (across surface and antenna altitudes) and multiplied it by a direct mapping function.

However, models for direct propagation as used in GNSS positioning may adequately capture only the effect of linear refraction, i.e., that of speed retardation. This is because the angular refraction experienced by incoming rays in the upper atmospheric layer (i.e., in the portion above the antenna) does not necessarily cancel out when forming the interferometric atmospheric delay, even for near-surface configurations (Santamaría-Gómez and Watson, 2017). The incoming reflection ray deviates from a straight line as a function of the gradient of refractivity along its entire path; it is thus a cumulative effect, not restricted to the lower portion of the atmosphere, i.e., between the receiver and the reflecting surface. As the incident ray arrives along the apparent satellite elevation angle, and abiding to Snell's law, the refracted reflection point will be shifted compared to unrefracted atmospheric conditions. As the baseline or reference condition for comparison is that of propagation in vacuum, angular refraction thus causes an additional atmospheric delay of geometric nature (Santamaría-Gómez and Watson, 2017).

In Nikolaidou et al. (2020) we have unified the linear and angular components of interferometric atmospheric delay experienced in GNSS-R, demonstrating how they can be derived from first principles. We have also explained the twofold effect of ray bending, introducing sub-components of the atmospheric geometric delay to express the shifitng of the reflection point as well as the deviation of the ray from a straight line. In that work, we have analyzed the bent wave propagation in ground-based GNSS-R altimetry applications. We used a rigorous raytracing approach (RI) in which the Eikonal equation was solved for determining the ray trajectory. Results were of high fidelity but somewhat opaque about the refraction effects involved.

Here we demonstrate a simplified raytracing approach to determine the interferometric atmospheric delay. We show that the large-scale atmospheric geometric delay can be well captured by a judicious choice of rectilinear raypaths. We then assess, for varying satellite elevation and receiver height, under what observation conditions small-scale atmospheric geometric delay is negligible. We justify the simplified rectilinear modeling because it was a common approximation in previous GNSS studies, such as in water-vapor GNSS tomography (Bender et al., 2011; Rohm & Bosy, 2009). It was also very common in early modelling efforts of atmosphere effects in radio propagation (Hopfield, 1969; Saastamoinen, 1972).

In section 2 we describe the numerical procedure while in section 3 we lay down a model for the interaction between the various quantities. An alternative formulation is also presented in section 3, based on the atmospheric layer between receiving antenna and reflecting surface. Numerical assessment results are shown and discussed in section 4, while section 5 concludes the paper with a summary of the main findings.

4.2. Interferometric Raytracing

Figure 4.1 depicts the setup involved in a refracted reflection as observed from a near-surface receiver. The main position vectors refer to: an arbitrary ray position, $\boldsymbol{r}$; transmitting satellite, $\boldsymbol{r}_{\mathrm{sat}}$; receiving antenna, $\boldsymbol{r}_{\mathrm{ant}}$; vacuum surface reflection point, $\boldsymbol{r}_{\mathrm{sfc}}$; and refracted reflection point, $\boldsymbol{r}'_{\mathrm{sfc}}$. Viewing directions are denoted as unit vectors such as $\Delta\hat{\boldsymbol{r}}_{\mathrm{sat}}$ and $\Delta\hat{\boldsymbol{r}}'_{\mathrm{sat}}$ for geometric (vacuum) and apparent (refracted) conditions, respectively.

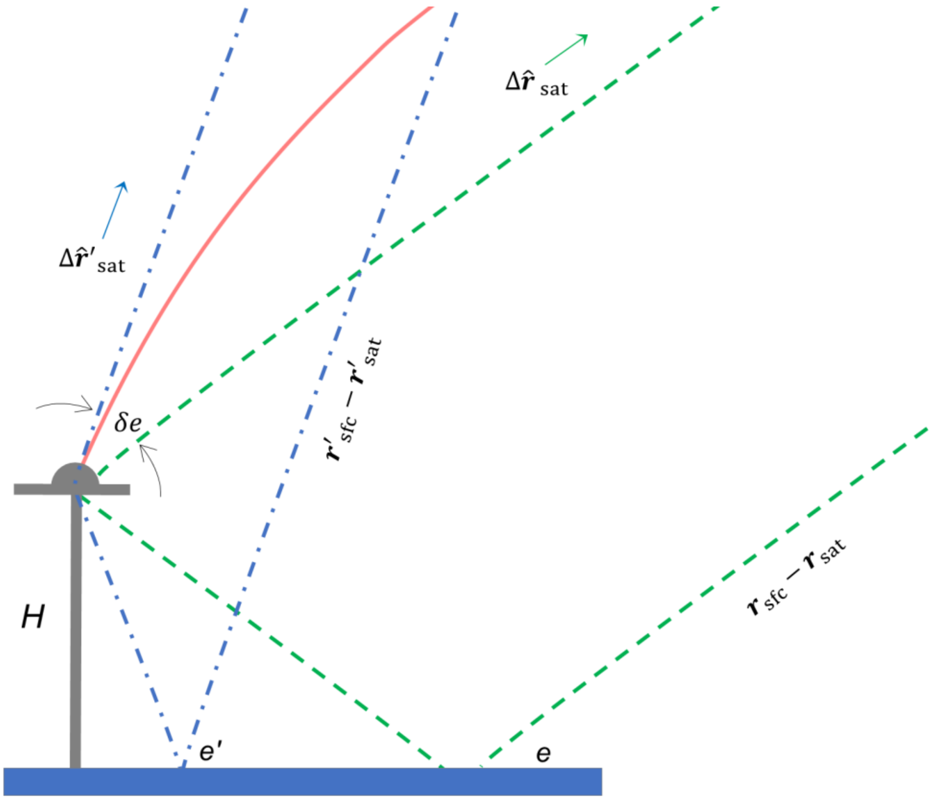

Figure 4.1: Geometry of the two rectilinear approaches: rectilinear-geometric (green dashed line) and rectilinear-apparent (blue dash-dot line).

4.2.1. Rigorous Raytracing

A rigorous interferometric raytracing procedure has been developed in a previous study (Nikolaidou et al. 2020), where we gave a detailed description of both the direct and reflection raytracing. The background can be summarized as follows.

We assume a spherical atmosphere, where the spatial gradient of the index of refraction ($\boldsymbol{\nabla} n$) points to the center of the sphere and the raypath is a plane curve, i.e., there is no out-of-plane bending:

$$\hat{\boldsymbol{\nabla}} n = \frac{\boldsymbol{\nabla} n}{\|\boldsymbol{\nabla} n\|} = -\hat{\boldsymbol{r}}' = -\frac{\boldsymbol{r}'}{\|\boldsymbol{r}'\|} \qquad (1)$$

where $\boldsymbol{r}' = \boldsymbol{r} - \boldsymbol{r}_o$ is a ray vector position with respect to the center of the sphere; the sphere is said to osculate the Earth's ellipsoid, i.e., its center $\boldsymbol{r}_o$ lies along the ellipsoidal normal and has radius equal to the ellipsoidal Gaussian radius of curvature (Nievinski and Santos, 2010).

The evolution of the ray is defined by solving the Eikonal equation (Born & Wolf, 1999):

$$\frac{\partial}{\partial l}\left(n\frac{\partial \boldsymbol{r}}{\partial l}\right) = \boldsymbol{\nabla} n \tag{2}$$

with n the (scalar) field of index of refraction and l the incremental raypath arc length. On the one hand, linear refraction will slow down the radio wave (via the atmospheric speed of propagation $v = c/n$, where c is the vacuum speed of light). On the other hand, angular refraction will change the direction of propagation, via the gradient of refraction $\boldsymbol{\nabla} n$ (Nievinski & Santos, 2009).

In order to solve eq.(2), a set of conditions needs to be specified. Often the time is reversed so that raytracing starts at the receiving antenna and ends near the transmitting satellite. A common set of conditions is made of an initial position and an initial direction – the receiver position and the satellite apparent direction; in this case, the final position (the satellite position) is determined as a consequence of the raytracing procedure. Another common choice of boundary conditions is made of initial and final positions (receiver and satellite positions); in this case, the initial or apparent direction follows from raytracing. We start by raytracing the direct ray followed by the reflection. The latter is performed separately for each of the incident and scattered legs (incoming and outgoing segments), which split the whole reflection ray at the specular point. For more details, the reader is referred to Nikolaidou et al. (2020).

4.2.2. Rectilinear Raytracing

We simplified the rigorous bent raypath, based on the Eikonal equation, by postulating rectilinear radio propagation:

$$\boldsymbol{r} = \check{\boldsymbol{r}} + s \cdot \hat{\boldsymbol{t}} \tag{3}$$

So, rays are artificially set to coincide with straight line segments, where $\check{\boldsymbol{r}}$ is the initial ray position, $\hat{\boldsymbol{t}}$ is the ray tangent direction (constant unit vector), and s is the incremental ray distance.

Under this simplified model, the solution of initial- and boundary-value problems is no longer necessary, as the ray trajectory is completely known in advance. We denote the infinitesimal straight-line distance as ds, e.g., $\|\boldsymbol{r}_2 - \boldsymbol{r}_1\| = \int_{\boldsymbol{r}_1}^{\boldsymbol{r}_2} ds$. A numerical quadrature is retained, to integrate the propagation delays d based on refractivity $N \equiv n - 1$: $d = \int N\, ds$. Propagation still occurs in an inhomogeneous atmospheric, model so the ray is subject to linear refraction and, indirectly, may also may be subject to angular refraction, depending on the postulated ray direction, as detailed below.

There are two variants of the rectilinear model. For the *rectilinear geometric* (RG) model, the direct ray is based on the satellite and antenna position in vacuum:

$$\mathrm{RG_d}: \begin{cases} \check{\boldsymbol{r}}_\mathrm{d} & = \boldsymbol{r}_\mathrm{ant} \\ \hat{\boldsymbol{t}}_\mathrm{d} & = \Delta\hat{\boldsymbol{r}}_\mathrm{sat} \end{cases} \tag{4}$$

where the geometric or vacuum satellite relative direction with respect to the antenna is:

$$\begin{gathered} \Delta\hat{\boldsymbol{r}}_\mathrm{sat} = \frac{\Delta\boldsymbol{r}_\mathrm{sat}}{\Delta r_\mathrm{sat}} \\ \Delta r_\mathrm{sat} = \|\Delta\boldsymbol{r}_\mathrm{sat}\| \\ \Delta\boldsymbol{r}_\mathrm{sat} = \boldsymbol{r}_\mathrm{sat} - \boldsymbol{r}_\mathrm{ant} \end{gathered} \tag{5}$$

Continuing with the RG model, the reflection is specified in terms of its incoming and outgoing parts:

$$\mathrm{RG}_{\mathrm{r/inc}}\colon \begin{cases} \check{\boldsymbol{r}}_{\mathrm{r/inc}} = \boldsymbol{r}_{\mathrm{sfc}} \\ \hat{\boldsymbol{t}}_{\mathrm{r/inc}} = \Delta\hat{\boldsymbol{r}}_{\mathrm{sat}} \end{cases} \tag{6}$$

$$\mathrm{RG}_{\mathrm{r/out}}\colon \begin{cases} \check{\boldsymbol{r}}_{\mathrm{r/out}} = \boldsymbol{r}_{\mathrm{sfc}} \\ \hat{\boldsymbol{t}}_{\mathrm{r/out}} = -\Delta\hat{\boldsymbol{r}}_{\mathrm{sfc}} \end{cases} \tag{7}$$

where the geometric or vacuum relative surface direction with respect to the antenna is:

$$\begin{aligned} \Delta\hat{\boldsymbol{r}}_{\mathrm{sfc}} &= \frac{\Delta\boldsymbol{r}_{\mathrm{sfc}}}{\Delta r_{\mathrm{sfc}}} \\ \Delta r_{\mathrm{sfc}} &= \left\|\Delta\boldsymbol{r}_{\mathrm{sfc}}\right\| \\ \Delta\boldsymbol{r}_{\mathrm{sfc}} &= \boldsymbol{r}_{\mathrm{sfc}} - \boldsymbol{r}_{\mathrm{ant}} \end{aligned} \tag{8}$$

The second variant of this simplified ray model is the *rectilinear apparent* (RA) model, for which the direct ray is defined as:

$$\mathrm{RA}_{\mathrm{d}}\colon \begin{cases} \check{\boldsymbol{r}}_{\mathrm{d}} = \boldsymbol{r}_{\mathrm{ant}} \\ \hat{\boldsymbol{t}}_{\mathrm{d}} = \Delta\hat{\boldsymbol{r}}'_{\mathrm{sat}} \end{cases} \tag{9}$$

The antenna position $\boldsymbol{r}_{\mathrm{ant}}$ is unchanged and the apparent or refracted satellite relative direction with respect to the antenna $\Delta\hat{\boldsymbol{r}}'_{\mathrm{sat}}$ is assumed known; in practice, the latter is obtained from a previous rigorous direct-path raytracing (Nikolaidou et al. 2020). The RA reflection is again specified in terms of its incoming and outgoing parts:

$$\mathrm{RA}_{\mathrm{r/inc}}\colon \begin{cases} \check{\boldsymbol{r}}_{\mathrm{r/inc}} = \boldsymbol{r}'_{\mathrm{sfc}} \\ \hat{\boldsymbol{t}}_{\mathrm{r/inc}} = \Delta\hat{\boldsymbol{r}}'_{\mathrm{sat}} \end{cases} \tag{10}$$

$$\mathrm{RA}_{\mathrm{r/out}}\colon \begin{cases} \check{\boldsymbol{r}}_{\mathrm{r/out}} = \boldsymbol{r}'_{\mathrm{sfc}} \\ \hat{\boldsymbol{t}}_{\mathrm{r/out}} = -\Delta\hat{\boldsymbol{r}}'_{\mathrm{sfc}} \end{cases} \tag{11}$$

where the apparent or refracted relative surface position with respect to the antenna, $\Delta\hat{\boldsymbol{r}}'_{\mathrm{sfc}}$ is obtained analogously to $\Delta\hat{\boldsymbol{r}}'_{\mathrm{sat}}$. Where necessary, we establish a fictitious *apparent satellite position* as

$$\boldsymbol{r}'_{\mathrm{sat}} = \boldsymbol{r}_{\mathrm{ant}} + D_d \cdot \Delta\hat{\boldsymbol{r}}'_{\mathrm{sat}} \tag{12}$$

lying along a given apparent satellite direction $\Delta\hat{\boldsymbol{r}}'_{\mathrm{sat}}$ at a direct distance $D_d = \left\|\Delta\hat{\boldsymbol{r}}_{\mathrm{sat}}\right\|$ which is the same as in vacuum, for convenience. Given these specifications of rectilinear initial and boundary conditions, raytracing proceeds as before.

4.3. Atmospheric Delay Modeling

Now we describe how to model the interferometric atmospheric delay given the output of the raytracing procedure laid above.

4.3.1. Rigorous Delay Formulation

Error! Reference source not found. summarizes the definitions of the intrinsic radio propagation quantities between any two points: vacuum distance: $D = \|\boldsymbol{r}_1 - \boldsymbol{r}_2\|$; radio length: $L = \int_{\boldsymbol{r}_1}^{\boldsymbol{r}_2} n \, dl$; and curve range: $R = \int_{\boldsymbol{r}_1}^{\boldsymbol{r}_2} 1 \, dl$.

Table 4.2 recapitulates the atmospheric delay and its components: total: $d = L - D = d^a + d^g$; along-path: $d^a = L - R = \int_{r_1}^{r_2} N\, dl$; and geometric atmospheric delay: $d^g = R - D$. For details, the reader is directed to Nikolaidou et al. (2020).

The interferometric quantities yield as the difference of the corresponding reflection and direct quantities, for example: interferometric vacuum distance: $D_i = D_r - D_d$; interferometric radio length: $L_i = L_r - L_d$; and interferometric curve range: $R_i = R_r - R_d$. The interferometric atmospheric delay follows from two equivalent formulations:

$$d_i = d_r - d_d = L_i - D_i \tag{13}$$

This definition is extended to the interferometric delay components, the along-path delay: $d_i^a = L_i - R_i$ and the geometric one: $d_i^g = R_i - D_i$ As before, the two parts make up the total delay, i.e., $d_i = d_i^a + d_i^g$ (Nikolaidou et al. 2020).

Finally, the atmospheric geometric delay can be further decomposed into the geometric-excess and the geometric-shift delays as $d_i^g = d_i^{g'} + d_i^{g''}$. This is possible with the introduction of a shifted vacuum delay D_i':

$$\begin{aligned} d_i^{g'} &= R_i - D_i' \\ d_i^{g''} &= D_i' - D_i \end{aligned} \tag{14}$$

where:

$$\begin{aligned} D_i &= \|\boldsymbol{r}_{\text{ant}} - \boldsymbol{r}_{\text{sfc}}\| + \|\boldsymbol{r}_{\text{sfc}} - \boldsymbol{r}_{\text{sat}}\| - \|\boldsymbol{r}_{\text{ant}} - \boldsymbol{r}_{\text{sat}}\| \\ D_i' &= \|\boldsymbol{r}_{\text{ant}} - \boldsymbol{r}'_{\text{sfc}}\| + \|\boldsymbol{r}'_{\text{sfc}} - \boldsymbol{r}'_{\text{sat}}\| - \|\boldsymbol{r}_{\text{ant}} - \boldsymbol{r}'_{\text{sat}}\| \end{aligned} \tag{15}$$

So, while the ordinary vacuum delay D_i involves the vacuum reflection point, the shifted vacuum delay D_i' is obtained freezing the refracted reflection geometry (shifted specular point $\boldsymbol{r}'_{\text{sfc}}$ and apparent satellite direction $\Delta\hat{\boldsymbol{r}}'_{\text{sfc}}$) and undressing the atmosphere (i.e., nullifying the refractivity, $N = 0$).

The atmospheric geometric-shift delay is a consequence of the application of Snell's law at the refracted reflection point. It will maintain its magnitude even for small reflector heights, as it is largely formed by the angular refraction taking place above the receiving antenna. In contrast, the atmospheric geometric-excess delay corresponds to the deviation of the ray paths from straight-line segments. It may be assumed close to zero for sufficiently small reflector heights, as determined below.

Table 4.1: Definition of the propagation quantities

	Vacuum distance	Radio length	Curve range
(generic)	$D = \lVert \boldsymbol{r}_1 - \boldsymbol{r}_2 \rVert$	$L = \int_{\boldsymbol{r}_1}^{\boldsymbol{r}_2} n \, dl$	$R = \int_{\boldsymbol{r}_1}^{\boldsymbol{r}_2} 1 \, dl$
Direct	$D_d = \lVert \boldsymbol{r}_{\text{ant}} - \boldsymbol{r}_{\text{sat}} \rVert$	$L_d = \int_{\boldsymbol{r}_{\text{ant}}}^{\boldsymbol{r}_{\text{sat}}} n \, dl$	$R_d = \int_{\boldsymbol{r}_{\text{ant}}}^{\boldsymbol{r}_{\text{sat}}} 1 \, dl$
Reflection	$D_r = \lVert \boldsymbol{r}_{\text{ant}} - \boldsymbol{r}_{\text{sfc}} \rVert + \lVert \boldsymbol{r}_{\text{sfc}} - \boldsymbol{r}_{\text{sat}} \rVert$	$L_r = \int_{\boldsymbol{r}'_{\text{sfc}}}^{\boldsymbol{r}_{\text{sat}}} n \, dl + \int_{\boldsymbol{r}_{\text{ant}}}^{\boldsymbol{r}'_{\text{sfc}}} n \, dl$	$R_r = \int_{\boldsymbol{r}'_{\text{sfc}}}^{\boldsymbol{r}_{\text{sat}}} 1 \, dl + \int_{\boldsymbol{r}_{\text{ant}}}^{\boldsymbol{r}'_{\text{sfc}}} 1 \, dl$
Interferometric	$D_i = D_r - D_d$	$L_i = L_r - L_d$	$R_i = R_r - R_d$

Table 4.2: Definition of atmospheric delay and its components

	Atmospheric delay	Along-path atmospheric delay	Geometric atmospheric delay
(generic)	$d = L - D$ $d = d^a + d^g$	$d^a = L - R = \int_{r_1}^{r_2} N\,dl$	$d^g = R - D$
Direct	$d_d = L_d - D_d$ $d_d = d_d^a + d_d^g$	$d_d^a = L_d - R_d$	$d_d^g = R_d - D_d$
Reflection	$d_r = L_r - D_r$ $d_r = d_r^a + d_r^g$	$d_r^a = L_r - R_r$	$d_r^g = R_r - D_r$
Interfero-metric	$d_i = L_i - D_i$ $d_i = d_r - d_d$ $d_i = d_i^a + d_i^g$	$d_i^a = L_i - R_i$	$d_i^g = R_i - D_i$ $d_i^g = d_r^g - d_d^g$

4.3.2. Rectilinear Delay Formulation

In Table 4.3, we have adapted the rigorous definitions above (henceforth RI) for the two cases of rectilinear propagation (RG and RA); an overhead bar notation is used for distinction.

The RG vacuum distance equals the ordinary one used in the RI case, $\overline{D} = D$. In the RA approach, though, it equals the shifted vacuum distance, $\overline{D}' = D'$. The RG approach lacks any angular refraction effect and is subject only to linear refraction, albeit on a simplified ray path. The RA approach, on the other hand, includes both types of refraction, although ray bending is accounted in an all-or-nothing manner, only in the incident direction and it is not allowed to vary along the raypath as in the RI case. In both rectilinear cases, the curve range equals the respective vacuum distances, as there is no ray bending:

$$\begin{aligned} \bar{R} &= \bar{D} \\ \bar{R}' &= \bar{D}' \end{aligned} \tag{16}$$

The rectilinear models may seem overly simplistic, but it turns out a judicious combination proved accurate, as demonstrated by results below. We define a *rectilinear-mixed* (RM) model, denoted with double overhead bars. It utilizes the RG vacuum distance in conjunction with the RA radio length and the RA curve range:

$$\begin{aligned} \bar{\bar{D}} &= \bar{D} \\ \bar{\bar{R}} &= \bar{R}' \\ \bar{\bar{L}} &= \bar{L}' \end{aligned} \tag{17}$$

Table 4.3: Definition of rectilinear propagation quantities

	Rectilinear Geometric (RG)		Rectilinear Apparent (RA)	
	Vacuum distance	Radio length	Vacuum distance	Radio length
Direct	$\bar{D}_d = \lVert \boldsymbol{r}_{\text{ant}} - \boldsymbol{r}_{\text{sat}} \rVert$	$\bar{L}_d = \int_{\boldsymbol{r}_{\text{ant}}}^{\boldsymbol{r}_{\text{sat}}} n\, ds$	$\bar{D}'_d = \lVert \boldsymbol{r}_{\text{ant}} - \boldsymbol{r}'_{\text{sat}} \rVert$	$\bar{L}'_d = \int_{\boldsymbol{r}_{\text{ant}}}^{\boldsymbol{r}'_{\text{sat}}} n\, ds$
Reflection	$\bar{D}_r = \lVert \boldsymbol{r}_{\text{ant}} - \boldsymbol{r}_{\text{sfc}} \rVert + \lVert \boldsymbol{r}_{\text{sfc}} - \boldsymbol{r}_{\text{sat}} \rVert$	$\bar{L}_r = \int_{\boldsymbol{r}_{\text{sfc}}}^{\boldsymbol{r}_{\text{sat}}} n\, ds + \int_{\boldsymbol{r}_{\text{ant}}}^{\boldsymbol{r}_{\text{sfc}}} n\, ds$	$\bar{D}'_r = \lVert \boldsymbol{r}_{\text{ant}} - \boldsymbol{r}'_{\text{sfc}} \rVert + \lVert \boldsymbol{r}'_{\text{sfc}} - \boldsymbol{r}'_{\text{sat}} \rVert$	$\bar{L}'_r = \int_{\boldsymbol{r}'_{\text{sfc}}}^{\boldsymbol{r}'_{\text{sat}}} n\, ds + \int_{\boldsymbol{r}_{\text{ant}}}^{\boldsymbol{r}'_{\text{sfc}}} n\, ds$
Interferometric	$\bar{D}_i = \bar{D}_r - \bar{D}_d$	$\bar{L}_i = \bar{L}_r - \bar{L}_d$	$\bar{D}'_i = \bar{D}'_r - \bar{D}'_d$	$\bar{L}'_i = \bar{L}'_r - \bar{L}'_d$

Table 4.4, summarizes the definitions of the various rectilinear interferometric atmospheric delays and their components. Where necessary, the atmospheric altimetry correction follows from half the rate of change of delay with respect to the sine of the elevation angle (Nikolaidou et al. 2020):

$$\Delta\bar{H} = -0.5\, \partial \bar{d}_i / \partial \sin e \tag{18}$$

Table 4.4: Definition of rectilinear interferometric atmospheric delays

	Rectilinear Geometric	Rectilinear Apparent	Rectilinear Mixed
Along-path	$\bar{d}_i^{a} = \bar{L}_i - \bar{R}_i$ $\bar{d}_i^{a} = \bar{L}_i - \bar{D}_i$	$\bar{d}_i^{\prime a} = \bar{L}_i' - \bar{R}_i'$ $\bar{d}_i^{\prime a} = \bar{L}_i' - \bar{D}_i'$	$\bar{\bar{d}}_i^{a} = \bar{\bar{L}}_i - \bar{\bar{R}}_i$ $\bar{\bar{d}}_i^{a} = \bar{L}_i' - \bar{R}_i'$ $\bar{\bar{d}}_i^{a} = \bar{d}_i^{\prime a}$
Geometric	$\bar{d}_i^{g} = \bar{R}_i - \bar{D}_i$ $\bar{d}_i^{g} = 0$	$\bar{d}_i^{\prime g} = \bar{R}_i' - \bar{D}_i'$ $\bar{d}_i^{\prime g} = 0$	$\bar{\bar{d}}_i^{g} = \bar{\bar{R}}_i - \bar{\bar{D}}_i$ $\bar{\bar{d}}_i^{g'} = \bar{R}_i' - \bar{D}_i$ $\bar{\bar{d}}_i^{g''} = \bar{D}_i' - \bar{D}_i$
Total	$\bar{d}_i = \bar{d}_i^{a} + \bar{d}_i^{g}$ $\bar{d}_i = \bar{d}_i^{a}$	$\bar{d}_i' = \bar{d}_i^{\prime a} + \bar{d}_i^{\prime g}$ $\bar{d}_i' = \bar{d}_i^{\prime a}$	$\bar{\bar{d}}_i = \bar{\bar{d}}_i^{a} + \bar{\bar{d}}_i^{g}$

4.4. Results and Discussion

Here we assess results from rectilinear approach against rigorous raytracing. We assess first wave propagation quantities and later the derived atmospheric delays and altimetry corrections.

As atmospheric model source, we employed the COSPAR International Reference Atmosphere 1986 (CIRA-86) climatology (Chandra, Fleming, Schoeberl, & Barnett, 1990; Fleming, Chandra, Barnett, & Corney, 1990); more specifically, file twp.lsn, available for download from https://ccmc.gsfc.nasa.gov/modelweb/atmos/cospar1.html. It provides temperature (0-120 km) and pressure (20-120 km) at 5-km intervals; surface pressure is obtained via hydrostatic integration. Temperature and pressure at any other sampling points is obtained via linear and log-linear interpolation, respectively.

In terms of computational cost, for an elevation angle of 5 degrees and a delay convergence tolerance of 10^{-6} m, the processing time decreases by 67%, from 0.45 s in RI to 0.15 s in RM, i.e., RM takes only one third the time taken by RI.

4.4.1. Propagation Quantities

We start by illustrating in Figure 4.2 the discrepancy in interferometric vacuum distance, D_i. The rectilinear-geometric (RG) result, $\overline{D}_i$, is in near absolute agreement with that of RI. In contrast, rectilinear apparent (RA) result, $\overline{D}_i'$, falls short of D_i by an amount which is a consequence of angular refraction (ray bending angle, $\delta e = e' - e$). At zenith, all interferometric vacuum distances agree to $2H$. Their discrepancy increases at low elevation angles, reaching 6.5 cm at 5° elevation angle for a 10-m reflector height.

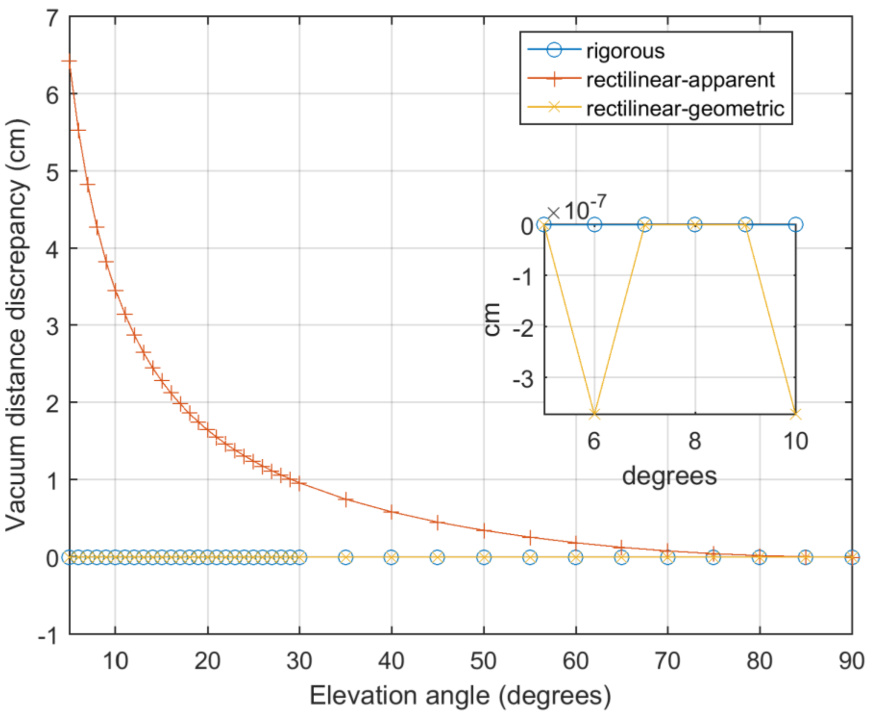

Figure 4.2: Vacuum distance discrepancy as a function of satellite elevation angle (for a fixed 10-m reflector height).

Next, Figure 4.3 shows the discrepancy in interferometric curve range, R_i, among the various approaches. Contrary to the previous comparison, here the RG curve range, $\bar{R}_i$, has a large discrepancy with respect to RI. In this comparison, it is RA that best matches RI, $\bar{R}_i' \approx R_i$, as both are subject to angular refraction on the raypath. So, although the fictitious refracted satellite is very far from the actual satellite position, it is more representative for the calculation of the interferometric curve range. The agreement between RA and RI is not exact because rectilinear propagation neglects path-dependent incremental ray bending, accounting only for the total ray bending. The RA curve range degenerates to the respective (modified) vacuum distance, $\bar{R}_i' = \bar{D}_i'$.

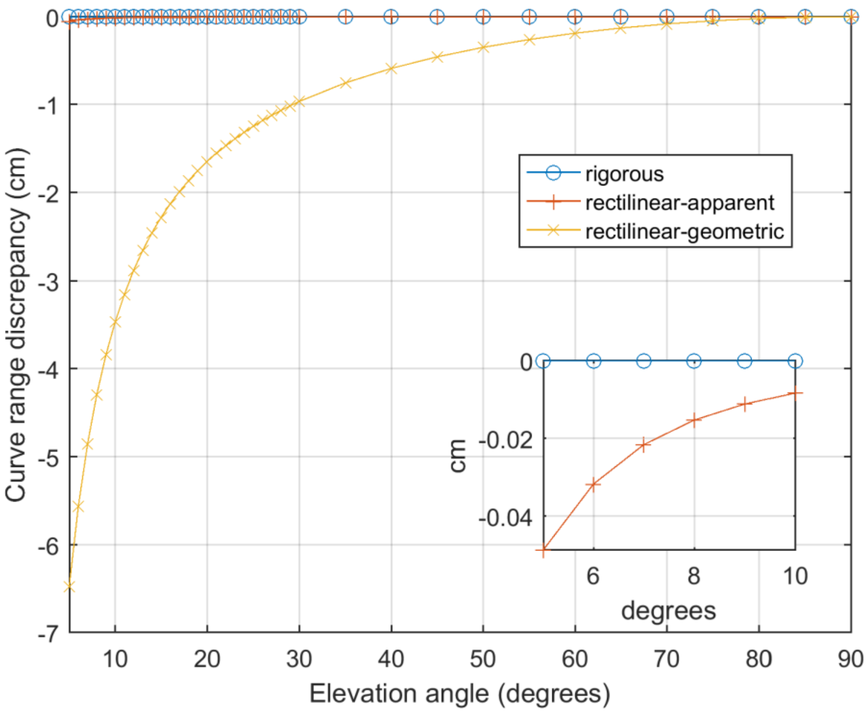

Figure 4.3: Curve range discrepancy as a function of satellite elevation angle (for a fixed 10-m reflector height).

Lastly, the discrepancy in interferometric radio length L_i follows a similar pattern than that of the interferometric curve range (Figure 4.3), with RI agreeing better with RA, $\bar{L}'_i$, than with RG, $\bar{L}_i$. This characteristic will be further analyzed below, in terms of the atmospheric delay.

In summary, RI vacuum distance is best approximated by RG while RI curve range and RI radio length are best approximated by RA. With this we justify the rectilinear-mixed (RM) approach (17), which borrows the best of each rectilinear models: RG $\left(\bar{\bar{D}}_i = \bar{D}_i\right)$ and RA $\left(\bar{\bar{L}}_i = \bar{L}'_i \text{ and } \bar{\bar{R}}_i = \bar{R}'_i\right)$.

4.4.2. Total Atmospheric Delay and Altimetry Correction

In this section we shall assess rectilinear results in terms of atmospheric delay and the resulting atmospheric altimetry correction. Figure 4.4 shows the discrepancy, $\bar{\bar{d}}_i - d_i$, in total interferometric atmospheric delay, between RM ($\bar{\bar{d}}_i = \bar{\bar{L}}_i - \bar{\bar{D}}_i$) and RI ($d_i = L_i - D_i$) approaches. For a 10-m reflector height, the agreement is excellent, having a maximum sub-mm discrepancy near the horizon.

Further, it demonstrates that rigorous results (RI) can be approximated well by a judicious rectilinear propagation scheme (RM). It is remarkable that the effect of ray bending can be accurately represented by a straight line at the appropriate direction in the interferometric case.

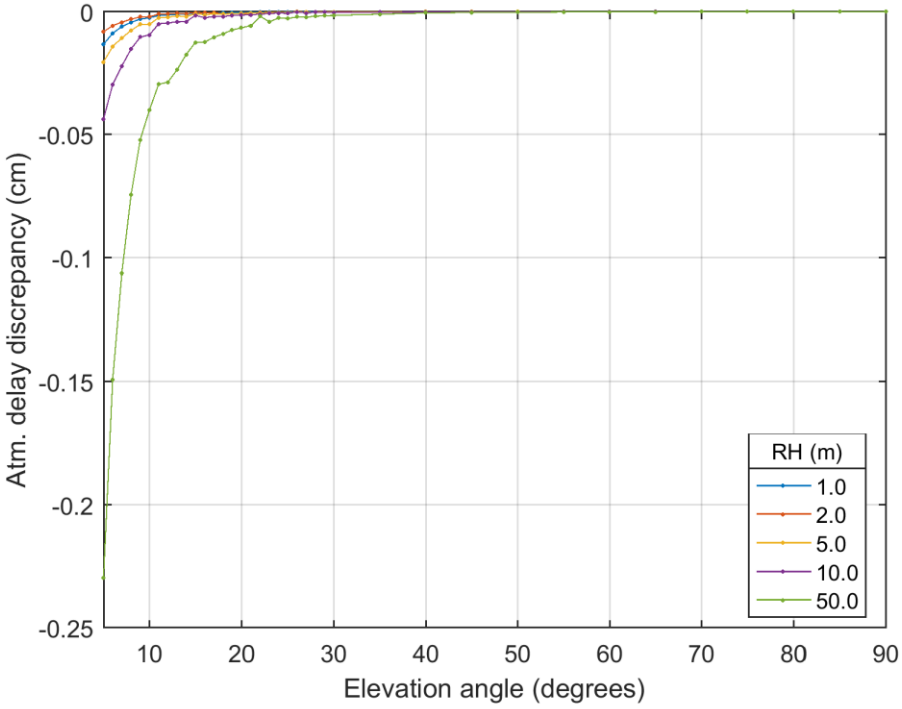

Figure 4.4: Discrepancy in interferometric atmospheric delay between RM and RI formulations as a function of satellite elevation angle (for multiple reflector heights).

The discrepancy in the resulting interferometric atmospheric altimetry correction (Figure 4.5) follows a similar pattern than in the previous result, but scaled approximately by a factor of ten. The maximum discrepancy in atmospheric altimetry is found near the horizon, amounting to 0.4 cm for a 10-m reflector height. Both figures illustrate the proportional increase in the discrepancy with reflector height.

For a reflector height of 20 m, the RM-RI agreement is better than 1 cm in altimetry correction for any elevation above 5 degrees; so the 20-m antenna height may be adopted as a threshold of validity for the assumption of near-surface conditions for the rectilinear model.

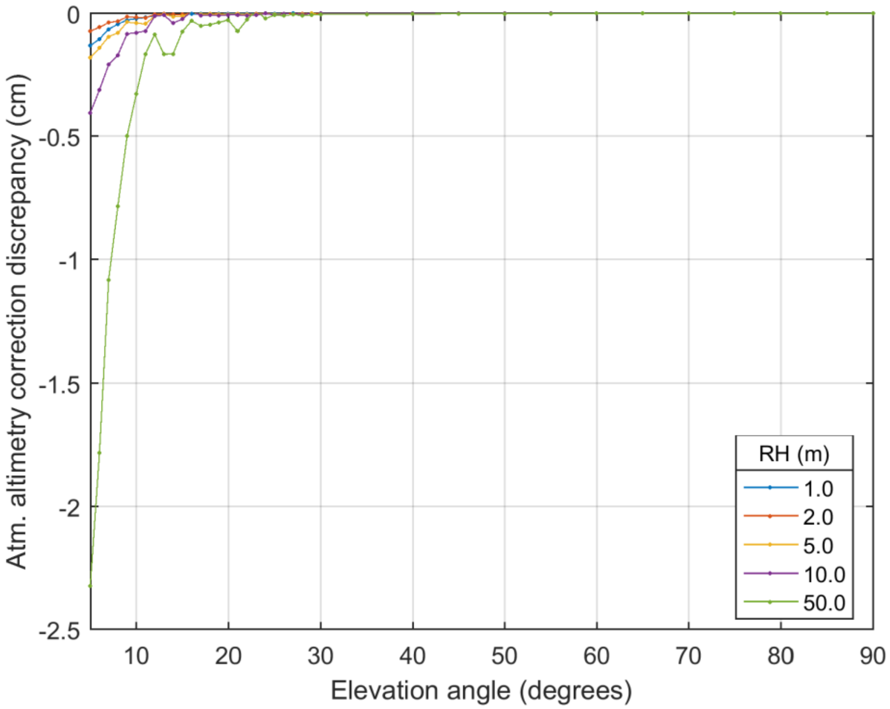

Figure 4.5: Discrepancy in interferometric atmospheric altimetry correction between RM and RI formulations as a function of satellite elevation angle (for multiple reflector heights).

4.4.3. Atmospheric Delay Components

Figure 4.6 compares interferometric geometric atmospheric delay, across RI $\left(d_i^g = R_i - D_i\right)$ and RM $\left(\bar{\bar{d}}_i^g = \bar{\bar{R}}_i - \bar{\bar{D}}_i\right)$ approaches. The discrepancy $\bar{\bar{d}}_i^g - d_i^g$ converges to zero at zenith, where elevation bending is null, and it grows to at most 1 mm towards the horizon for a 10-m reflector height. Figure 4.4 demonstrates that the bulk of angular refraction is well captured by the atmospheric geometric-shift delay, the difference between RA and RG interferometric vacuum distances, $\bar{\bar{d}}_i^{g''} = \bar{D}_i' - \bar{D}_i$. The present RM-RI discrepancy in geometric delay is dominated by the atmospheric geometric-excess delay, which also equals the RA-RI discrepancy in curve ranges: $\bar{\bar{d}}_i^g - d_i^g = \bar{\bar{d}}_i^{g'} - d_i^{g'} = \bar{R}_i' - R_i$. Thus, it follows from the incremental elevation bending present in rigorous raytracing but absent in the rectilinear approaches.

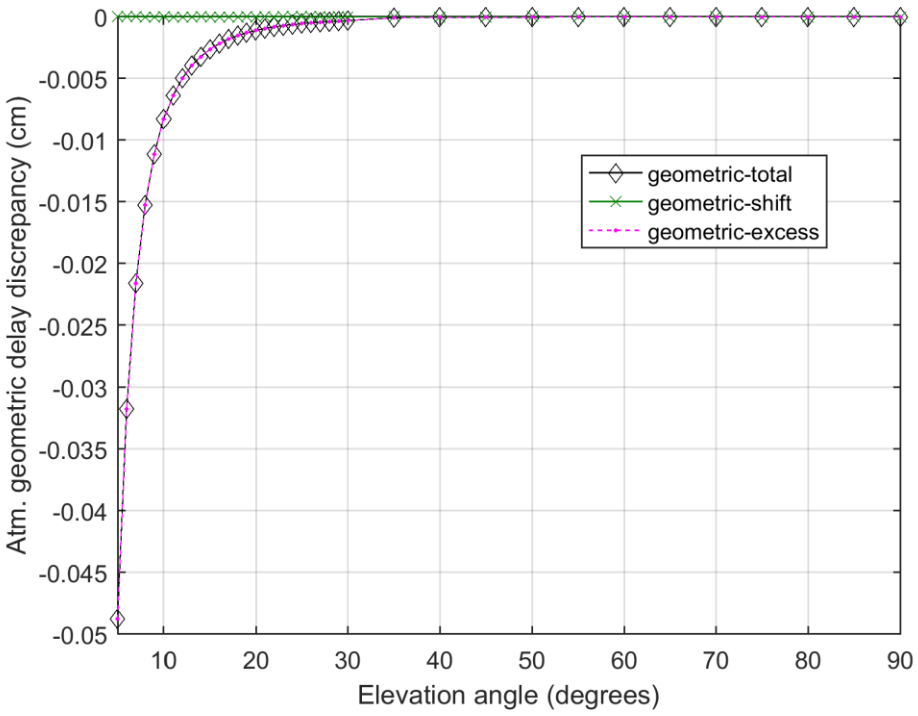

Figure 4.6: Discrepancy in interferometric atmospheric geometric delay between RM and RI formulations as a function of satellite elevation angle (for a fixed 10-m reflector height).

Figure 4.7 shows the discrepancy, $\bar{\bar{d}}_i^a - d_i^a$, in interferometric along-path atmospheric delay, across RI $(d_i^a = L_i - R_i)$ and RM $\left(\bar{\bar{d}}_i^a = \bar{\bar{L}}_i - \bar{\bar{R}}_i\right)$ cases. The agreement is even better (at 50 μm level), with discrepancy values more randomly distributed, resembling numerical noise (likely caused by interpolation in the CIRA atmospheric model).

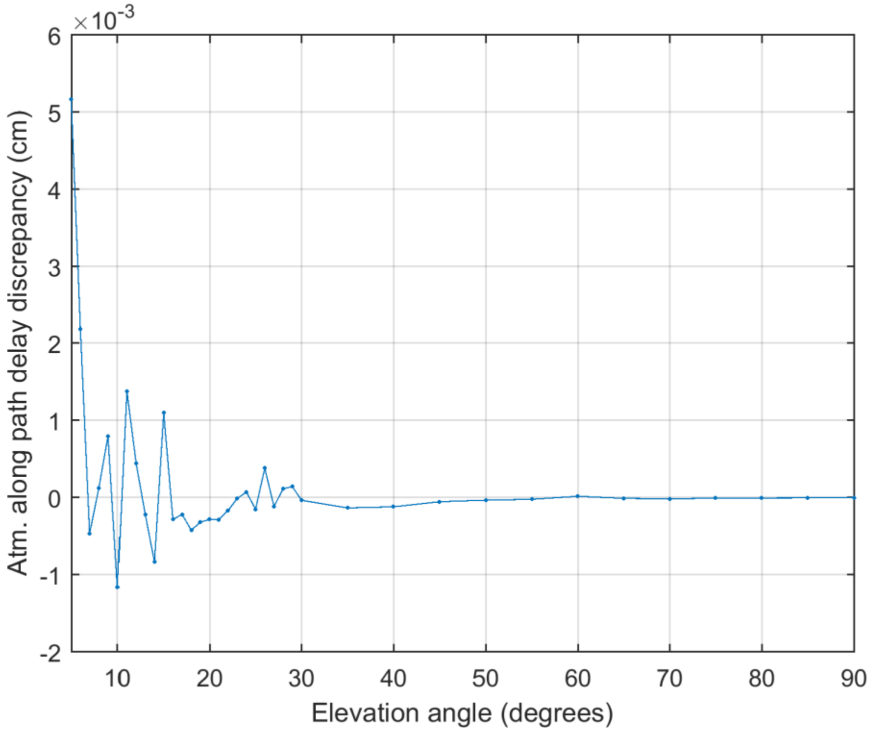

Figure 4.7: Discrepancy in interferometric atmospheric along-path delay between RM and RI formulations as a function of satellite elevation angle (for a fixed 10-m reflector height).

4.4.4. Slant factors

For a better comparison to the standard approach reported in the literature, based on mapping functions, we provide an analysis based on slant factors, $f = d/d^z$, defined as the ratio between slant delay and zenith delay at a particular elevation angle. Slant factors computed from direct raytracing are the input data for developing mapping function models, such as the global mapping function (GMF) (Boehm, Niell, Tregoning, & Schuh, 2006), after fitting to a particular functional expression valid over a given space-time domain (Urquhart et al., 2012).

The direct slant factor is defined as $f_d = d_d/d_d^z$, where the direct zenith delay is that at the antenna: $d_d^z = d_{ant}^z$. The interferometric slant factor, $f_i = d_i/d_i^z$, uses the total interferometric zenith delay, $d_i^z = 2\left(d_{ant}^z - d_{sfc}^z\right)$, which is twice the zenith delay difference across antenna and surface. The slant factors for interferometric components $f_i = f_i{}^a + f_i{}^g$ are computed similarly, as $f_i{}^a = d_i^a / d_i^z$ and $f_i{}^g = d_i^g / d_i^z$ for along-path and geometric terms, respectively.

Figure 4.8 shows the slant factors defined above. They all follow the exponential decay of delay with elevation angle. However, at the lowest elevation angle (5 degrees) the interferometric slant factor measures twice the direct one (20.47 m/m vs. 10.29 m/m). At zenith, where angular refraction is null, they both converge to unity. At low elevation angle, though, using a direct mapping function will underestimate the interferometric delay systematically with decreasing elevation angle by up to 50%.

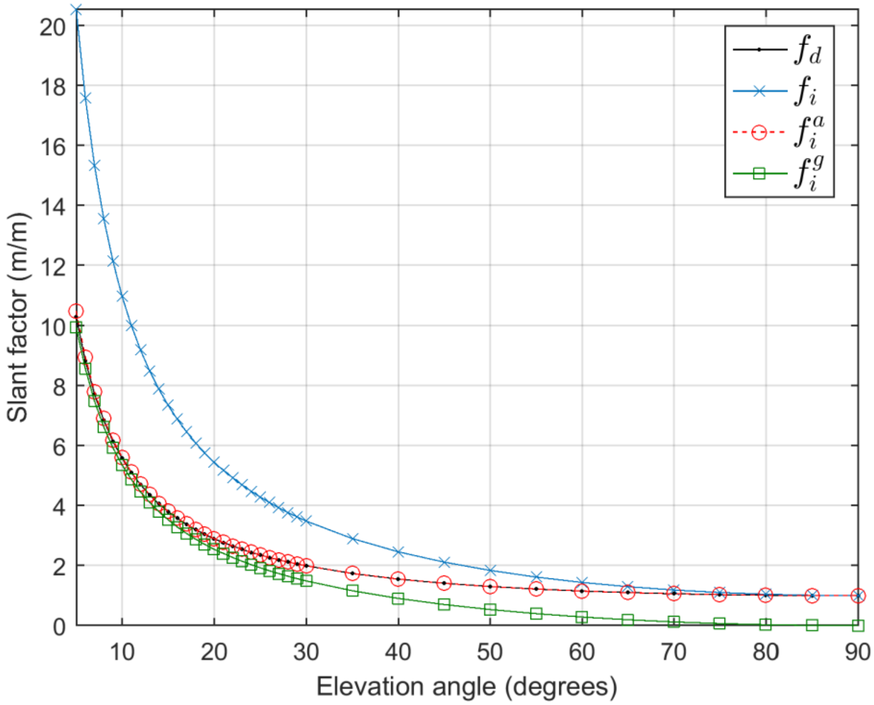

Figure 4.8: Slant factors for the direct and interferometric -total and components- signals as a function of satellite elevation angle (for a fixed 10-m reflector height).

In relation to the components, the interferometric along-path slant factor resembles the direct slant factor, $f_i^a \approx f_d$. They are both related to the thickness of atmospheric layers, albeit different ones: respectively, the inner and outer ones, below and above the antenna. Furthermore, the direct slant factor $f_d = f_d^a + f_d^g$ also involves a weighting of the layer slant distances by refractivity in the integrand of $\int N dl$, as well as a minor contribution from the direct atmospheric geometric delay, f_d^g. The interferometric geometric slant factor f_i^g approaches the along-path one f_i^a at low elevations, e.g., 9.97 m/m vs. 10.51 m/m at 5 degrees elevation angle, but converges to zero at zenith due to the absence of bending.

Finally, it should be emphasized that mapping functions developed for GNSS positioning, such as the GMF, are supposed to agree only with the direct slant factors, as in fact it does: the agreement with our results is within 2% at 5° (not shown). However, correcting for the atmospheric interferometric delay in GNSS-R using GMF or a similar mapping functions will introduce an exponentially increasing bias with elevation angle. The remaining geometric-shift atmospheric delay, which is a result of Snell's law on the refracted specular point, cannot be captured using only the direct or LOS propagation effects, and would require a model for the angular refraction.

4.5. Conclusions

A simplification of the rigorous interferometric raytracing approach (RI) was carried out, imposing a rectilinear ray propagation model for ground-based or near-surface GNSS reflectometry applications. Two initial variants were developed, considering the apparent (refracted) and the geometric (vacuum) satellite directions. The rectilinear-geometric (RG) agreed with the rigorous (RI) for the vacuum distance, while the rectilinear-apparent (RA) agreed with RI for the radio length. Both RG and RA had poor performance in terms of atmospheric delays, though.

Upon combination of the best matching aspect of the two above, RG and RA, we defined a third variant, the rectilinear-mixed (RM) model. It demonstrated excellent agreement in the interferometric atmospheric delay, both in total value and in all components (along-path and geometric). GNSS-R altimetry corrections can, therefore, be predicted by performing a single rigorous raytracing in the direct or line-of-sight direction to determine the ray bending, followed by two rectilinear raytracings in the direct and reflection directions.

The rectilinear models demonstrated for the interferometric atmospheric delay allow for faster and more efficient raytracing, as the reflection three-point boundary value problem (satellite-surface-antenna) can be replaced for an easier two-point problem. Thus, existing raytracing software can be adapted more easily for ground-based GNSS-R applications. The simplifications demonstrated here also pave the way for the future development of more convenient closed-form expressions.

Another key demonstration is that mapping functions developed for GNSS positioning, or even a direct raytracing procedure, cannot be reused for GNSS-R purposes without adaptations. The interferometric atmospheric delay is induced by the atmosphere both above and below the receiver, roughly corresponding to its angular refraction and linear refraction components. At low elevation angles, where the interferometric delay components are similar, direct-only mapping functions will underestimate the total delay by nearly half. In the current study, however, we showed how the interferometric delay and its components can be deduced with a direct-only raytracing procedure by employing a judicious combination of two simpler rectilinear models for the raypath.

References

Anderson, K. D. (2000). Determination of Water Level and Tides Using Interferometric Observations of GPS Signals. *Journal of Atmospheric and Oceanic Technology*, *17*(8), 1118–1127. doi.org/10.1175/1520-0426(2000)017<1118:DOWLAT>2.0.CO;2

Bender, M., Dick, G., Ge, M., Deng, Z., Wickert, J., Kahle, H.-G., … Tetzlaff, G. (2011). Development of a GNSS water vapour tomography system using algebraic reconstruction techniques. *Advances in Space Research*, *47*(10), 1704–1720. doi.org/10.1016/J.ASR.2010.05.034

Boehm, J., Niell, A., Tregoning, P., & Schuh, H. (2006). Global Mapping Function (GMF): A new empirical mapping function based on numerical weather model data. *Geophysical Research Letters*, *33*(L07304). doi.org/10.1029/2005GL025546

Born, M., & Wolf, E. (1999). *Principles of optics Electromagnetic theory of propagation, interference and diffraction of light* (7th expand). Cambridge University Press. doi.org/10.1017/CBO9781139644181

Cardellach, E., Fabra, F., Nogués-Correig, O., Oliveras, S., Ribó, S., & Rius, A. (2011). GNSS-R ground-based and airborne campaigns for ocean, land, ice, and snow techniques: Application to the GOLD-RTR data sets. *Radio Science*, *46*(5), 1–16. doi.org/10.1029/2011RS004683

Chandra, S., Fleming, E. L., Schoeberl, M. R., & Barnett, J. J. (1990). Monthly mean global climatology of temperature, wind, geopotential height and pressure for 0-120 km. *Advances in Space Research*, *10*(6), 3–12. doi.org/10.1016/0273-1177(90)90230-W

Fabra, F., Cardellach, E., Rius, A., Ribó, S., Oliveras, S., Nogués-Correig, O., … D'Addio, S. (2012). Phase altimetry with dual polarization GNSS-R over sea ice. *IEEE Transactions on Geoscience and Remote Sensing*, *50*(6), 2112–2121. doi.org/10.1109/TGRS.2011.2172797

Fleming, E. L., Chandra, S., Barnett, J. J., & Corney, M. (1990). Zonal mean temperature, pressure, zonal wind and geopotential height as functions of latitude. *Advances in Space Research*, *10*(12), 11–59. doi.org/10.1016/0273-1177(90)90386-E

Hopfield, H. S. (1969). Two-Quartic Tropospheric Refractivity Profile for Correcting Satellite Data. *Journal of Geophysical Research*, *74*(18), 4487–4499. doi.org/10.1029/JC074i018p04487

Jin, S., Cardellach, E., & Xie, F. (2014). *GNSS Remote Sensing*. (F. D. Van Der Meer & A. Marçal, Eds.) (Vol. 19). Springer Netherlands. doi.org/10.1007/978-94-007-7482-7

Larson, K. M., Ray, R. D., Nievinski, F. G., & Freymueller, J. T. (2013). The Accidental Tide Gauge: A GPS Reflection Case Study From Kachemak Bay, Alaska, *10*(5), 1200–1204. doi.org/10.1109/LGRS.2012.2236075

Larson, K. M., Ray, R. D., & Williams, S. D. P. (2017). A 10-Year Comparison of Water Levels Measured with a Geodetic GPS Receiver versus a Conventional Tide Gauge. *Journal of Atmospheric and Oceanic Technology*, *34*(2), 295–307. doi.org/10.1175/JTECH-D-16-0101.1

Nafisi, V., Urquhart, L., Santos, M. C., Nievinski, F. G., Bohm, J., Wijaya, D. D., … Gegout, P. (2012). Comparison of Ray-Tracing Packages for Troposphere Delays. *IEEE Transactions on Geoscience and Remote Sensing*, *50*(2), 469–481. doi.org/10.1109/TGRS.2011.2160952

Nievinski, F. G., & Larson, K. M. (2014). Forward modeling of GPS multipath for near-surface reflectometry and positioning applications. *GPS Solutions*, *18*(2), 309–322. doi.org/10.1007/s10291-013-0331-y

Nievinski, F. G., & Santos, M. C. (2010). Ray-tracing options to mitigate the neutral atmosphere delay in GPS. *Geomatica*, *64*(2), 191–207.

Nikolaidou, T., Santos, C. M., Williams, D. P. S., & Geremia-Nievinski, F. (2020). Raytracing atmospheric delays in ground-based GNSS reflectometry. *Journal of Geodesy*, *94*(68). doi.org/10.1007/s00190-020-01390-8

Nilsson, T., Böhm, J., Wijaya, D. D., Tresch, A., Nafisi, V., & Schuh, H. (2013). Path Delays in the Neutral

Atmosphere. In S. H. Böhm J. (Ed.), *Atmospheric Effects in Space Geodesy* (pp. 73–136). Springer Atmospheric Sciences. Springer, Berlin, Heidelberg. doi.org/10.1007/978-3-642-36932-2_3

Rohm, W., & Bosy, J. (2009). Local tomography troposphere model over mountains area. *Atmospheric Research*, *93*(4), 777–783. doi.org/10.1016/J.ATMOSRES.2009.03.013

Roussel, N., Frappart, F., Ramillien, G., Darrozes, J., Desjardins, C., Gegout, P., … Biancale, R. (2014). Simulations of direct and reflected wave trajectories for ground-based GNSS-R experiments. *Geoscientific Model Development*, *7*(5), 2261–2279. doi.org/10.5194/gmd-7-2261-2014

Saastamoinen, J. (1972). Atmospheric Correction for the Troposphere and Stratosphere in Radio Ranging Satellites. In *Geophysical Monograph Series* (pp. 247–251). American Geophysical Union (AGU). doi.org/10.1029/GM015p0247

Santamaría-Gómez, A., & Watson, C. (2017). Remote leveling of tide gauges using GNSS reflectometry: case study at Spring Bay, Australia. *GPS Solutions*, *21*(2), 451–459. doi.org/10.1007/s10291-016-0537-x

Santamaría-Gómez, A., Watson, C., Gravelle, M., King, M., & Wöppelmann, G. (2015). Levelling co-located GNSS and tide gauge stations using GNSS reflectometry. *Journal of Geodesy*, *89*(3), 241–258. doi.org/10.1007/s00190-014-0784-y

Semmling, A. M., Schmidt, T., Wickert, J., Schn, S., Fabra, F., Cardellach, E., … Rius, A. (2012). On the retrieval of the specular reflection in GNSS carrier observations for ocean altimetry. *Radio Science*, *47*(6). doi.org/10.1029/2012RS005007

Treuhaft, R. N., Lowe, S. T., Zuffada, C., & Chao, Y. (2001). 2-cm GPS altimetry over Crater Lake. *Geophysical Research Letters*, *28*(23), 4343–4346. doi.org/10.1029/2001GL013815

Urquhart, L., Nievinski, F. G., & Santos, M. C. (2012). Ray-traced slant factors for mitigating the tropospheric delay at the observation level. *Journal of Geodesy*, *86*(2), 149–160. doi.org/10.1007/s00190-011-0503-x

Williams, S. D. P., & Nievinski, F. G. (2017). Tropospheric delays in ground-based GNSS multipath reflectometry-Experimental evidence from coastal sites. *Journal of Geophysical Research: Solid Earth*, *122*(3), 2310–2327. doi.org/10.1002/2016JB013612

Zavorotny, V. U., Gleason, S., Cardellach, E., & Camps, A. (2014). Tutorial on remote sensing using GNSS bistatic radar of opportunity. *IEEE Geoscience and Remote Sensing Magazine*, *2*(4), 8–45. doi.org/10.1109/MGRS.2014.2374220

5. Closed-form expressions for atmospheric delay and altimetry correction in ground-based GNSS reflectometry

Abstract[9]: Radio waves used in Global Navigation Satellite System Reflectometry (GNSS-R) are subject to atmospheric refraction, even for ground-based tracking stations in applications such as coastal sea-level altimetry. Although atmospheric delays are best investigated via ray-tracing, its modification for reflections is not trivial. We have developed closed-form expressions for atmospheric refraction in ground-based GNSS-R and validated them against raytracing. We provide specific expressions for the linear and angular components of the atmospheric interferometric delay and corresponding altimetry correction, parameterized in terms of refractivity and bending angle. Assessment results showed excellent agreement for the angular component and good for the linear one. There were small discrepancies towards the horizon as a consequence of approximating the layer refractivity by its mean value. About half of the delay was found to originate above the receiving antenna at low satellite elevation angles. We define the interferometric slant factor used to map interferometric zenithal delays to individual satellites. We also provide an equivalent correction for the effective satellite elevation angle such that the refraction effect is nullified. Lastly, we present the limiting conditions for negligible atmospheric altimetry correction (sub-cm), over domain of satellite elevation angle and reflector height. For example, for 5-meter reflector height,

---

[9] This chapter is based on a manuscript submitted to the journal IEEE Transactions on Geoscience and Remote Sensing: Nikolaidou, T., Santos, C. M., Williams, D. P. S., & Geremia-Nievinski, F., (2020). Closed-form expressions for atmospheric delay and altimetry correction in ground-based GNSS reflectometry. IEEE Transactions on Geoscience and Remote Sensing.

observations below 20-degrees elevation angle have more than 1-centimeter atmospheric altimetry error.

5.1. Introduction

Global navigation satellite system reflectometry (GNSS-R) has been widely applied for coastal sea level altimetry from ground-based tracking stations (Larson et al., 2013, 2017). Unfortunately, GNSS-R altimetry suffers from an atmospheric refraction bias (Williams & Nievinski, 2017). Its linear and angular components induce, respectively, speed retardation and direction bending on the radio wave. The result is a propagation delay as compared to the idealization of propagation in vacuum. For example, for a 10-m reflector height, the atmospheric altimetry correction reaches half-a-meter for a satellite near the horizon (Nikolaidou et al., 2020a) and is thus significant even for near-surface configurations (Santamaría-Gómez & Watson, 2017). It further increases exponentially with satellite elevation angle and linearly with reflector height, i.e., distance between the antenna and the surface.

Atmospheric models developed for direct or line-of-sight propagation, as used in GNSS positioning, cannot compensate for the total atmospheric refraction effect (Nikolaidou, Santos, Williams, & Geremia-Nievinski, 2020b). That is because the angular refraction experienced by the incoming rays in the upper atmospheric layer, i.e., the portion of the atmosphere above the antenna, does not necessarily cancel out when forming the interferometric delay, between reflection and direct delays. To overcome this problem, raytracing can be performed, solving for the reflection three-point boundary value problem, involving broadcasting satellite, reflecting surface, and receiving antenna (Kenneth D. Anderson, 2000; N. Roussel et al., 2014). A detailed description of an interferometric raytracing procedure is given in (Nikolaidou et al., 2020a), whose results are general and comprehensive but require a raytracing algorithm customized for reflections, which is not always available for GNSS-R researchers.

Here, we develop and present closed-form expressions for the atmospheric delay and corresponding altimetry correction in ground-based GNSS-R. They are parameterized in terms of ancillary meteorological information (average refractivity and elevation bending angle) besides the independent geometrical variables (reflector height and satellite elevation angle).

We validate the derived closed-form expressions by comparison to raytracing results based on a judicious choice of rectilinear raypaths (Nikolaidou et al., 2020b). In their turn, rectilinear raytracing has been previously validated by comparison to rigorous raytracing results (Nikolaidou et al., 2020a). We define the interferometric slant factor used to map interferometric zenithal delays to individual satellites. We also provide an equivalent correction for the effective satellite elevation angle such that the refraction effect is nullified. Finally, we provide the limiting conditions for significant atmospheric altimetry correction in terms of satellite elevation angle and reflector height; in other words, we indicate the observation conditions under which atmospheric refraction is negligible in ground-based GNSS-R.

5.2. Background: Delay Modelling and Raytracing

5.2.1. Atmospheric Delay Formulation

Here we briefly recapitulate the essential concepts of atmospheric refraction in GNSS-R (Nikolaidou et al., 2020a). The atmospheric delay

$$d = L - D, \tag{1}$$

is defined in terms of two intrinsic radio propagation quantities: the vacuum distance, $D = \|r_1 - r_2\|$ and the radio length, $L = \int_{r_1}^{r_2} n \, dl$, where n is the index of refraction; the integral is evaluated along the bent ray path, of infinitesimal arc length dl, between any two points. Introducing further the curve range, $R = \int_{r_1}^{r_2} 1 \, dl$, allows the definition of two atmospheric delay components,

$$d = (L - R) + (R - D) = d^a + d^g \tag{2}$$

the along-path atmospheric delay:

$$d^a = L - R = \int_{\boldsymbol{r}_1}^{\boldsymbol{r}_2} N \, dl \tag{3}$$

and the geometric atmospheric delay:

$$d^g = R - D \tag{4}$$

The definitions above can be applied to the direct path, between the transmitting satellite $\boldsymbol{r}_{\text{sat}}$ and the receiver antenna $\boldsymbol{r}_{\text{ant}}$, yielding $d_d = L_d - D_d = d_d^a + d_d^g$; and also to the reflection path, involving the refracted specular point on the surface $\boldsymbol{r}'_{\text{sfc}}$, yielding $d_r = L_r - D_r = d_r^a + d_r^g$ (Nikolaidou et al., 2020a).

Finally, the corresponding interferometric quantities result from the difference between reflection and direct quantities, for example: interferometric vacuum distance, $D_i = D_r - D_d$; interferometric radio length, $L_i = L_r - L_d$; and interferometric curve range: $R_i = R_r - R_d$. Hence, the interferometric atmospheric delay follows from two equivalent formulations:

$$d_i = d_r - d_d = L_i - D_i \tag{5}$$

This definition is extended to the interferometric delay components, $d_i = d_i^a + d_i^g$:

$$d_i^a = d_r^a - d_d^a = L_i - R_i \tag{6}$$

$$d_i^g = d_r^g - d_d^g = R_i - D_i \tag{7}$$

5.2.2. Atmospheric Raytracing

The above delay formulation normally is evaluated numerically based on rigorous raytracing. The bent raypath is determined solving the Eikonal equation (Born & Wolf, 1999):

$$\frac{\partial}{\partial l}(n\,\hat{\boldsymbol{t}}) = \boldsymbol{\nabla} n \tag{8}$$

where $\hat{\boldsymbol{t}} = \partial \boldsymbol{r}/\partial l$ is the ray tangent direction (a unit vector), $\boldsymbol{r}$ is the evolving ray vector position, l is the incremental arc length, and $\boldsymbol{\nabla} n = \boldsymbol{\nabla} N$ is the spatial gradient of index of refraction or refractivity, $N = n - 1$. A two-point boundary value problem (BVP) defines the direct raypath between the satellite and antenna position vectors ($\boldsymbol{r}_{\text{sat}}\ \boldsymbol{r}_{\text{ant}}$), and a three-point BVP defines the reflection, including additionally the refracted reflection point ($\boldsymbol{r}_{\text{sat}}, \boldsymbol{r}_{\text{ant}}, \boldsymbol{r}'_{\text{sfc}}$).

The derivation of the closed-form expressions for the atmospheric delay is facilitated by imposing a judicious choice of rectilinear raypaths (Nikolaidou et al., 2020b). The bent raypath is approximated by straight line segments of the form:

$$\boldsymbol{r} = \check{\boldsymbol{r}} + s \cdot \hat{\boldsymbol{t}} \tag{9}$$

where $\check{\boldsymbol{r}}$ is the initial ray position and s is the incremental ray distance. The ray trajectory is thus completely known in advance and hence one can avoid solving the Eikonal differential equation. The rectilinear results are denoted with an overhead bar, to distinguish from the rigorous results:

$$\bar{d}_i = \bar{d}_r - \bar{d}_d = \bar{L}_i - \bar{D}_i. \tag{10}$$

The rectilinear ray still travels in an inhomogeneous atmosphere, as is subject to linear refraction (speed retardation) and may also be subject to angular refraction, as described below.

Two variants of the rectilinear model were defined (Nikolaidou et al., 2020b). The first one is the *rectilinear geometric* (RG) model, based on the vacuum position vectors ($\boldsymbol{r}_{\text{sat}}, \boldsymbol{r}_{\text{ant}}, \boldsymbol{r}_{\text{sfc}}$). The second variant is the *rectilinear apparent* (RA) model, for which the refracted reflection point $\boldsymbol{r}'_{\text{sfc}}$ and apparent satellite position, $\boldsymbol{r}'_{\text{sat}}$ are considered in conjunction with the unchanged antenna vacuum position $\boldsymbol{r}_{\text{ant}}$. The satellite elevation angle bending due to refraction, $\delta e = e' - e$, is due to propagation *above* the antenna, thus it is obtained from a previous rigorous direct-path raytrace (Nikolaidou et al., 2020a).

In Table 5.1 the intrinsic radio propagation quantities for the two rectilinear raytracing procedures (RG and RA) are summarized for the direct, reflected and interferometric signals (RA quantities are distinguished from the respective RG ones by using a prime symbol). The atmospheric delay d, and its components d^a and d^g, were then formulated building on the propagation quantities as per eq. (5)-(7) for each rectilinear variant (Table 5.2) (Nikolaidou et al., 2020b).

Table 5.1: Definition of rectilinear propagation quantities

	Rectilinear Geometric (RG)		Rectilinear Apparent (RA)	
	Vacuum distance	Radio length	Vacuum distance	Radio length
Direct	$\overline{D}_d = \Vert\boldsymbol{r}_{\text{ant}} - \boldsymbol{r}_{\text{sat}}\Vert$	$\overline{L}_d = \int_{\boldsymbol{r}_{\text{ant}}}^{\boldsymbol{r}_{\text{sat}}} n\,ds$	$\overline{D}'_d = \Vert\boldsymbol{r}_{\text{ant}} - \boldsymbol{r}'_{\text{sat}}\Vert$	$\overline{L}'_d = \int_{\boldsymbol{r}_{\text{ant}}}^{\boldsymbol{r}'_{\text{sat}}} n\,ds$
Reflection	$\overline{D}_r = \Vert\boldsymbol{r}_{\text{ant}} - \boldsymbol{r}_{\text{sfc}}\Vert + \Vert\boldsymbol{r}_{\text{sfc}} - \boldsymbol{r}_{\text{sat}}\Vert$	$\overline{L}_r = \int_{\boldsymbol{r}_{\text{sfc}}}^{\boldsymbol{r}_{\text{sat}}} n\,ds + \int_{\boldsymbol{r}_{\text{ant}}}^{\boldsymbol{r}_{\text{sfc}}} n\,ds$	$\overline{D}'_r = \Vert\boldsymbol{r}_{\text{ant}} - \boldsymbol{r}'_{\text{sfc}}\Vert + \Vert\boldsymbol{r}'_{\text{sfc}} - \boldsymbol{r}'_{\text{sat}}\Vert$	$\overline{L}'_r = \int_{\boldsymbol{r}'_{\text{sfc}}}^{\boldsymbol{r}'_{\text{sat}}} n\,ds + \int_{\boldsymbol{r}_{\text{ant}}}^{\boldsymbol{r}'_{\text{sfc}}} n\,ds$
Interferometric	$\overline{D}_i = \overline{D}_r - \overline{D}_d$	$\overline{L}_i = \overline{L}_r - \overline{L}_d$	$\overline{D}'_i = \overline{D}'_r - \overline{D}'_d$	$\overline{L}'_i = \overline{L}'_r - \overline{L}'_d$

Table 5.2: Definition of rectilinear interferometric atmospheric delays

	Rectilinear Geometric	Rectilinear Apparent	Rectilinear Mixed
Total	$\bar{d}_i = \bar{d}_i^a + \bar{d}_i^g$ $\bar{d}_i = \bar{d}_i^a$	$\bar{d}'_i = \bar{d}'^a_i + \bar{d}'^g_i$ $\bar{d}'_i = \bar{d}'^a_i$	$\bar{\bar{d}}_i = \bar{\bar{L}}_i - \bar{\bar{D}}_i$ $\bar{\bar{d}}_i = \bar{\bar{d}}_i^a + \bar{\bar{d}}_i^g$
Along-path	$\bar{d}_i^a = \bar{L}_i - \bar{R}_i$ $\bar{d}_i^a = \bar{L}_i - \bar{D}_i$	$\bar{d}'^a_i = \bar{L}'_i - \bar{R}'_i$ $\bar{d}'^a_i = \bar{L}'_i - \bar{D}'_i$	$\bar{\bar{d}}_i^a = \bar{\bar{L}}_i - \bar{\bar{R}}_i$ $\bar{\bar{d}}_i^a = \bar{L}'_i - \bar{R}'_i$ $\bar{\bar{d}}_i^a = \bar{d}'^a_i$
Geometric	$\bar{d}_i^g = \bar{R}_i - \bar{D}_i$ $\bar{d}_i^g = 0$	$\bar{d}'^g_i = \bar{R}'_i - \bar{D}'_i$ $\bar{d}'^g_i = 0$	$\bar{\bar{d}}_i^g = \bar{\bar{R}}_i - \bar{\bar{D}}_i$ $\bar{\bar{d}}_i^g = \bar{R}'_i - \bar{D}_i$

Finally, a special combination of the RA and RG models was found (Nikolaidou et al., 2020b), called *rectilinear-mixed* (RM), that follows closely the rigorous raytracing results. RM, denoted with double overhead bar, utilizes the RG vacuum distance in conjunction with the RA radio length and the RA curve range:

$$\begin{aligned} \bar{\bar{D}} &= \bar{D} \\ \bar{\bar{R}} &= \bar{R}' \\ \bar{\bar{L}} &= \bar{L}' \end{aligned} \tag{11}$$

The specification of the RM delay and its components is provided in Table 5.2.

5.2.3. Atmospheric Layering

Here we recognize the role of the bottom atmospheric layer, between the receiving antenna and the reflecting surface. The layer thickness equals the antenna height or reflector depth, H. It complements the portion of the atmosphere above the antenna, responsible for the elevation bending δe.

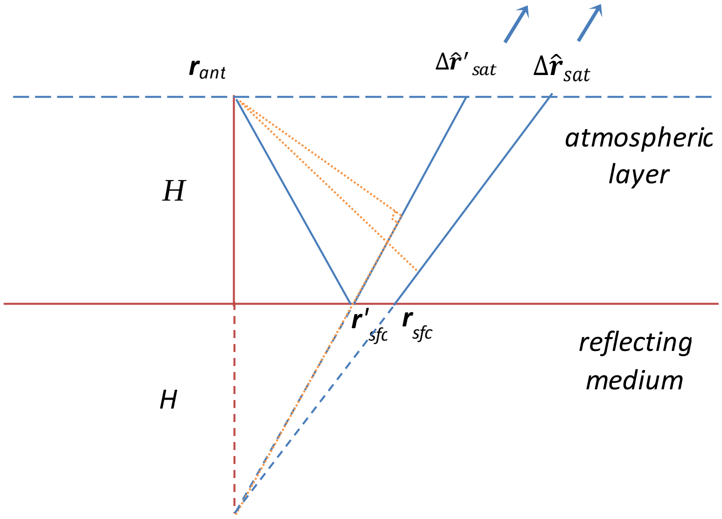

Figure 5.1: Refracted notable points and directions of rectilinear raytracing

We start by defining the *zenith interferometric atmospheric delay*:

$$d_i^z = d_r^z - d_d^z = 2(d_{\text{sfc}}^z - d_{\text{ant}}^z)$$

$$d_i^z = 2\int_{\boldsymbol{r}_{\text{sfc}}^z}^{\boldsymbol{r}_{\text{ant}}} N\,dl = 2\int_0^H N\,dH = 2HN_\ell^z \tag{12}$$

The vector $\boldsymbol{r}_{\text{sfc}}^z$ refers to the surface position immediately under the antenna. The quantity $N_\ell^z = d_i^z/H$ is the *average layer refractivity*; further assuming a thin atmospheric layer, it can be approximated as $N_\ell^z \approx (N_{\text{sfc}} + N_{\text{ant}})/2$, in terms of the refractivity at the surface and at the antenna height. With that we can factor out the *interferometric slant factor*:

$$f_i = d_i / d_i^z \tag{13}$$

which is responsible for mapping the zenith delay to a specific satellite elevation angle.

To further pave the way for the development of closed-form expressions, we define the *layer slant distance* in the rectilinear-geometric formalism:

$$\overline{D}_\ell = 2\Delta r_{\mathrm{sfc}} \tag{14}$$

It is twice the slant distance from antenna to the surface, $\Delta r_{\mathrm{sfc}} = \|\Delta \boldsymbol{r}_{\mathrm{sfc}}\|$, in terms of the relative position vector $\Delta \boldsymbol{r}_{\mathrm{sfc}} = \boldsymbol{r}_{\mathrm{sfc}} - \boldsymbol{r}_{\mathrm{ant}}$. By analogy, in the rectilinear-apparent formalism, the layer slant distance is:

$$\overline{D}'_\ell = 2\Delta r'_{\mathrm{sfc}} \tag{15}$$

involving the distance from antenna to the refracted surface specular point, $\Delta r'_{\mathrm{sfc}} = \|\boldsymbol{r}'_{\mathrm{sfc}} - \boldsymbol{r}_{\mathrm{ant}}\|$.

5.3. Closed-form Expressions

Based on the principles above, now we report the closed-form expressions, denoted with an overhead tilde. They were derived for the atmospheric delay components as well as for the atmospheric altimetry correction.

5.3.1. Interferometric Atmospheric Delay

Assuming a flat and horizontal reflecting surface at a small depth H below the antenna (Figure 5.1) establishes a symmetric configuration, where the direct and reflected angles of incidence are equal. The *closed-form interferometric vacuum distance* is well-known to be:

$$\widetilde{D}_i = 2H \sin e \tag{16}$$

By analogy, *the closed-form apparent interferometric vacuum distance* is:

$$\widetilde{D}_i' = 2H\sin e' \qquad (17)$$

It is based on the *apparent elevation angle* $e' \approx e_d'$, here approximated as that experienced along the direct path. With the last two equations, we can define the *closed-form interferometric atmospheric geometric delay* as:

$$\tilde{d}_i^g = \widetilde{D}_i' - \widetilde{D}_i = 2H(\sin\tilde{e}' - \sin e) \cong 2H\delta\tilde{e}\cos e \qquad (18)$$

where $\delta\tilde{e} = \tilde{e}' - e \approx \delta\tilde{e}_d$ is the elevation bending, here approximated as that experienced along the direct path. It is also proportional to reflector height H, so it is not necessarily negligible, unless the elevation bending δe is also small. The approximation on the right-hand side is derived from the angle-sum and small-angle trigonometric identities and requires $\delta\tilde{e}$ to be expressed in radians.

Next, we define the *closed-form layer slant distance (in the apparent formalism)*, based on $\tilde{e}'$:

$$\widetilde{D}_\ell' = 2H/\sin\tilde{e}' \qquad (19)$$

We use it to define the *closed-form interferometric atmospheric along-path delay* as:

$$\tilde{d}_i^a = \widetilde{N}_\ell^z\widetilde{D}_\ell' = \tilde{d}_i^z/\sin\tilde{e}' \cong 2H\widetilde{N}_\ell^z\csc\tilde{e}' \qquad (20)$$

Notice that it is directly proportional to reflector height H while it depends indirectly on the station altitude via the average layer refractivity $\widetilde{N}_\ell^z$.

Finally, the *closed-form total interferometric atmospheric delay* is simply the sum of the two components above:

$$\tilde{d}_i = \tilde{d}_i^a + \tilde{d}_i^g = 2H\widetilde{N}_\ell^z/\sin\tilde{e}' + 2H\delta\tilde{e}\cos e \qquad (21)$$

It should be emphasized that the ancillary meteorological information (average refractivity N and elevation bending $\delta\tilde{e}$) can be obtained from direct/line-of-sight raytracing. However, in case such output is not available, empirical models such as the Global Pressure and Temperature (GPT) (Lagler, Schindelegger, Böhm, Krásná, & Nilsson, 2013; Landskron & Böhm, 2017) can be used to obtain the refractivity at the station and models such as that of (Bennett, 1982; Hobiger, Ichikawa, Koyama, & Kondo, 2008) can be used to approximate the elevation bending.

5.3.2. Interferometric Slant Factors

Slant factors help cancel out the zenith delay effects. For example, the *closed-form interferometric atmospheric along-path slant factor* reads:

$$\tilde{f}_i^{\,a} = \frac{\tilde{d}_i^a}{\tilde{d}_i^z} = \frac{1}{\sin \tilde{e}'} = \csc \tilde{e}' \tag{22}$$

Analogously, for the *closed-form interferometric atmospheric geometric slant factor* we can write:

$$\tilde{f}_i^{\,g} = \frac{\tilde{d}_i^g}{\tilde{d}_i^z} = \frac{\sin \tilde{e}' - \sin e}{\tilde{N}_\ell^z} \cong \frac{\delta \tilde{e} \cos e}{\tilde{N}_\ell^z} \tag{23}$$

The expression for the *closed-form interferometric total slant factor* yields as:

$$\tilde{f}_i \quad = \tilde{f}_i^{\,a} + \tilde{f}_i^{\,g} = \csc \tilde{e}' + \delta \tilde{e} \cos e / \tilde{N}_\ell^z$$

5.3.3. Atmospheric Altimetry Correction

The atmospheric altimetry correction can be derived analytically for the closed-form delay expressions above based on the altimetry retrieval technique employed by a particular instrument.

The first one follows from half the rate of change of atmospheric delay with respect to the sine of the elevation angle (Nikolaidou et al., 2020a). Equivalently, it can be expressed as the product of zenith delay and half the rate of change of the slant factor:

$$\Delta H = -0.5\, \partial d / \partial \sin e = -0.5\, d_i^z\, \partial f / \partial \sin e \tag{24}$$

$$\begin{aligned}
\frac{\Delta \widetilde{H}_i^a}{H} &= \frac{\widetilde{N}_\ell^z}{\sin^2 e'}\left(1 + \frac{\partial \delta e}{\partial e}\right) \approx \frac{\widetilde{N}_\ell^z}{\sin^2 e'} \\
\frac{\Delta \widetilde{H}_i^g}{H} &= -\delta \tilde{e}' \tan e \left(1 + \frac{\partial \delta \tilde{e}'}{\partial e}\right) + \frac{\partial \delta \tilde{e}'}{\partial e} \approx \frac{\partial \delta e}{\partial e}
\end{aligned} \tag{25}$$

The dependence on reflector height H is emphasized by normalization of the altimetry corrections on the left-hand side of the equations, forming relative altimetry corrections. Also evident is the dependence on the elevation bending δe (which must be expressed in radians when used as multiplicative factor) as well as its rate of change with respect to geometric elevation angle $\partial \delta e / \partial e$.

For completeness we report a second set of closed-form altimetry correction expressions, derived using the absolute-ratio retrieval technique (Nikolaidou et al., 2020a):

$$\begin{aligned}
\frac{\Delta \widetilde{H}_i^a}{H} &= \frac{\widetilde{N}_\ell^z}{\sin e' \sin e} \\
\frac{\Delta \widetilde{H}_i^g}{H} &= \frac{\sin \tilde{e}' - \sin e}{\sin e} \cong \delta \tilde{e} \cot e
\end{aligned} \tag{26}$$

The first set of expressions () can be adopted by a number of retrieval algorithms that utilize the “phase stopping” approach (Zavorotny et al., 2014), including interferometric Doppler measurements (A. M. Semmling et al., 2012) and multipath signal-to-noise ratio (SNR) measurements (Larson et al., 2013). On the other hand, the second set of eq.(26) is to be applied with the “phase anchoring” approach (Zavorotny et al., 2014), using ambiguity-fixed carrier-phase observables (Löfgren, Haas, Scherneck, & Bos, 2011; Martin-Neira, Colmenarejo, Ruffini, & Serra, 2002) or code-phase pseudorange observables (Rius et al., 2012). Here we focus on the former formulation because we assume SNR as the main observable.

5.3.4. Atmospheric Elevation Correction

A final closed-form expression is motivated by limitations of existing GNSS-R altimetry retrieval software. They may rely only on modifying the satellite elevation angle to compensate for atmospheric refraction, with no possibility of using the total atmospheric interferometric delay explicitly[10]. We thus define an *atmospheric elevation angle correction* as,

$$\delta e^* = \operatorname{asin}\left(\frac{d_i + \ D}{2H}\right) - e \tag{27}$$

It is based on a fictious satellite elevation angle $e^* = e + \delta e^*$ such that, when input to the ordinary vacuum delay formula, produces the total radio length. In its turn, when subtracted from the vacuum distance, it reproduces the total interferometric atmospheric delay:

$$d_i \ = 2H \sin(e + \delta e^*) - 2H \sin e \,. \tag{28}$$

Applying the angle-sum and small-angle trigonometric identities, the atmospheric elevation angle correction can be approximated by:

$$\delta e^* = \delta e \quad + N/(\sin e \cos e) \tag{29}$$

where the result is expressed in radians. This formulation is general and valid for any type of raytracing (rigorous or rectilinear); when it is based on closed-form expressions for the delays, it may be denoted as $\delta \tilde{e}^*$. It should be noted that the usage of (Santamaría-

---

[10] (akin to retracking (Park et al., 2012))

Gómez & Watson, 2017) corresponds to the first term in the last equation ($\delta e^* \cong \delta e$), while the usage of (Purnell et al., 2020) seems equivalent to approximating the elevation correction with only the second term ($\delta e^* \cong N/(\sin e \cos e)$).

5.4. Results

In the following, we assess all closed-form expressions developed above, by comparison to the rectilinear-mixed (RM) raytracing results. As atmospheric model, we used the CIRA climatology (Fleming et al., 1990), which neglects humidity. A fixed 10-m reflector height is employed throughout, as a value representative of ground-based GNSS-R stations. For completeness, we also include an ad-hoc model introduced in (Treuhaft et al., 2001) and assessed by (Williams & Nievinski, 2017):

$$\tilde{d}_i^* = d_i^z \cdot f_d \tag{30}$$

where $f_d = d_d / d_d^z$ is the direct slant factor, obtained from rigorous raytracing. The corresponding altimetry correction $\Delta\tilde{H}_i^* = 0.5\, \partial \tilde{d}_i^* / \partial \sin e$, is obtained via numerical differentiation. The same numerical approach is used to obtain altimetry corrections from the rectilinear raytracing delay results, henceforth called “hybrid” results.

5.5.1 Atmospheric Delay

Figure 5.2 (top) displays the total delay and its components. Overall, there is excellent agreement between closed-form $\tilde{d}_i$ and the respective rectilinear-mixed (RM) term $\bar{\bar{d}}_i$, whose discrepancy is shown in the bottom panel of Figure 5.2.

For the atmospheric along-path delay, the agreement between $\tilde{d}_i^a$ and $\bar{\bar{d}}_i^a$ is nearly exact at high elevations and it remains at the millimeter level at low elevations, where the discrepancy grows exponentially, reaching 3 mm or 7% near the horizon. For the atmospheric geometric delay, $\tilde{d}_i^g$ has near exact agreement with $\bar{\bar{d}}_i^g$ throughout the elevation angle domain.

Finally, the ad-hoc formulation, $\tilde{d}_i^*$, follows closely the RM along-path results; the discrepancy $\tilde{d}_i^* - \bar{\bar{d}}_i^a$, Figure 5.2 (bottom), is similar to $\tilde{d}_i^a - \bar{\bar{d}}_i^a$, albeit with reversed sign and slightly smaller magnitude. The discrepancy with respect to the total delay, $\tilde{d}_i^* - \bar{\bar{d}}_i$, is 5 cm at the lowest elevation angle. Thus, the ad-hoc is seen not to be an adequate replacement for the total interferometric atmospheric delay.

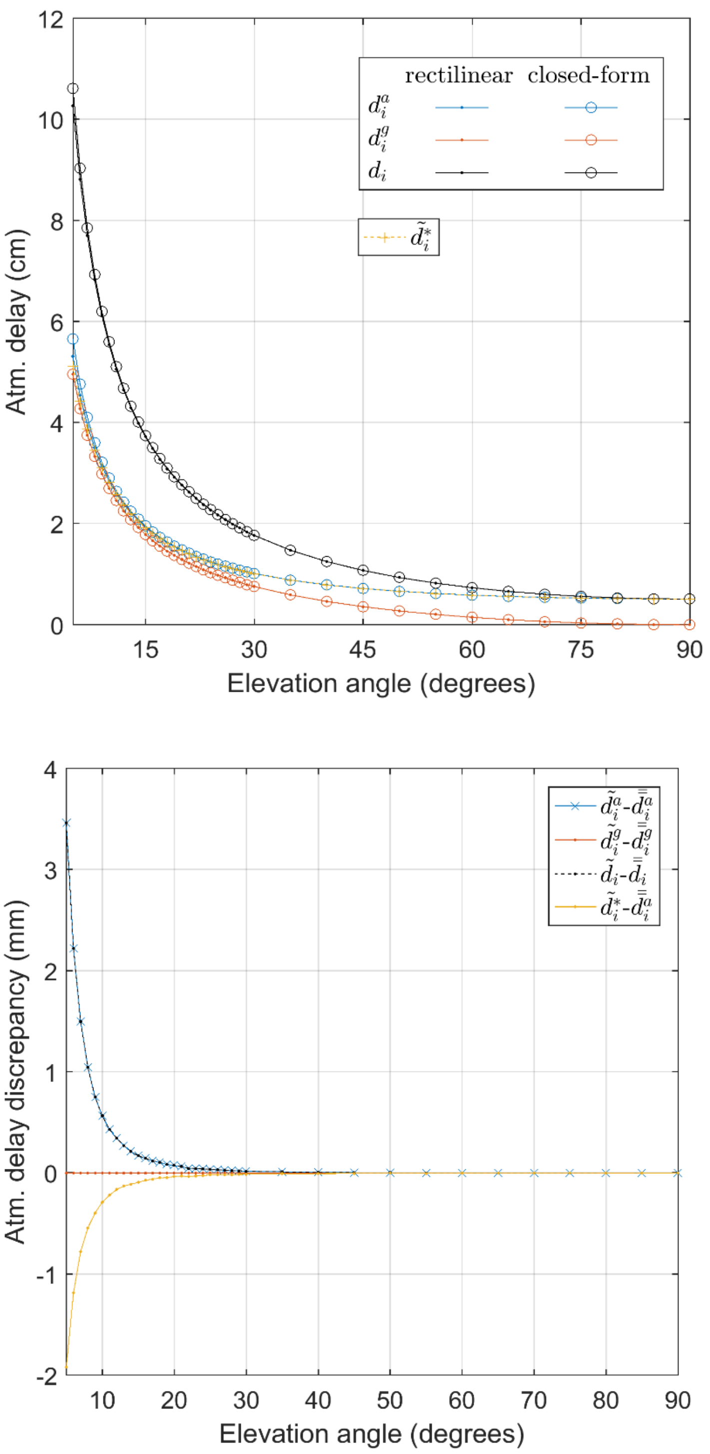

Figure 5.2: Interferometric atmospheric delay (top) and its discrepancy (bottom) as a function of satellite elevation angle (for a fixed 10-m reflector height).

5.4.1. Slant Factors

In Figure 5.3 (top) the total slant factors and their components are presented. There is excellent agreement between closed-form and the respective RM terms, whose discrepancy is shown in the bottom panel of the same figure. For the along-path slant factor, the agreement between $\tilde{f}_i^a$ and $\bar{\bar{f}}_i^a$ is exact at high elevations and assuming a nominal interferometric zenith delay of 5 mm, it remains at the millimeter level at low elevations; near the horizon, the discrepancy grows exponentially, reaching 7% or 7 cm/m.

The atmospheric geometric slant factor, $\tilde{f}_i^g$, has near exact agreement with the RM result, $\bar{\bar{f}}_i^g$, for all elevation angles. For the total slant factor, the discrepancy between closed-form $\tilde{f}_i$ and RM $\bar{\bar{f}}_i$ is dominated by the discrepancy $\tilde{f}_i^a - \bar{\bar{f}}_i^a$ previously discussed.

Finally, the direct slant factor, f_d, follows closely the RM along-path results (Figure 5.3, top). In the bottom panel of Figure 5.3, the discrepancy $f_d - \bar{\bar{f}}_i^a$ is similar to $\tilde{f}_i^a - \bar{\bar{f}}_i^a$, albeit with reversed sign and slightly smaller magnitude. Thus, if f_d were to be used to compute the total delay the error would reach 5 cm at the lowest elevation angle (Figure 5.3, inset).

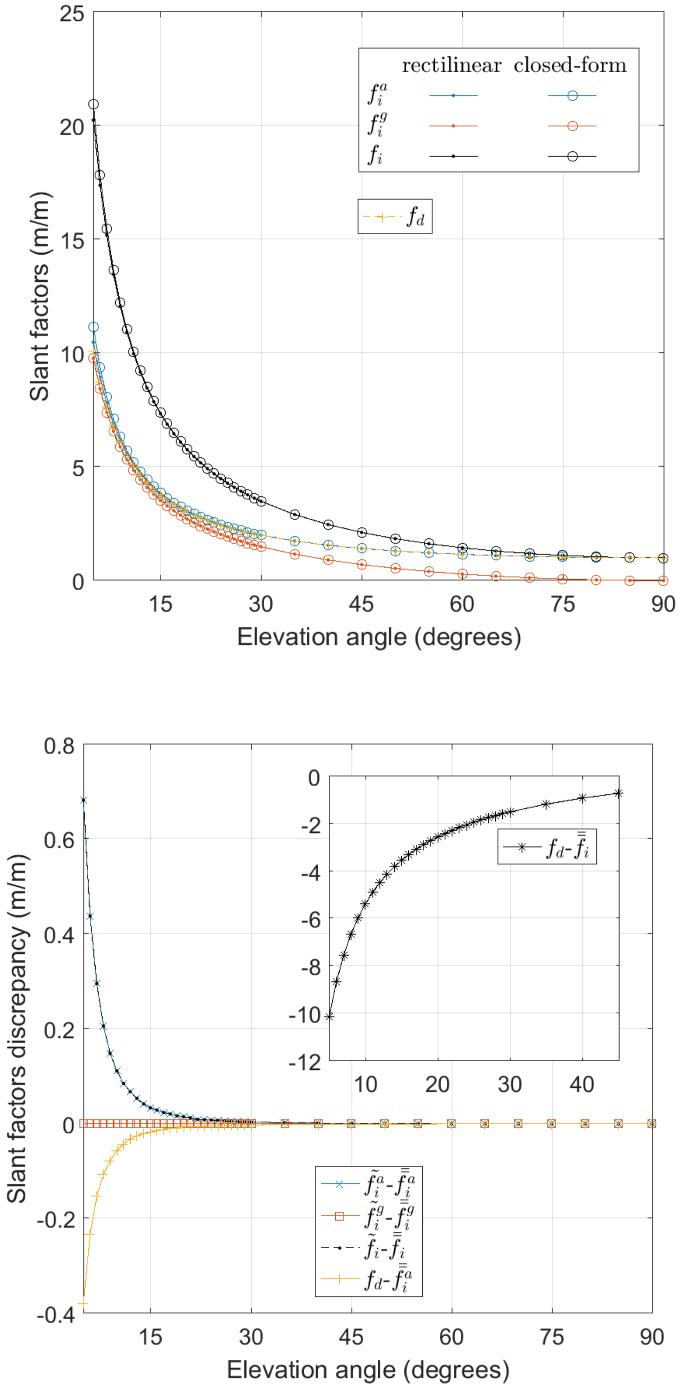

Figure 5.3: Interferometric slant factor and components (top), their discrepancy (middle), and the discrepancy of the direct slant factor with respect to the total interferometric (bottom), as a function of satellite elevation angle.

Figure 5.4 highlights that interferometric along-path atmospheric delay $\bar{d}_i'^{a}$ is closely related to the layer slant distance $\bar{D}'_\ell$ and unrelated to the interferometric vacuum distance $\bar{D}'_i$. With respect to the trigonometric components $\csc \tilde{e}'$ and $\delta\tilde{e} \cos e$ involved in, respectively, $\tilde{d}_i^a$ and $\tilde{d}_i^g$, it is interesting to see the similarity in their graphs (Figure 5.3, top), despite having very different formulas. It is also worth noticing that although the trigonometric elements differ largely in order of magnitude, this is compensated to some extent by the refractivity value ($N \cong 0.0003$). The ratio of the two closed-form delay components reads:

$$\frac{\tilde{d}_i^g}{\tilde{d}_i^a} = \frac{\delta\tilde{e} \cos e \sin \tilde{e}'}{\tilde{N}_\ell^z}$$

It attains almost unity at 10-degree elevation (Figure 5.5) where the two delay components are almost balanced. Also, for the conditions considered, $\tilde{d}_i^a$ is always greater than $\tilde{d}_i^g$.

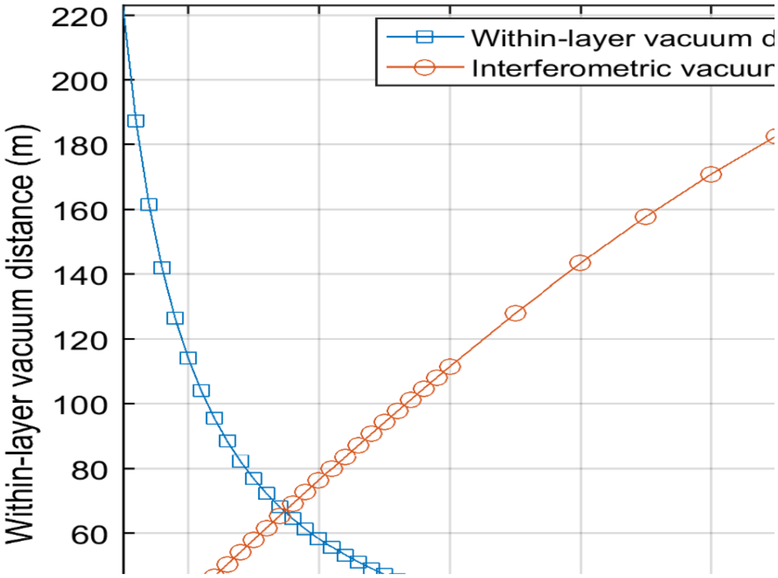

Figure 5.4: Within-layer vacuum distance (left axis) and interferometric vacuum distance (right axis), both as a function of satellite elevation angle (for a fixed 10-m reflector height).

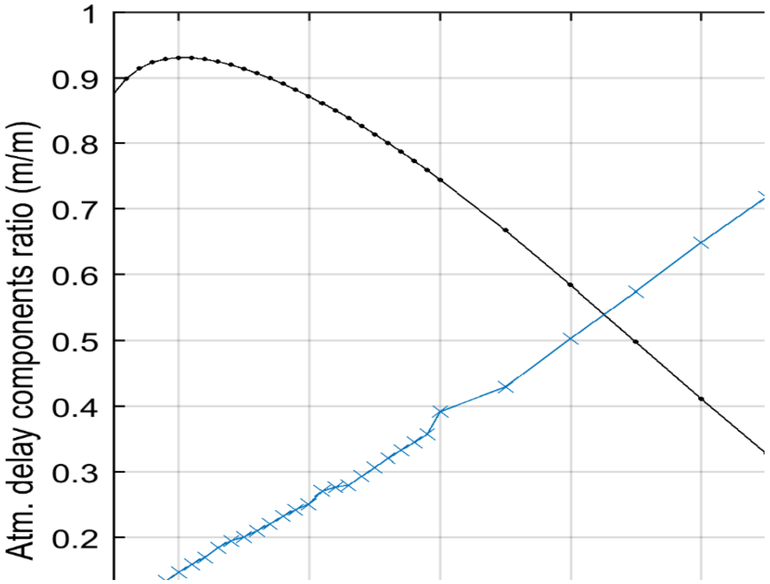

Figure 5.5: Ratio of closed-form atmospheric delay components (black line) and altimetry correction components (blue line) – geometric over along-path – as a function of satellite elevation angle.

5.4.2. Atmospheric Altimetry Correction

Now turning to the atmospheric altimetry correction (eq.(25)), we show it normalized by reflector height, in units of centimeters per meter (Figure 5.6, top). For example, for a satellite at 5-degrees elevation angle, it corresponds to a relative atmospheric altimetry correction of 4.5 cm/m, which scales to 45 cm for a reflector height of 10-m; on the other hand, near zenith, the correction amounts to 0.8 mm/m or 8 mm for a 10-m reflector height.

The inset at Figure 5.6 (top) emphasizes that the geometric altimetry correction component converges to a constant value (0.5 mm/m) at zenith, despite the respective geometric delay component converging to zero. This is explained by the definition of the altimetry correction, based on the rate of change with respect to the sine of the satellite elevation angle. In addition, contrarily to the delay components, at high elevation angles, the geometric altimetry correction is larger than the respective along-path component.

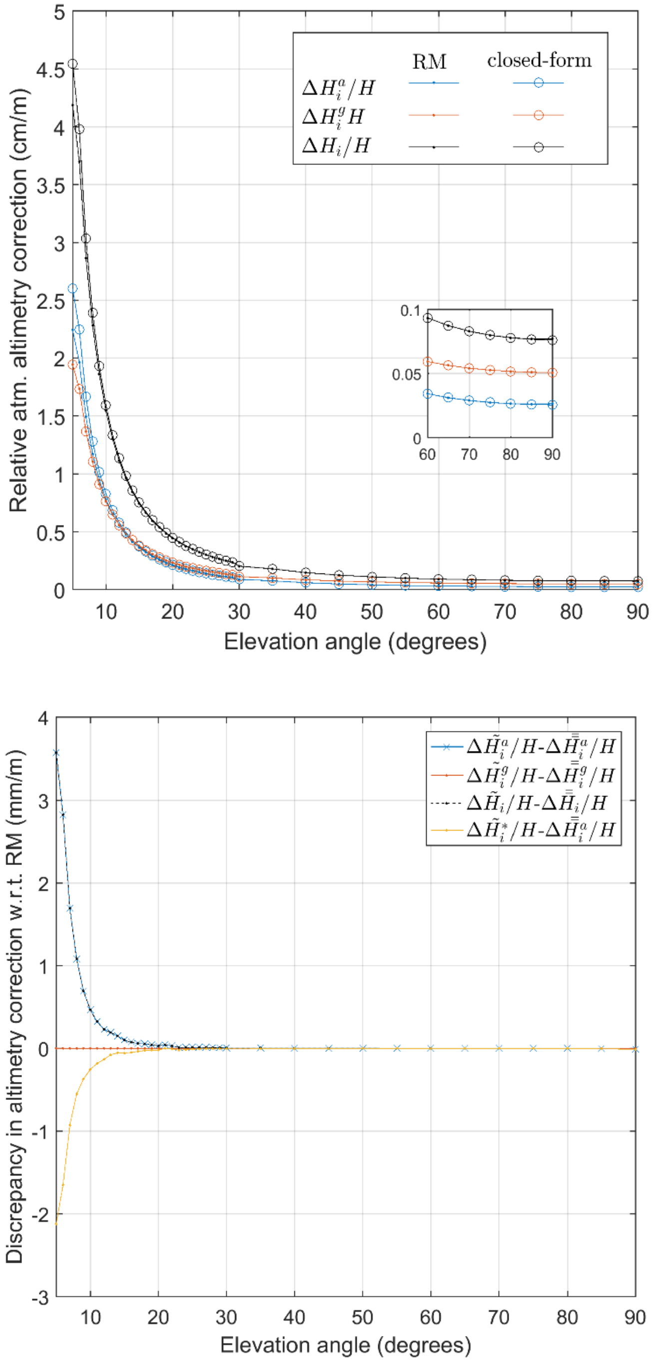

Figure 5.6: Relative atmospheric altimetry correction (top) and its discrepancy (bottom) as a function of satellite elevation angle.

The agreement between closed-form and RM (Figure 5.6, bottom) is good for the along-path component, with the discrepancy $\Delta\widetilde{H}_i^a - \Delta\overline{\overline{H}}_i^a$ remaining smaller than a tenth of the correction. The agreement is excellent for the geometric atmospheric altimetry correction, where $\Delta\widetilde{H}_i^g - \Delta\overline{\overline{H}}_i^g$ is negligible for all practical purposes. The closed-form total atmospheric altimetry correction follows closely the RM results; the corresponding discrepancy $\Delta\widetilde{H}_i - \Delta\overline{\overline{H}}_i$ is dominated by the discrepancy in the along-path component which remains less than 5 mm even at the low elevation angles. The ad-hoc model, $\Delta\widetilde{H}_i^*$, agrees with the along-path term, $\Delta\overline{\overline{H}}_i^a$, and misses the geometric contribution $\Delta\overline{\overline{H}}_i^g$.

The ratio of the respective altimetry correction components:

$$\frac{\Delta\widetilde{H}_i^g}{\Delta\widetilde{H}_i^a} = \frac{\partial\delta e/\partial e}{\widetilde{N}_\ell^z/\sin^2 e'}$$

is also shown in Figure 5.5 and behaves in the opposite way to the delay ratio. The geometric component is larger than the along-path one for most of the elevation angle domain. The ratio is balanced at 12-degree satellite elevation angle due to the rate of change with respect to the elevation angle. Near zenith, although the absolute altimetry correction is minimal, the ratio approaches its maximum; at 85-degrees satellite elevation angle, the geometric altimetry correction is almost twice the along-path one.

5.4.3. Cutoff Elevation Angle

We investigate the limiting conditions for negligible atmospheric altimetry correction by showing in Figure 5.7 the closed-form atmospheric altimetry correction as contour lines over a bivariate domain of satellite elevation angle and reflector height. The plot can be interpreted following an atmospheric altimetry correction contour line or along either a set reflector height or a cut-off elevation angle.

For instance, when reflector height equals 1 m, a 13° cut-off elevation angle corresponds to a negligible correction, of less than 1 cm. If a greater reflector height is utilized, the cutoff elevation angle grows almost linearly, e.g., it is 19° at a 2-m reflector height and 30°at 5 m. For an antenna located at an altitude of 50 m above the reflecting surface, the altimetry correction is at least 10 cm for any satellite observed above 30°elevation angle; applying nothing but a tighter elevation cut-off angle of 55° would reduce the altimetry error to 5 cm.

From another point of view, the same satellite would produce an altimetry error proportional to the reflector height at which is observed. For example, an error of nearly 0.1 cm and 10 cm correspond to a satellite at 30° elevation angle when observed from antennas located at almost 0.5 m and 50 m above the surface, respectively. These results are consistent with the ratio of the altimetry correction components shown in Figure 5.5 and highlight the contribution of the geometric component of the delay, present even when there is little bending, i.e., near zenith.

Taking the 1-cm threshold for each altimetry correction component (Figure 5.7, bottom), we see that they vary with reflector height like the total correction[11]. For example, assuming a 12° cut-off elevation angle, it is apparent that the relative along-path altimetry correction is always smaller than the geometric one. Alternatively, for the same satellite elevation angle a higher reflector height can be applied, e.g., at 40° elevation angle the limiting reflector height is 16 m or 11.5 m, should one consider either the along-path or the geometric altimetry correction only.

---

[11] The numerical derivative is based on a 3-point centered finite difference, as implemented by function "gradient" from MathWorks. As a consequence, a kink appears in the plot at 30 degrees, where the sampling in elevation changes from 1 degree to 5 degrees. Had we adopted a uniform spacing or utilized an improved numerical derivative implementation (e.g., a 5-point stencil), this artifact would likely disappear.

The combination of both components naturally drops the limiting reflector height, to 6.7 m. At very high elevation angles, where both altimetry correction components are minimum, the limiting reflector height for the along-path component approaches twice the respective geometric; e.g., near zenith, the limiting reflector height is 38.5 m and 20 m for the along-path and geometric altimetry correction components, respectively. On the other hand, near the horizon (below 12° elevation angle) the roles flip, with a lower effective reflector height for the along-path component than the geometric, yet with a minimal difference.

In summary, for a given altimetry correction threshold, the limiting reflector height increases while the elevation angle window narrows. It is evident that the atmospheric correction plays an important role when it comes to the observation planning. If no altimetry correction is applied, for a fixed reflector height the maximum cutoff elevation angle will limit the number of observations. Equivalently, employing a low cutoff elevation angle requires an equally low reflector height. Of course, lower elevation angles can be exploited even at high reflector heights, if the altimetry correction model of eq.(25) or eq.(26) is applied.

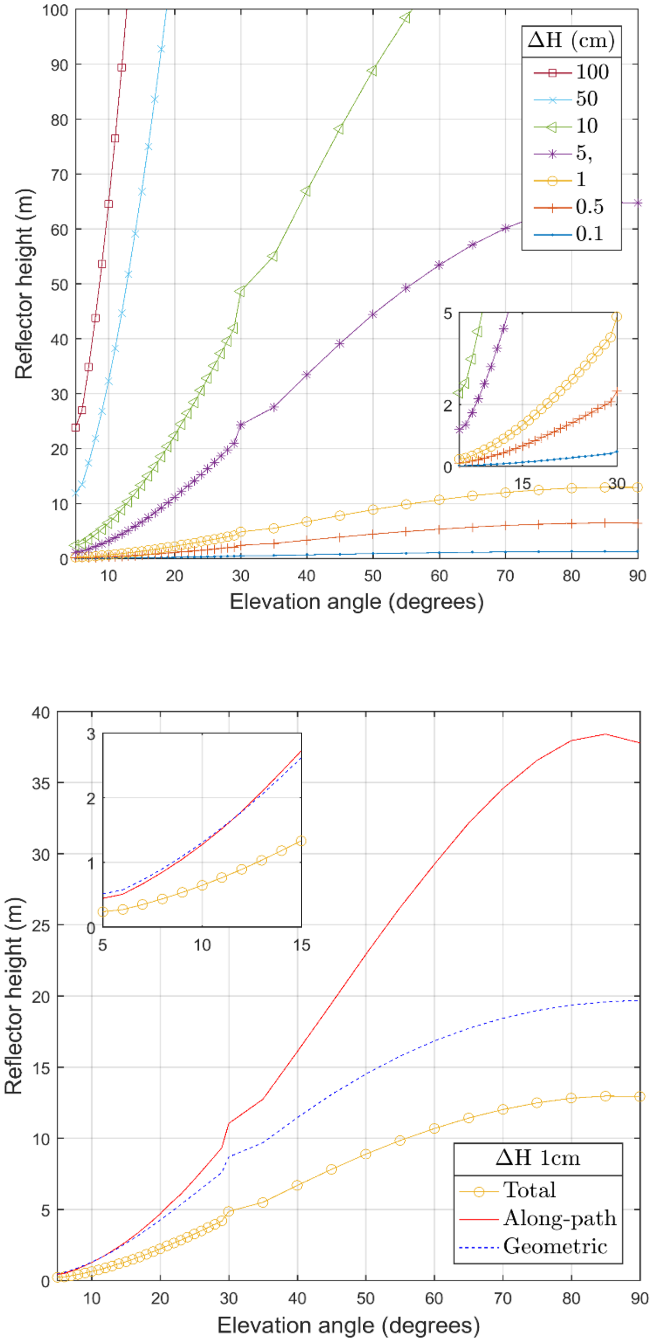

Figure 5.7: Closed-form atmospheric altimetry correction as contor lines over domain of satellite elevation angle and reflector height.

5.4.4. Atmospheric Elevation Correction

The atmospheric elevation correction δe^* (eq.(27)), resembles twice the interferometric bending $\delta e = e' - e$ with an average difference of about 50% throughout the elevation angle range (Figure 5.8). The difference is minimum (0.03°) at 45° elevation while it raises at the edges i.e., 0.16° and 0.18° at satellite elevation angles of 5° and 85°, respectively. It is especially pronounced near zenith, where the elevation correction has to account for the along-path delay, in addition to the elevation bending. In other words, the effect of the linear refraction is approximated by a fictious angular one.

Thus, the formulation is inapplicable at zenith, where the arcsine would return a complex number.

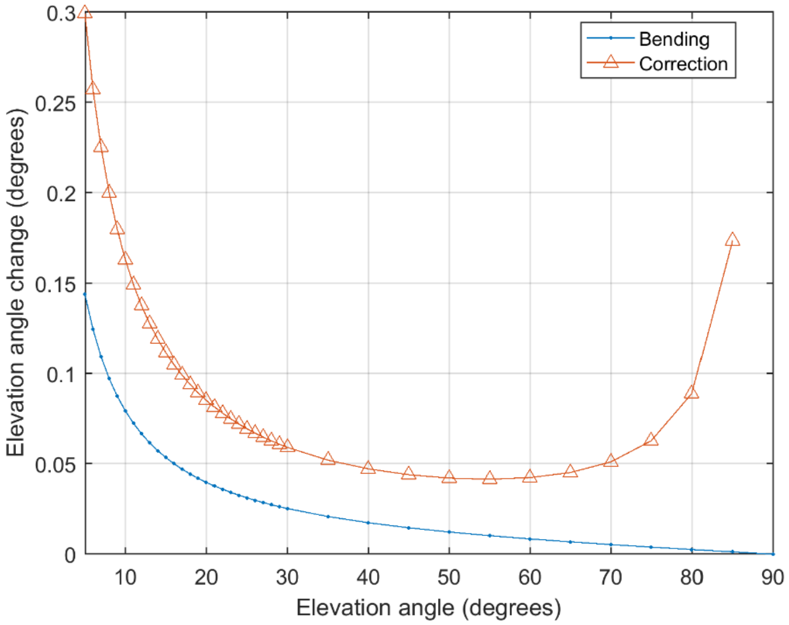

Figure 5.8: Elevation angle correction and interferometric bending as a function of satellite elevation angle.

5.5. Conclusions

In this study, we derived and validated closed-form expressions for the interferometric atmospheric delay, valid for a flat and horizontal reflecting surface at a small depth below the receiving antenna. We also provided closed-form atmospheric altimetry correction expressions for unbiased sea-level retrievals.

Firstly, we described and formulated the intrinsic propagation quantities based on two geometric quantities: satellite elevation angle and reflector height. A greater insight into the physics of the problem was given by considering the atmospheric layer between antenna and surface. This revealed that even small reflector heights are still subject to the atmospheric refraction originating above the receiving antenna.

Next, the closed-form expression for the interferometric along-path delay was given as a function of the layer slant distance and the mean refractivity. The interferometric geometric delay was computed as the difference between the refracted and unrefracted interferometric distances. The summation of the two yielded the total delay. We then extended the delays' definitions to the respective slant factors by factoring out the zenith delay. The corresponding atmospheric altimetry correction was derived via analytical formulas and approximations thereof. Finally, we presented the elevation correction that can be utilized in place of the apparent satellite elevation angle to sufficiently correct for the total atmospheric delay, featuring an easy adaptation in existing GNSS-R software.

We assessed the closed-form expressions against rectilinear raytracing results, which in turn had been previously validated against rigorous raytracing. The interferometric geometric atmospheric delay exhibited excellent agreement, with negligible discrepancies compared to raytracing. The interferometric along-path atmospheric delay showed good agreement to raytracing, with discrepancies that grew towards the horizon but remained within few mm. Finally, the ad-hoc or direct/line-of sight model proved insufficient to predict the total delay, as it can approximate only the along-path component, thus neglecting the geometric atmospheric delay which measures half of the delay at low satellite elevation angles.

Slant factors showed similar to the delays results and the discussion on their trigonometric elements highlighted the similarity of the two components latter albeit their differences in scale. The corresponding atmospheric altimetry corrections were similarly derived and validated. The closed-form formulas revealed a direct dependence on the reflector height. Their assessment against raytracing followed similar conclusions as for the atmospheric delays.

Lastly, we presented the limiting conditions for neglecting any atmospheric altimetry correction, in terms of a cutoff satellite elevation for variable reflector height. For example, at a reflector height of 1 m the cut-off elevation angle should be 13 degrees to keep the altimetry correction below 1 cm. As the tolerance increases, so does the effective reflector height but the elevation angle window narrows. The same 1-cm altimetry correction would impose a cut-off elevation angle of 30 degrees if observed by a 5-m reflector height. In any case, these cutoffs can be surpassed with the application of the correction expressions here developed.

It should be highlighted that the closed-form expressions need no reflection raytracing, only line-of-sight raytracing so as to obtain the elevation bending and mean refractivity as input. Tabulations of elevation bending and mean refractivity may be used by GNSS-R users with no access to raytracing software.

Many neglected effects also need to be considered in the future, such as: atmospheric humidity (instead of just dry gases); curvature of the Earth (spherical reflecting surface instead of a tangent plane); geographical variations (station latitude, longitude, altitude); temporal variations (time of day, day of year, year-to-year); greater reflector height variations (thicker atmospheric layer); and directional variations (satellite azimuth).

References

Anderson, K. D. (2000). Determination of Water Level and Tides Using Interferometric Observations of GPS Signals. *Journal of Atmospheric and Oceanic Technology*, *17*(8), 1118–1127. doi.org/10.1175/1520-0426(2000)017<1118:DOWLAT>2.0.CO;2

Bennett, G. G. (1982). The Calculation of Astronomical Refraction in Marine Navigation. *Journal of Navigation*, *35*(02), 255. doi.org/10.1017/S0373463300022037

Born, M., & Wolf, E. (1999). *Principles of optics Electromagnetic theory of propagation, interference and diffraction of light* (7th expand). Cambridge University Press. doi.org/10.1017/CBO9781139644181

Fleming, E. L., Chandra, S., Barnett, J. J., & Corney, M. (1990). Zonal mean temperature, pressure, zonal wind and geopotential height as functions of latitude. *Advances in Space Research*, *10*(12), 11–59. doi.org/10.1016/0273-1177(90)90386-E

Hobiger, T., Ichikawa, R., Koyama, Y., & Kondo, T. (2008). Fast and accurate ray-tracing algorithms for real-time space geodetic applications using numerical weather models. *Journal of Geophysical Research Atmospheres*, *113*(20), 1–14. doi.org/10.1029/2008JD010503

Lagler, K., Schindelegger, M., Böhm, J., Krásná, H., & Nilsson, T. (2013). GPT2: Empirical slant delay model for radio space geodetic techniques. *Geophysical Research Letters*, *40*(6), 1069–1073. doi.org/10.1002/grl.50288

Landskron, D., & Böhm, J. (2017). VMF3/GPT3: refined discrete and empirical troposphere mapping functions. *Journal of Geodesy*, *92*(4), 349–360. doi.org/10.1007/s00190-017-1066-2

Larson, K. M., Ray, R. D., Nievinski, F. G., & Freymueller, J. T. (2013). The Accidental Tide Gauge: A GPS Reflection Case Study From Kachemak Bay, Alaska, *10*(5), 1200–1204. doi.org/10.1109/LGRS.2012.2236075

Larson, K. M., Ray, R. D., & Williams, S. D. P. (2017). A 10-Year Comparison of Water Levels Measured with a Geodetic GPS Receiver versus a Conventional Tide Gauge. *Journal of Atmospheric and Oceanic Technology*, *34*(2), 295–307. doi.org/10.1175/JTECH-D-16-0101.1

Löfgren, J. S., Haas, R., Scherneck, H.-G., & Bos, M. S. (2011). Three months of local sea level derived from reflected GNSS signals. *Radio Science*, *46*(6). doi.org/10.1029/2011RS004693

Martin-Neira, M., Colmenarejo, P., Ruffini, G., & Serra, C. (2002). Altimetry precision of 1 cm over a pond using the wide-lane carrier phase of GPS reflected signals. *Canadian Journal of Remote Sensing*, *28*(3), 394–403. doi.org/10.5589/m02-039

Nikolaidou, T., Santos, C. M., Williams, D. P. S., & Geremia-Nievinski, F. (2020a). Raytracing atmospheric delays in ground-based GNSS reflectometry. *Journal of Geodesy*, *94*(68). doi.org/10.1007/s00190-020-01390-8

Nikolaidou, T., Santos, M. C., Williams, S. D. P., & Geremia-Nievinski, F. (2020b). A simplification of rigorous atmospheric raytracing based on judicious rectilinear paths for near-surface GNSS reflectometry. *Earth, Planets and Space*, *72*(91). doi.org/10.1186/s40623-020-01206-1

Park, H., Camps, A., Valencia, E., Rodriguez-Alvarez, N., Bosch-Lluis, X., Ramos-Perez, I., & Carreno-Luengo, H. (2012). Retracking considerations in spaceborne GNSS-R altimetry. *GPS Solutions*, *16*(4), 507–518. doi.org/10.1007/s10291-011-0251-7

Purnell, D. J., Gomez, N., Chan, N.-H. H., Strandberg, J., Holland, D. M., & Hobiger, T. (2020). Quantifying the Uncertainty in Ground-Based GNSS-Reflectometry Sea Level Measurements. *IEEE Journal of Selected Topics in Applied Earth Observations and Remote Sensing*. doi.org/10.1109/JSTARS.2020.3010413

Rius, A., Nogués-Correig, O., Ribó, S., Cardellach, E., Oliveras, S., Valencia, E., … Martín-Neira, M. (2012). Altimetry with GNSS-R interferometry: First proof of concept experiment. *GPS Solutions*, *16*(2), 231–241. doi.org/10.1007/s10291-011-0225-9

Roussel, N., Frappart, F., Ramillien, G., Darrozes, J., Desjardins, C., Gegout, P., … Biancale, R. (2014). Simulations of direct and reflected wave trajectories for ground-based GNSS-R experiments. *Geoscientific Model Development*, *7*(5), 2261–2279. doi.org/10.5194/gmd-7-2261-2014

Santamaría-Gómez, A., & Watson, C. (2017). Remote leveling of tide gauges using GNSS reflectometry: case study at Spring Bay, Australia. *GPS Solutions*, *21*(2), 451–459. doi.org/10.1007/s10291-016-0537-x

Semmling, A. M., Schmidt, T., Wickert, J., Schn, S., Fabra, F., Cardellach, E., … Rius, A. (2012). On the retrieval of the specular reflection in GNSS carrier observations for ocean altimetry. *Radio Science*, *47*(6). doi.org/10.1029/2012RS005007

Treuhaft, R. N., Lowe, S. T., Zuffada, C., & Chao, Y. (2001). 2-cm GPS altimetry over Crater Lake. *Geophysical Research Letters*, *28*(23), 4343–4346. doi.org/10.1029/2001GL013815

Williams, S. D. P., & Nievinski, F. G. (2017). Tropospheric delays in ground-based GNSS multipath reflectometry-Experimental evidence from coastal sites. *Journal of Geophysical Research: Solid Earth*, *122*(3), 2310–2327. doi.org/10.1002/2016JB013612

Zavorotny, V. U., Gleason, S., Cardellach, E., & Camps, A. (2014). Tutorial on remote sensing using GNSS bistatic radar of opportunity. *IEEE Geoscience and Remote Sensing Magazine*, *2*(4), 8–45. doi.org/10.1109/MGRS.2014.2374220

6. Conclusions

Global Navigation Satellite System Reflectometry (GNSS-R) uses GNSS radio waves to remotely sense ocean properties, land geophysical parameters, forest biomass and snow properties. The focus here was on ground-based altimetry sea-level retrievals. Accuracy and consistency of GNSS-R retrievals and their time series is a very demanding issue though, pivotal. Reliable GNSS-R products are a key factor for emerging sea level altimetry applications including predicting high waves, dangerous sea states, risk of flooding, ocean eddy and storm surges. To accomplish stability and fidelity of the sea-level retrievals, it is paramount that systematic errors, such as atmospheric refraction, be mitigated. To achieve that, this work conducted a thorough analysis of the atmospheric delay, starting from the refraction index and concluding with closed-form expressions for the atmospheric altimetry correction in GNSS-R sea-level retrievals.

In the first part, we showed how the interferometric atmospheric delay can be defined based on vacuum distance and radio length, or as the difference between reflected and direct atmospheric delays. The along-path and geometric interferometric delay components were subsequently derived and combined in the total delay. We also introduced for the first time two subcomponents of the atmospheric geometric delay, the geometric-shift and the geometric-excess, unique for reflected signals. The atmospheric altimetry correction was formulated as half the rate-of-change of the delay with respect to the sine of satellite elevation angle, allowing an easy to implement correction in the final sea-level products. The theoretical developments were corroborated by a ray-tracing procedure to solve the reflection three-point boundary value problem, involving the broadcasting satellite, reflecting surface, and receiving antenna. The interested researcher may follow our approach to develop a ray-tracing procedure for GNSS-R, starting from a direct-only ray-tracer.

Results demonstrated that the atmospheric altimetry correction (and atmospheric delay) decreases exponentially with satellite elevation angle but increases linearly with reflector height, thus manifesting as a scale error in the sea-level retrievals. A discussion on the interplay of the delay components, as well as their role in partitioning the total delay as a function of the satellite elevation angle, completed the study highlighting that atmospheric altimetry bias may persist even if the atmospheric delay converges to zero.

In the second part, the goal was to approximate rigorous results while using rectilinear ray-tracing. This was accomplished by implementing two ray-tracing approaches: one at the apparent (refracted) direction, and one at the geometric (vacuum) satellite direction. Although these scenarios failed to capture the rigorous interferometric delay, a judicious combination thereof, the rectilinear-mixed approach, showed excellent agreement in terms of delay, both in total and of its components. Following this approach, the atmospheric altimetry correction can be predicted by one direct rigorous ray-tracing, followed by one reflection rectilinear ray-tracings in the apparent satellite direction. This approach is faster and more efficient because it involves only the broadcasting satellite and receiving antenna. It can also be easily adapted by existing atmospheric ray-tracing software to predict the GNSS-R altimetry corrections. On a side contribution, we described the contribution of atmospheric layers both above and below the receiver to the total interferometric delay, contrary to the popular belief that atmospheric effects above the receiver height cancel out when forming the interferometric delay. It was further evidenced that direct mapping functions, like the ones used in GNSS positioning, are not to be used alone in GNSS-R, by reason of lacking the geometric-shift interferometric delay component.

In the final part we developed closed-form expressions for the atmospheric delay and altimetry corrections for the end-user. In particular, the linear refraction is predicted using the in-situ refractivity whereas the angular refraction uses the bending angle. Only a single direct ray-tracing is required to obtain these inputs and evaluate the altimetry correction for a specific satellite elevation angle. The fine agreement between the closed-form expressions and the ray-tracing results suggests them as an effective and suitable atmospheric refraction mitigation technique in GNSS-R. A deeper look into the rectilinear modelling reinforced the premise that even small reflector heights are still subject to the atmospheric refraction originating above the receiving antenna. A contour graph of multiple nominal atmospheric altimetry correction values with varying reflector height and satellite elevation angle, helped to visualize the limitations that atmospheric refraction poses on the accuracy of the sea-level retrievals. An additional graph in terms of the delay components showed how the along-path component contributes progressively more to the total altimetry correction as the satellite approaches the zenith direction. These illustrations are useful for observation planning and error budgeting of the GNSS-R retrievals. Yet, upon application of the atmospheric altimetry correction proposed herein, the limitations are lifted.

Summarizing, this study enables more accurate sea-level altimetric products (and by-products, such as tidal constituents) by mitigating the effect of atmospheric refraction, therefore supporting the operational use of GNSS-R. At the same time, it aids in geocentric sea-level GNSS-R retrievals which have direct impact on society, the environment and the economy. Reliable, consistent and representative GNSS-R altimetry retrievals will represent a significant step forward for a host of users, including climate scientists and policy-makers. In particular, the correction for the atmospheric refraction in altimetry will improve our understanding of the air-sea exchanges, ocean surface height, wind speed and direction, and even sea ice conditions particularly for ungauged seas, inaccessible areas and harsh sea ice cover. Precision of inundation and wetland monitoring shall also increase. Modelling the atmospheric refraction will also allow for the usage of lower satellite elevation angles, enabling thus the coverage of larger areas.

This study also offers the necessary foundation to further explore atmospheric refraction in GNSS-R. This work aspires to ignite atmospheric science research in benefit of other GNSS-R applications, e.g., snow sensing, and beyond near-surface configurations, e.g., airborne GNSS-R. While procedures for correcting the atmospheric refraction for GNSS positioning are well established and recommendations for long time series processing have been recently published (Bock et al., 2020), there is nothing comparable for GNSS-R observations or time series. Based on the findings of this work, GNSS-R historic observations can be corrected for atmospheric refraction, allowing for a more precise validation against tide gauge (and altimetry) long time series records.

6.1. Systematic Errors in Atmospheric Modelling

Factors we did not consider in this study or we assume they were constant and error-free can contribute to a systematic bias under different conditions. These include the spatio-temporal variation of the refractivity and elevation bending, the relative humidity of the atmosphere and errors in the position of the receiver/satellite.

According to CIRA-84, refractivity at sea level height, varies globally between 0.000255– 0.000305. This range variation will bias the atmospheric (along-path) relative altimetry correction (eq.(25)), by 6 mm/m, at a 5 degrees satellite elevation angle. The temporal variability N is within the above limits, so a similar impact is expected on the altimetry correction. Still, N has also a strong vertical dependency (decreasing exponentially with altitude) and it would be more appropriate to consider its global variation at the orography. It ranges between 0.00015 – 0.0003, resulting to an altimetry correction bias of 1.8 cm/m.

On the other hand, the elevation bending at 5 degrees satellite elevation angle, varies between 0.09 degrees – 0.17 degrees globally, again based on CIRA-84. Such variation will bias the along-path altimetry correction by a sub-cm bias (1.2 mm) and it can be considered negligible for the geometric altimetry correction. As a result, we may conclude that the spatial variability of the altimetry correction is caused at large by the global refractivity variation, yet it remains at few cm-level. The temporal variation of N and δe is within the limits of their spatial variation and thus similar findings can be expected.

Relative humidity is known to contribute about 10% of the direct atmospheric delay at zenith. Generalizing this rule-of-thumb for the interferometric zenith atmospheric delay though is valid only for the along-path delay component, according to the findings of Chapter 5. Nonetheless, at zenith, where no bending exists, the rule predicts that humidity will have an impact of 0.6 mm/m in the total interferometric delay for 10-m reflector height, which will scale to 3 mm/m if a reflector height of 50-m is used instead. In terms of atmospheric altimetry correction, the impact remains at the same level due to the slow rate of change of the delay with respect to the sine of the elevation angle. Although the zenith interferometric geometric delay is not zero, as shown in Chapter 1, the impact of humidity bending is considered negligible due to the minimal rate of change of the bending with respect to the elevation angle as such elevations.

6.2. Random Errors in Atmospheric Modelling

It is recognized that random commission errors occur which can affect the atmospheric altimetry correction and limit its effectiveness. Although modelling the uncertainty is beyond the scope of this work, this section attempts to identify them and estimate their impact.

The random error budget consists of the uncertainty in refractivity and elevation bending, the two independent variables of the closed form expressions, assuming a constant reflector height, during an "interferometric" observation. Though these variables are interdependent producing an extra error term from their correlation, in this first approach to determine the errors we assume it is negligible compared to the individual variable's errors.

The uncertainty in refractivity and in elevation bending originates from the uncertainty in the meteorological variables of pressure P, temperature T, and humidity (e.g., water vapor pressure[12] ρ), used to determine it. They relate to the quality and accuracy of the atmospheric source used for the ray-tracing. According to the propagation law of errors, the uncertainty in N is: due to the error in P, $\sigma_{N_{|P}} = \frac{77.6}{T}\sigma_P$, due to the error in T, $\sigma_{N_{|T}} = \left(-\frac{77.6}{5T^2} - \frac{72\rho}{T^2} - \frac{750000\rho}{T^3}\right)\sigma_T$ and due to the error in ρ, $\sigma_{N_{|\rho}} =$

---

[12] Although we did not consider humidity in this work, based on our references, we consider its uncertainty in this paragraph to provide a more realistic result for the total refractivity.

$\left(\frac{72}{T} - \frac{375000}{T^2}\right)\sigma_{\rho}$. CIRA-86 meteorological data is not accompanied by its uncertainties. However, if a 20% error in the meteorological variables is assumed (Ya, Krasitsky, Marov M.Ya, & Krasitsky O. P., 1990), on standard meteorological conditions, at the equator, and at sea level height (P = 1013.25 hPa, T = 28° C, and ρ = 23 hPa), the uncertainty in N due to the error in P, T, and ρ quantifies at 14%, 25% and 6% respectively. Whereas if all three variables are considered together (still uncorrelated) the combined error reaches nearly 30% of the N. In terms of atmospheric altimetry correction and assuming for now that the apparent satellite elevation angle is perfectly determined (i.e., neglecting elevation bending uncertainty), it will affect the relative altimetry correction (mean value 4.4 cm/m) by ±1.3 cm/m, or 29.5%, at 5 degrees satellite elevation angle. At an elevation angle of 10 degrees the same error, will affect the relative correction (1.2 cm/m) by nearly ±0.4 cm/m, or 33.3%. It is evident that the relative uncertainty in ΔH due to N increases with decreasing elevation angle: $\sigma_{\Delta\tilde{H}_i^a/H} = \sigma_{\tilde{N}_\ell^z} \cdot \sin^{-2} e'$.

Now turning to the elevation bending, it is determined by the ray-tracing procedure based on the gradient of refractivity. Based on the closed-form expressions (eq.(25)), the uncertainty in the relative geometric atmospheric altimetry correction $\sigma_{\Delta\tilde{H}_i^g/H}$, is more complicated as it involves the dependency of its rate-of-change with respect to the elevation angle, on it: $\sigma_{\Delta\tilde{H}_i^g/H} = \sigma_{\frac{\partial\delta e}{\partial e}}$, which in turn it involves the correlation between successive elevation angles. Assuming two close enough, successive elevation angles, e_1 and e_2, the elevation bending rate can be approximated as: $\frac{\partial\delta e}{\partial e} \approx \frac{\delta e_2 - \delta e_1}{e_2 - e_1} = \frac{\Delta\delta e}{\Delta e}$. Then its uncertainty yields as: $\sigma_{\frac{\partial\delta e}{\partial e}} = \sigma_{\frac{\Delta\delta e}{\Delta e}} = \left(2\sigma_{\delta e}^2 - 2\rho\sigma_{\delta e}^2\right)^{0.5}/\Delta e$, which denotes its additional dependency on the correlation of e_2 and e_1. Upon an educated guess (Bennett, 1982) a maximum error in bending at the range of 0.07”- 0.2” is assumed for a standard and a non-standard atmospheric conditions, respectively. Selecting the largest error (0.2”), and approximating the uncertainty numerically, yields a 5% error in the relative geometric atmospheric altimetry correction or equivalently 2.4 mm/m for elevation angles between 0-5 degrees. The same elevation bending error has a negligible effect (< 1%) in the along-path altimetry correction.

Last but not least, an error in the atmospheric delay due to an error in the satellite orbits is considered negligible based on the findings of M. Semmling, (2012). However, a bias in the receiver position will have a direct effect on the atmospheric altimetry correction. In particular, the altimetry correction will be biased by twice the vertical component of the receiver position error, based on eq. (25). The impact of a small error (e.g., mm to cm level) on refractivity and elevation bending can be considered negligible.

6.3. Modelling Limitations

In this study we made certain assumptions concerning the atmospheric source, atmospheric setup, and reflecting surface; These assumptions serve well the scope of this work: ground-based, near-surface GNSS-R altimetry for a smooth and planar surface, but will inevitably introduce systematic errors under more extreme conditions such as airborne or spaceborne platforms and/or very low or even negative satellite elevation angles. In this section, we discuss each one of the assumptions and offer suggestions to raise the limitations they bring.

6.3.1. Atmospheric source

In terms of atmospheric source, the COSPAR International Reference Atmosphere 1986 (CIRA-86) climatology (Chandra et al., 1990; Fleming et al., 1990) does not include humidity and its contribution has been consciously ignored in the present analysis. Dry gases are known to be responsible for the majority of the atmospheric delay in radio propagation and to remain relatively stable over time and space. In contrast, humidity has a smaller contribution (<10% at zenith) and is highly variable. Therefore, we expect the present study to represent well the bulk of the atmospheric effect in ground-based GNSS-R. Wet contributions should be small on average, being more important for representing higher frequency variability. However, we recognize the importance of its contribution and it is recommended to be the subject of future research. The inclusion of higher order atmospheric sources, i.e., a numerical weather model (NWM), is also recommended, especially if the surface layers are to be exploited for more accurate prediction of the refractivity. Although there are several studies (Alshawaf et al., 2018; Balidakis et al., 2018; Teke et al., 2013) on the consistency of surface NWM variables for GNSS atmospheric applications, their utility in GNSS-R remains unexplored. Using reanalysis NWM, e.g., ERA5 reanalysis model produced by the European Centre for Medium-Range Weather Forecasts (Hersbach et al., 2020), would be highly valuable in that regard. Furthermore, a high spatio-temporal resolution NWM, like ERA5 (Hersbach et al., 2020), would be beneficial to decorrelate atmospheric disturbances and a moving reflector as in the presence of high tides.

6.3.2. Atmospheric setup

In this work we used a 1-D spherical osculating atmosphere (Nievinski & Santos, 2010), and assumed a planar, horizontal and smooth surface below the antenna. Although these assumptions served well the purpose of the current study, they should be re-evaluated for higher accuracy. A more realistic 3-D atmospheric setup (Nievinski & Santos, 2010) could potentially improve the atmospheric altimetry prediction for individual satellite tracks, especially for cases of azimuthal variation of the refractive index.

6.3.3. Earth's model

Earth's curvature is an important factor to consider, particularly when the employed reflector height is very high and the satellite elevation angle is very low (more than few hundreds of meters and/or near the horizon, respectively). The higher the altitude of the antenna, the further away the reflections can occur. For instance, site NOMI, on island Santorini, in Greece, has a theoretical view-point of 3.4 km at 5 degrees satellite elevation angle (assuming a flat Earth model). At such heights, a flat Earth model can introduce dm level bias in the altimetry retrievals, that can grow up to 1-meter, at 5 degrees elevation angle. In general, the bias is particularly evident at low satellite elevation angles (<10 degrees) and converges to zero at the vicinity of the station. Semmling et al. (2011) used an ellipsoidal Earth model for the calculation of the reflection point in a ray-tracing procedure. However, no closed-form expressions were derived, so the analytical effect of the Earth's curvature on the atmospheric altimetry correction has not been fully examined yet. Though, it is expected to depend on the excess interferometric path length, caused by surface curvature, as well as the possible displacement of the reflection point, should its magnitude be significant.

Geoid undulation is another parameter to consider in the model for a more accurate determination of the reflection point. Although its effect on the atmospheric altimetry correction is yet to be determined M. Semmling, (2012) showed that it can bias the retrieved surface heights by as much as 20 cm at the steep coast of Disko Island in Western Greenland.

With these limitations in mind, for reflector heights exceeding few hundreds of meters, and very low/negative satellite elevation angles, the atmospheric altimetry corrections developed in this work cannot guarantee a full compensation of the atmospheric refraction effect.

6.4. Future work

Despite our best efforts, as our understanding of interferometric atmospheric refraction deepened, we came upon new uncharted territories waiting to be explored. In addition to the aforementioned possibilities to expand the current work, here we identify two immediate future objectives.

One objective is the tabulation of auxiliary variables to the closed-form expressions: refractivity and elevation bending. A blind model, function of location (latitude, longitude, altitude and azimuth) as well as day-of-year, based on ray-tracing outputs and/or a provisional model using in-situ meteorological data as proxies (e.g., pressure), are the two viable alternatives we envision. While the first alternative offers a quick and handy solution to correct the altimetry retrievals for atmospheric refraction, the second can provide more accurate results by calibrating the model to the local meteorological conditions. Such models would further accommodate end-users without access to a ray-tracing package and facilitate the adoption of atmospheric altimetry correction for GNSS-R studies, thus promoting more accurate and time-stable altimetry retrievals.

Then, an experimental demonstration of the atmospheric altimetry correction using field GNSS-R observations is the second objective. It would require accounting for some of the pending issues raised above, as atmospheric refraction alone is not expected to fully account for the field observations. This future work will indicate the level of improvement attained by correcting for atmospheric refraction under field conditions. It will be an important contribution to the literature for enabling absolute, instead of relative, validation against the tide gauges via the geocentric height of the sea surface.

For dynamic scenarios, such as spaceborne and airborne GNSS-R altimetry, the need for a combined ray-tracing to solve simultaneously for atmospheric altimetry correction and reflector height is a subject that requires investigation. Although research has been initiated by Hu, Benson, Rizos, & Qiao (2019), who showed in a simulation study of spaceborne GNSS-R that receiver dynamics can lead to altimetric errors of the order of several meters if not included in the geometric model, further study is necessary.

Another effect that requires investigation for its impact on the atmospheric altimetry correction is the phase wind-up, caused by the relative orientation between the receiving and transmitting antenna. A starting point for such research can be found at (Beyerle, 2009; M. Semmling, 2012; Wu, Wu, Hajj, Bertiger, & Lichten, 1992)where the effect in GNSS-R observations is examined.

Modelling the atmospheric delay is a step forward to fully exploit the enormous potential of GNSS-R altimetry; that is, if the plethora of open, global and multi-GNSS can be used for accurate and stable sea-level monitoring. Risk management solutions can be delivered informed by leading-edge science so that businesses and governments can make strategic decisions to manage the world’s ocean resources. To this end, the present work encompasses a research contribution on atmospheric refraction for GNSS reflections.

References

Alshawaf, F., Zus, F., Balidakis, K., Deng, Z., Hoseini, M., Dick, G., & Wickert, J. (2018). On the Statistical Significance of Climatic Trends Estimated From GPS Tropospheric Time Series. *Journal of Geophysical Research: Atmospheres*, *123*(19), 10,967-10,990. doi.org/10.1029/2018JD028703

Balidakis, K., Nilsson, T., Zus, F., Glaser, S., Heinkelmann, R., Deng, Z., & Schuh, H. (2018). Estimating Integrated Water Vapor Trends From VLBI, GPS, and Numerical Weather Models: Sensitivity to Tropospheric Parameterization. *Journal of Geophysical Research: Atmospheres*, *123*(12), 6356–6372. doi.org/10.1029/2017JD028049

Bennett, G. G. (1982). The Calculation of Astronomical Refraction in Marine Navigation. *Journal of Navigation*, *35*(02), 255. doi.org/10.1017/S0373463300022037

Beyerle, G. (2009). Carrier phase wind-up in GPS reflectometry. *GPS Solutions*, *13*(3), 191–198. doi.org/10.1007/s10291-008-0112-1

Bilich, A., & Larson, K. M. (2007). Mapping the GPS multipath environment using the signal-to-noise ratio (SNR). *Radio Science*, *42*(6), 1–16. doi.org/10.1029/2007RS003652

Bock, O., Pacione, R., Ahmed, F., Araszkiewicz, A., Bałdysz, Z., Balidakis, K., … Xaver, A. (2020). Use of GNSS Tropospheric Products for Climate Monitoring (Working Group 3). In *Advanced GNSS Tropospheric Products for Monitoring Severe Weather Events and Climate* (pp. 267–402). Cham: Springer International Publishing. doi.org/10.1007/978-3-030-13901-8_5

Chandra, S., Fleming, E. L., Schoeberl, M. R., & Barnett, J. J. (1990). Monthly mean global climatology of temperature, wind, geopotential height and pressure for 0-120 km. *Advances in Space Research*, *10*(6), 3–12. doi.org/10.1016/0273-1177(90)90230-W

Fleming, E. L., Chandra, S., Barnett, J. J., & Corney, M. (1990). Zonal mean temperature, pressure, zonal wind and geopotential height as functions of latitude. *Advances in Space Research*, *10*(12), 11–59. doi.org/10.1016/0273-1177(90)90386-E

Hersbach, H., Bell, B., Berrisford, P., Hirahara, S., Horányi, A., Muñoz-Sabater, J., … Thépaut, J. (2020). The ERA5 global reanalysis. *Quarterly Journal of the Royal Meteorological Society*, qj.3803. doi.org/10.1002/qj.3803

Hu, C., Benson, C. R., Rizos, C., & Qiao, L. (2019). Impact of Receiver Dynamics on Space-Based GNSS-R Altimetry. *IEEE Journal of Selected Topics in Applied Earth Observations and Remote Sensing*, *12*(6), 1974–1980. doi.org/10.1109/JSTARS.2019.2910544

Jacobson, M. D. (2014). Estimating snow water equivalent for a slightly tilted snow-covered prairie grass field by GPS interferometric reflectometry. *Eurasip Journal on Advances in Signal Processing*, *61*. doi.org/10.1186/1687-6180-2014-61

Nievinski, F. G. (2013). *Forward and Inverse Modeling of GPS Multipath for Snow Monitoring (Ph.D. thesis).* University of Colorado. Retrieved from https://cires1.colorado.edu/portal/publications/Nievinski_2013_PhD.pdf

Nievinski, F. G., & Larson, K. M. (2014a). Forward modeling of GPS multipath for near-surface reflectometry and positioning applications. *GPS Solutions*, *18*(2), 309–322. doi.org/10.1007/s10291-013-0331-y

Nievinski, F. G., & Larson, K. M. (2014b). Inverse Modeling of GPS Multipath for Snow Depth Estimation—Part I: Formulation and Simulations. *IEEE Transactions on Geoscience and Remote Sensing*, *52*(10), 6555–6563. doi.org/10.1109/TGRS.2013.2297681

Nievinski, F. G., & Santos, M. C. (2010). Ray-tracing options to mitigate the neutral atmosphere delay in GPS. *Geomatica*, *64*(2), 191–207.

Semmling, A. M., Beyerle, G., Stosius, R., Dick, G., Wickert, J., Fabra, F., … D'Addio, S. (2011). Detection of Arctic Ocean tides using interferometric GNSS-R signals. *Geophysical Research*

Letters, *38*(4). doi.org/10.1029/2010GL046005

Semmling, M. (2012). *Altimetric Monitoring of Disko Bay using Interferometric GNSS Observations on L1 and L2 (Ph.D. thesis)*. Scientific Technical Report STR12/04. Deutsches GeoForschungsZentrum GFZ. doi.org/10.2312/GFZ.b103-12049

Strandberg, J., Hobiger, T., & Haas, R. R. (2017). Coastal Sea Ice Detection Using Ground-Based GNSS-R. *IEEE Geoscience and Remote Sensing Letters*, *14*(9), 1552–1556. doi.org/10.1109/LGRS.2017.2722041

Teke, K., Nilsson, T., Böhm, J., Hobiger, T., Steigenberger, P., García-Espada, S., … Willis, P. (2013). Troposphere delays from space geodetic techniques, water vapor radiometers, and numerical weather models over a series of continuous VLBI campaigns. *Journal of Geodesy*, *87*(10–12), 981–1001. doi.org/10.1007/s00190-013-0662-z

Wu, J. T., Wu, S. C., Hajj, G. A., Bertiger, W. I., & Lichten, S. M. (1992). Effects of antenna orientation on GPS carrier phase. *IN: Astrodynamics 1991; Proceedings of the AAS/AIAA Astrodynamics Conference, Durango, CO, Aug. 19-22, 1991. Pt. 2 (A92-43251 18-13). San Diego, CA, Univelt, Inc., 1992, p. 1647-1660.*, 1647. Retrieved from https://ui.adsabs.harvard.edu/abs/1992asdy.conf.1647W/abstract

Ya, M., Krasitsky, P., Marov M.Ya, & Krasitsky O. P. (1990). Some comments on the CIRA-86 model. *Advances in Space Research*, *10*(6), 117–121. Retrieved from https://reader.elsevier.com/reader/sd/pii/027311779090242R?token=D563F0AEB5714C7DDAB787BAE8B7812777C2721519CC8782A7640FC19D28FBA3726D6AEF941CC9C72A86EC0D0441A60C

Curriculum Vitae

Candidate's full name: Thalia Nikolaidou

Universities attended:

Diploma in Rural and Surveying Engineering (2014), Aristotle University of Thessaloniki, Greece

Publications:

Nikolaidou, T., Santos, C. M., Williams, D. P. S., & Geremia-Nievinski, F. (2020a). Raytracing atmospheric delays in ground-based GNSS reflectometry. Journal of Geodesy. https://doi.org/10.1007/s00190-020-01390-8

Nikolaidou, T., Santos, M. C., Williams, S. D. P., & Geremia-Nievinski, F. (2020b). A simplification of rigorous atmospheric raytracing based on judicious rectilinear paths for near-surface GNSS reflectometry. *Earth, Planets and Space*, 14. https://doi.org/10.1186/s40623-020-01206-1

Nikolaidou, T., Santos, M. C., Williams, S. D. P., & Geremia-Nievinski, F. (2020c). Closed-form expressions for atmospheric delay and altimetry correction in ground-based GNSS reflectometry. *IEEE Transactions on Geoscience and Remote Sensing*, [submitted]

Mayaki, A. O., Santos, M., & **Nikolaidou, T.** (2020). Least-Squares Spectral and Coherency Analysis of the Zenith Total Delay Time Series at SuomiNet Station SA56 (UNB2) (pp. 1–10). Springer, Berlin, Heidelberg. https://doi.org/10.1007/1345_2020_110

Mayaki, A. O., **Nikolaidou, T.,** Santos, M., & Okolie, C. J. (2018). Comparing the Nigerian GNSS Reference Network's Zenith Total Delays from Precise Point Positioning to a Numerical Weather Model. *International Association of Geodesy Symposia International Symposium on Advancing Geodesy in a Changing World* (pp. 149: 143-150). Springer, Cham. https://doi.org/10.1007/1345_2018_43

Nikolaidou, T., Balidakis, K., Nievinski, F., Santos, M., & Schuh, H. (2018). Impact of different NWM-derived mapping functions on VLBI and GPS analysis Introduction and background. *Earth, Planets and Space*, *70*, 95. https://doi.org/10.1186/s40623-018-0865-x

Santos, M. C., & **Nikolaidou, T.** (2018). Modeling neutral-atmospheric electromagnetic delays in a "big data" world. *Geo-spatial Information Science*, *21*(2), 75–79. Taylor & Francis. https://doi.org/10.1080/10095020.2018.1461780

Nikolaidou, T., Nievinski, F., Balidakis, K., Schuh, H., & Santos, M. (2018). PPP Without Troposphere Estimation: Impact Assessment of Regional Versus Global Numerical Weather Models and Delay Parametrization. International Association of Geodesy Symposia International Symposium on Advancing Geodesy in a Changing World (pp. 1–12). Springer, Berlin, Heidelberg. https://doi.org/10.1007/1345_2018_44

Selected Conference Presentations

Nikolaidou, T., Landskron, D., Mendonça, M., Boehm, J., & Santos, M. C. (2019). VMF3 versus VMF1: A Delay-domain Comparison Over the IGS Network. *The International Union of Geodesy and Geophysics*.

Nikolaidou, T., Santos, M. C., Williams, S. D. P., & Nievinski-Geremia F. (2019). An overview of tropospheric delays in ground-based GNSS reflectometry. *International Union of Geodesy and Geophysics*.

Santos, M. C., Pacione, R., Balidakis, K., Mendonça, M., Wickert, J., Dick, G., Heinkelmann, R., Mannel, B., & **Nikolaidou, T.** (2019). Combination of zenith delay estimates and its potential implications for climate. *International Union of Geodesy and Geophysics*.

Nikolaidou, T., Williams, S. D. P., Santos, M. C., & Nievinski, F. G. (2019). Tropospheric delays in ground-based GNSS reflectometry: Rigorous ray-tracing, rectilinear propagation, and nominal models. *IEEE GNSS+R*.

Nikolaidou, T., & Santos, M. C. (2018). Assessing state-of-the-art tropospheric gradients model under severe weather phenomena in geodetic analysis. *IX Hotine-Marussi Symposium*.

Nikolaidou, T., Nievinski, F. G., Balidakis, K., & Santos, M. C. (2017). Impact assessment of regional versus global Numerical Weather Model–derived tropospheric corrections for GPS. *Joint Scientific Assembly of International Association of Geodesy*.

Nikolaidou, T., & Santos, M. C. (2017). Effect of regional Numerical Weather Models on GNSS Positioning. A case study under non- standard atmospheric conditions. *Canadian Geophysical Union*.

Nikolaidou, T. (2016). GAPS: GPS Analysis & Positioning Software On-line & free. *2nd international Federation of Surveyors (FIG) Young Surveyors North American Meeting*.

Nikolaidou, T., & Santos, M. C. (2016). Impact of direct ray-tracing in PPP GNSS analysis. *Canadian Geophysical Union Joint Annual Meeting*.

Santos, M. C., & **Nikolaidou, T.** (2015). Trends in modelling neutral-atmospheric electromagnetic delays in a ‘big data’ world. *American Geophysical Union*.

Nikolaidou, T., Nievinski, F., & Santos, M. (2017). Atmospheric oscillations comparison on long term tropospheric delay time series derived from ray-tracing in Numerical Weather Model and GPS Precise Point Positioning *19th EGU General Assembly, EGU2017*.

Nikolaidou, T., Balidakis, K., Nievinski, F., Mendonça, M., Santos, M., & Schuh, H. (2016). Impact of different NWM-derived mapping functions on VLBI and GNSS analysis. *European Geophysical Union (EGU) General Assembly 2016*.